Control of Micro-Hybrid Boosting

by

Shima Nazari

A dissertation submitted in partial fulfillment
of the requirements for the degree of
Doctor of Philosophy
(Mechanical Engineering)
in The University of Michigan
2019

Doctoral Committee:

Professor Anna Stefanopoulou, Chair
Professor Ilya Kolmanovsky
Associate Research Scientist Jason Siegel
Assistant Professor Ramanarayan Vasudevan

Shima Nazari

snazari@umich.edu

ORCID iD: 0000-0002-1775-4664

To my mother, for her endless love and support.

ACKNOWLEDGEMENTS

This dissertation and its underlying research was not possible without the collaboration and support of countless people. First and foremost, I want to thank my research advisor and doctoral committee chair Professor Anna Stefanopoulou. I will always be grateful for her trust when she hired me. Her work ethic and her dedication to research and her students was admirable and her generous support during the past five years always pushed me forward. Second, I want to thank Dr. Jason Siegel, a pivotal member of the Powertrain Control Laboratory (PCL). This work was not possible without his nonstop work in the engine test cell and without his endless patience with my questions. I also want to thank Dr. Ilya Kolmanovsky and Dr. Ramanarayan Vasudevan for joining my dissertation committee and for their valuable remarks and fruitful discussions.

The financial support for this research was provided by the Advanced Research Projects Agency-Energy (ARPA-E) U.S. Department of Energy, under Award Number DE-AR0000659. I want to thank ARPA-E and U.S. taxpayers for providing the funds that supported this work and Dr. Chris Atkinson and Dr. Gokul Vishwanathan from ARPA-E for useful feedbacks and rewarding discussions. I also would like to thank EATON corporation and Southwest Research Institute for providing the hardware and technical support instrumental to the success of this work.

I want to thank Dr. Robert Middleton for his collaboration and support on numerous matters during my PhD years and Charles Solbrig for his assistance on engine dynamometer experiments. I am grateful to all other PCL members that I had a chance to work with during these years including Dr. Jason Martz, Rani Kiwan, Niket Prakash, Kanji Sugimori and Ashley Wiese. I want to thank all my friends in PCL and Ann Arbor, with whom I shared many unforgettable moments and who made my PhD journey pleasant.

Last but not least, I want to thank my family, my husband, Reza, who started this adventure with me and stood by my side the entire time. My mother, Saba, who taught me the value of learning and hard work and for her endless love, my father, Shahpoor, for believing in me and my sister and brother for their never-ending support.

TABLE OF CONTENTS

LIST OF FIGURES

Figure

LIST OF TABLES

Table

LIST OF ABBREVIATIONS

BAR Boost assist rule

BMEP Brake mean effective pressure

BSFC Brake specific fuel consumption

BSR Blade speed ratio

CAFE Corporate average fuel economy

cEGR Cooled exhaust gas recirculation

CMR Consumption minimization rule

DP Dynamic programming

ECMS Equivalent consumption minimization

EGR Exhaust gas recirculation

EMS Energy management system

eSC Electric supercharger

eTC Electric turbocharger

EV Electric vehicle

FC Fuel consumption

FCV Fuel cell vehicle

FE Fuel economy

FMEP Friction mean effective pressure

GHG Greenhouse gas

HEV Hybrid electric vehicle

hSC Hybrid supercharger

ICE Internal combustion engine

IDM Intelligent driver model

IEG Induction to exhaust gas

IMEP Indicated mean effective pressure

IPS Induction to power stroke

LDV Light duty vehicle

LP-EGR Low pressure exhaust gas recirculation

LTI Linear time invariant

MBT Maximum brake torque

MIMO Multi-input multi-output

MPC Model predictive control

mpg Miles per gallon

mph Miles per hour

MVM Mean value model

NA Naturally aspirated

PDE Partial differential equation

PMEP Pumping mean effective pressure

PSS Power split supercharger

SGM Starter generator motor

SI Spark Ignition

SIDI Spark Ignition Direct Injection

SoC State of Charge

TAR Torque assist rule

TC Turbocharger

ABSTRACT

Powertrain hybridization has been shown to greatly improve vehicle fuel economy, with significant additional component costs. A novel type of low voltage hybrid device, called a power split supercharger (PSS), has the potential to provide hybrid functionality at reduced system cost. The PSS is configured with a supercharger, a planetary gear set and a motor. The electric motor in the PSS system can be used in two discrete modes. It can drive the supercharger at variable speed and provide flexible boost pressure to the engine, or it can be employed to directly supply/receive torque to/from the crankshaft like a typical parallel hybrid powertrain. This work presents modeling, control design, optimization, and analysis of the PSS in fuel economy improvement of a light duty vehicle. The low-level controller for the air charge management of a twincharged engine with a PSS has to coordinated three actuators, throttle, wastegate, and the PSS in the nonlinear air path of the engine in a fraction of second to ensure fast engine torque control. A decentralized controller that uses the throttle to control intake manifold pressure and employs both the PSS and wastegate to control the boost pressure, in a master-slave configuration, is adopted. The controller was validated on a high fidelity GT-Power engine model and shown to effectively reduce the response time of the engine during critical transients to less than 0.5 second.

During large torque requests, the supervisory energy management system in a vehicle equipped with a PSS must decide whether to use the electric motor to drive the supercharger or supply the motor torque directly to the crankshaft. An optimal control problem for energy management of the PSS was formulated and solved over the standard EPA drive cycles using dynamic programming (DP). The DP solution provides the best selection of operating mode as well as the potential fuel economy benefit of the system. The results show that the optimal controller often selects the parallel hybrid mode over the supercharging mode to minimize the fuel consumption of the vehicle. Moreover, the PSS provides 75% of full hybridization benefit and is as efficient as a two motor solution. An online energy management system that minimizes the equivalent fuel consumption of the engine and motor at each time instant was also developed and shown to have good agreement with the DP results. The simulation time trajectories were supplied to an engine dynamometer experimental setup, which demonstrated that the PSS and EGR combined improve the vehicle fuel economy by 35.5% over the FTP75 cycle compared to a baseline turbocharged engine.

The fuel economy benefit of the PSS in combination with automation was also studied in this thesis. Automated vehicles can use a preview of the ahead traffic and plan their trajectory to minimize fuel consumption and maximize the benefit of a small hybrid system like the PSS. The fuel consumption minimization problem in a car following scenario for a vehicle equipped with a PSS was formulated and solved by sequential optimization of the velocity profile and energy management system. It was shown that with velocity smoothing a small hybrid system like the PSS can provide the fuel economy of a full hybrid powertrain at a lower cost.

CHAPTER I

Introduction

1.1 Background

The transportation sector is responsible for 28% of the U.S. Greenhouse Gas (GHG) emissions [3], 83% of which are emitted from vehicles with the Light Duty Vehicle (LDV) segment being the largest contributor [4]. Improving the fuel economy of LDVs is a compelling solution to stabilizing the GHG emissions and decreasing the reliance on fossil fuels. This target is pursued globally as seen in Figure 1.1, which represents the historical data and projection of future fuel economy targets for different countries normalized to U.S. Corporate Average Fuel Economy (CAFE) test cycles. These increasing fuel economy targets presents numerous challenges to the automotive industry.

Fuel Cell Vehicles (FCVs) and Electric Vehicles (EVs) are two examples of efforts in switching to alternative energy sources for reducing GHG emissions. Although both technologies are very promising in terms of emission reduction, their price and performance are not competitive to conventional Internal Combustion Engines (ICEs). FCVs and EVs cannot cover the full spectrum of customers' demand because they both use batteries to store electric energy and use it later for propulsion. During recent years many improvements in battery technology have been achieved but battery systems are still expensive, their performance degrades with time, their charging time is not comparable to fueling time, and their energy density is small compared to fuel. Due to all these reasons the market penetration of these vehicles is poor.

In the mean time, while battery technology is still evolving, improving ICEs efficiency can be pursued as a short term or mid term solution to fuel efficient transportation. Boosting and downsizing, alternative combustion modes, cylinder deactivation and exhaust gas recirculation are examples of efforts towards decreasing ICEs fuel consumption. These advanced efficient ICEs often suffer from transient response issues, due in part to their complexity. Engine electrification and low voltage hybridization can overcome such transient response challenges and further improve the vehicle fuel economy. In this work both engine air path electrification and powertrain hybridization are considered for enhancing the engine performance and fuel economy.

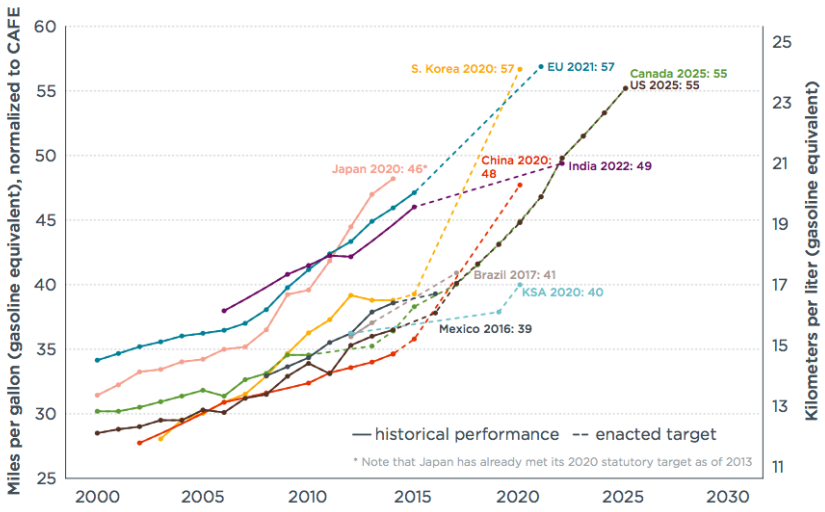

Figure 1.1: Comparison of projected and actual fuel economy targets for new vehicles throughout the world normalized to U.S. CAFE test cycles [1]

1.2 Air Path Electrification

Employing a smaller displacement engine improves the drive cycle fuel efficiency of a vehicle because engines tend to have a higher efficiency at higher relative pressures. The smaller engine has a lower maximum torque though, resulting in a poor acceleration. Boosting the engine air charge permits putting more air into the engine, burning more fuel and producing a larger torque and satisfactory acceleration.

Turbocharging is the most popular method for boosting the engine inlet charge. The turbocharger turbine recovers part of the wasted energy in the exhaust gases to spin the compressor, which is an efficient practice despite imposing some backpressure. Turbocharged engines suffer from two main drawbacks compared to electric boosting systems. One is the engine transient response and the other is the imposed backpressure for non-boosted conditions. The torque response of turbocharged engines is tied to the turbocharger acceleration and hence the exhaust gas enthalpy and turbocharger inertia, causing a delayed torque response known as turbolag. Gasoline turbocharged engines keep the turbocharger spinning at a higher speed than needed by closing the wastegate at non-boosted points to reserve some boost pressure across the throttle valve. The rapid intake filling associated with throttle opening enables fast torque response during tip-ins and mitigates the turbolag [5, 6]. However, this approach imposes unwanted backpressure and pumping loss on the engine and increases fuel consumption at points where no boost is required. Turbocharger electrification by inserting an electric machine on the turbocharger shaft has been pursued to decrease the engine turbolag [7–9]. In such a system the electric motor can assist the turbocharger acceleration during torque tip-ins and recover some energy during steady state. This approach

has its own limitations and is not considered in this study.

Supercharging is an alternative boosting mechanism. The supercharger is usually driven by either the engine crankshaft or an electric motor, which have higher fuel penalties compared to the backpressure imposed by a turbocharger. Mechanical superchargers, in which the supercharger is connected to the engine crankshaft through a fixed gear ratio, is the most common supercharging method. Although the engine air path dynamics are faster with a mechanical supercharger compared to a turbocharger but still transients can suffer from delays due to the speed coupling with the engine crankshaft. This coupling also prevents active control of the boost pressure produced by the supercharger leading to unwanted throttling loss at some operating points. Some studies suggest that variable speed supercharging is more efficient compared to either conventional mechanical supercharging or turbocharging due to lower throttling loss and higher supercharging efficiency enabled by right-sizing the compressor. As an example, McBroom et al. [10] showed that an engine with a variable speed supercharger, achieved with a continuously variable planetary transmission, can produce a higher fuel economy compared to a turbocharged engine counterpart in addition to exhibiting faster boost pressure response. Other studies have also addressed the fast engine torque management with electric superchargers [11, 12].

In this work variable speed supercharging through hybrid boosting and electric boosting is pursued. Figures 1.2(b) and 1.2(c) show such boosting systems with a hybrid supercharger (hSC) and an electric supercharger (eSC) respectively. Although a supercharged engine burns more fuel under boosted conditions, during a typical driving profile such as the HWFET or FTP75, a supercharged engine can actually have a better fuel economy due to the decreased pumping losses at non-boosted points [13, 14].

Superchargers can also be used as transient response facilitators in combination with a turbocharger [15–18], called twincharging. Figure 1.3(a) shows a twincharged engine in a super-turbo configuration realized with an electric supercharger and Figure 1.3(b) represents a turbo-super arrangement with a hybrid supercharger. Twincharged engines have higher low-end torque and faster transient response compared to turbocharged engines. In this work improving the turbocharged engine transient response by adding a supercharger is also considered. The air path of such engine is a Multi-Input/Multi-Output (MIMO) nonlinear system with the throttle, wastegate and the supercharger as pressure actuators. Furthermore, the engine fuel consumption depends on the control strategy and actuator set points, because the boost providers, supercharger and turbocharger, have different fuel penalties. In this work a decentralized controller is proposed for such a system that uses the turbocharger during steady state and employs the supercharger as a transient response enabler.

The fast engine torque response enabled by electrified boosting permits implementing advanced engine calibrations that trade-off transient response for fuel economy. For example one shared problem of all gasoline boosted engines is the combustion auto ignition tendency, or knocking, at highly boosted operating points. Knock damages the engine and sub-optimal

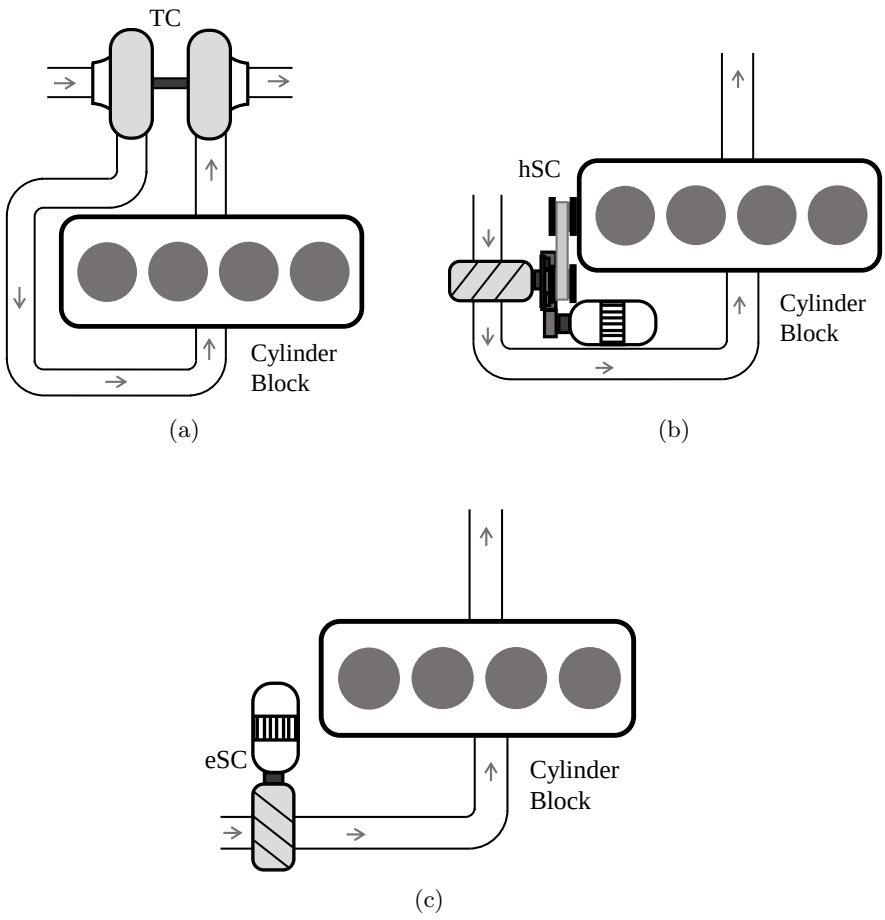

Figure 1.2: Examples of air path configuration, (a) turbocharged engine, (b) hybrid supercharged engine, (c) electric supercharged engine.

engine calibrations such as retarded combustion phasing and fuel enrichment have to be followed to avoid it. Consequently, the engine efficiency drops at highly boosted points causing low off-cycle fuel economy of these engines.

Exhaust Gas Recirculation (EGR), which recirculates part of the engine exhaust gases back into the inlet air charge, can be used for knock mitigation as well as efficiency improvement. Cooled EGR (cEGR) increases gasoline engines efficiency due to lower pumping losses, less heat transfer and higher specific heat ratio of charge mixture [19–22]. For downsized boosted engines or engines with high compression ratio cEGR decreases the knock propensity and enables a more optimal combustion phasing [19, 20, 23, 24]. In addition, at extremely high loads fuel enrichment is used to decrease the exhaust gas temperature and suppress knock. Cooled EGR decreases the exhaust gas temperature and alleviates the need for fuel enrichment [19, 20, 24]. Nevertheless, cEGR benefits come at the cost of slower turbocharged engine air path dynamics and increased engine turbolag. The turbocharger also has to negotiate higher boost pressures with cEGR due to the partial pressure of the

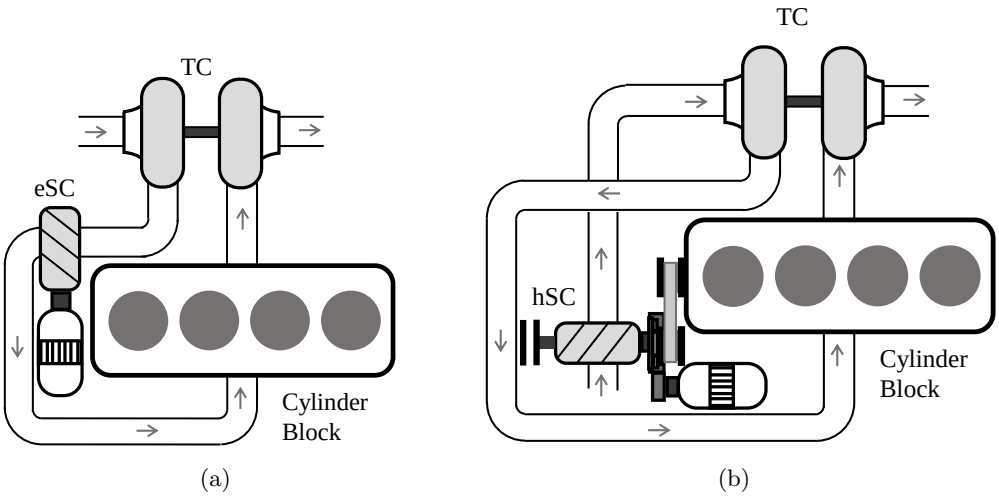

Figure 1.3: Examples of twincharged air path structure, (a) turbo-super configuration with electric supercharger, (b) super-turbo configuration with hybrid supercharger.

residual gases. Moreover, the decreased exhaust gas temperature reduces the available energy for turbocharger acceleration, both these effects contribute to longer turbolag. In this work it is shown that electrifying the engine boosting system in a twincharged or supercharged configuration allows faster boost pressure control and implementing a cooled EGR system without drive-ability concerns.

1.3 Powertrain Hybridization

Hybrid Electric Vehicles (HEVs) use both fuel and batteries to store energy for propulsion. The resulting flexibility in engine operating point selection, in addition to start/stop and regenerative braking, enabled by the electric motor, increases vehicle efficiency and saves fuel. Full powertrain hybridization requires large battery packs and a high voltage electrical system. Consequently, full HEVs are vulnerable to the same drawbacks of EVs such as high cost, battery degradation and additional safety requirements associated with high voltage systems. While full HEVs have high driving range due to the dual energy source, the same feature increases their price relative to EVs. Mild hybridization on the other hand, only partially provides the functionalities of full HEVs, yet it can effectively decrease the conventional powertrains fuel consumption.

1.3.1 Mild Hybridization

A mild hybrid powertrain, typically realized with a low voltage system (<60 V[1]), requires a small battery pack and low power electric machines, therefore, it is cheaper and requires fewer

[1]Industry practice 48 V systems

safety measures. A conventional powertrain can be upgraded to a mild hybrid configuration with minimal cost and modifications.

The electric motor in a mild hybrid system is not capable of propelling the vehicle due to limited available torque, but it can help modify the engine operating points and guide them into more efficient areas. Mild hybrid powertrains also save fuel through reducing the engine idling time. The start/stop systems shut down the engine when the vehicle is stopped. Around 8% fuel consumption reduction is reported over NEDC through start/stop systems [25]. Moreover, the electric motor can recover part of the energy lost in the friction brakes during vehicle deceleration. Up to 16% fuel consumption reduction over the FTP75 drive cycle has been reported using start/stop and regenerative braking combined [26]. That study excluded the benefit from engine operating point adjustment, conducted with optimization based controllers.

The electric power and storage capacity enabled by mild hybridization also enables the use of electrified engine boosting systems or electric turbo generation [27–29], which are not feasible with a conventional 12 V electrical system. The combination of mild hybridization and engine boosting electrification pursued here can significantly improve the performance and fuel economy of a conventional vehicle.

1.3.2 Energy Management Strategies for Hybrid Electric Vehicles

Within an engine with electrified air path and hybrid capabilities, there are multiple electric energy consumers and sources. The supervisory controller of such a system has to decide where and how much to supply the limited available electric power, the air path or the crankshaft.

The ICE efficiency map is nonlinear over its operating range, thus the vehicle fuel consumption depends on the engine operating point. The main goal of a HEV supervisory controller is to shift the engine operating points into a more efficient area. Many different controllers are developed for this target, which are classified as rule-based approaches and optimization-based approaches [30]. Rule-based methods are static controllers and can be implemented in real time, hence they are widely used in industry. The rules are generated offline, often based on heuristics. Two well-known rule-based controllers for serial and parallel HEVs are thermostatic control and load leveling, respectively. The thermostatic control turns the engine on and off based on the battery state of charge, while load leveling uses only the motor at low load, the engine at medium load and both a high load. These controllers do not exploit the full potential of the system in fuel consumption reduction and are not reusable for a different powertrain configuration.

Optimization-based methods use physics-based modeling and optimization techniques to minimize a cost function that can include different performance metrics such as fuel consumption or emissions. The objective cost can be minimized instantaneously like an Equivalent Consumption Minimization Strategy (ECMS), over some receding horizon such

Figure 1.4: Power split supercharger.

as with Model Predictive Control (MPC) or over the full driving profile as in Dynamic Programming (DP). The methods that optimize the fuel consumption over the full driving profile give the global optimum solution, but they cannot be implemented online since they are computationally expensive and need knowledge of future driver demand. Still, they can be used as a measure for evaluating the effectiveness of other methods and developing and improving rule-based methods [31]. In this work both the optimization over the full drive cycle horizon and instantaneous optimization are considered.

1.4 Contributions and Organization

The main focus of this work is a device called a Power Split Supercharger (PSS), shown in Figure 1.4. The PSS consists of a roots type blower, an electric motor, a planetary gear set, a brake, and a bypass valve. This system, introduced in detail in next chapter, can work both as a parallel hybrid powertrain and a variable speed supercharger. The main contributions of this thesis is summarized as follows:

- *Modeling and control design for a twincharged engine with a power split supercharger and a turbocharger*

  The air path of a twincharged engine is a MIMO system with nonlinear dynamics. The throttle valve, wastegate and the supercharger are three main actuators that have to coordinate to manage the air flow into the engine. On the power split supercharger side, the motor torque, bypass valve and the brake are also the three actuators that have to be scheduled using an event-based controller during mode transitions. A physics-based mean value engine model is developed and calibrated to the engine dynamometer steady state and transient data for designing and simulating the engine air path controller. The designed decentralized controller uses the throttle valve to control the intake manifold pressure while it applies a master-slave mechanism for regulating the engine boost pressure. This strategy uses the cheaper actuator (wastegate) during steady state and employs the more expensive actuator (supercharger) as the transient response facilitator. The controller performance is validated on a high fidelity GT-Power engine model. It is demonstrated that the controller can effectively mitigate the engine

turbolag even in the presence of cEGR. The engine mean value modeling along with the vehicle model are presented in Chapter II and the controller design is described in Chapter III. These parts are based on the following work,

  - S. Nazari, J. Siegel, and A. Stefanopoulou, "Control of hybrid boosting in highly diluted internal combustion engines," *accepted to IEEE Transactions on Control Systems Technology*, 2019, [32].

- *Optimal energy management of a mild hybrid electric vehicle with hybrid and electric engine boosting systems*

  Chapter IV investigates the utilization of the power split supercharger and a dual motor mild hybrid system for fuel economy improvement of a vehicle. The dual motor system provides both functionalities of the PSS, electric supercharging and parallel hybrid operation, but with two separate motors. Both systems enable the use of a downsized engine as a competitive counterpart to widely used turbocharged and full hybrid electric powertrains. The optimal control problem for energy management of both configurations on a vehicle with an automatic transmission is formulated and solved using dynamic programming over standard drive cycles. The supercharging versus torque assist share and its sensitivity to the drive cycle, battery size, and compressor efficiency, which influence the availability of electric energy and the losses of electrical and mechanical paths is also investigated. A few causally implementable rules for selecting the single motor system operating mode are found by analysis of the DP solution and their effectiveness is shown by incorporation into the DP formulation and comparison of the predicted fuel consumption. The optimal energy management formulation for the PSS and the dual motor system are published in the following papers,

  - S. Nazari, J. B. Siegel, and A. Stefanopoulou, "Optimal energy management for a mild hybrid vehicle with electric and hybrid engine boosting systems," *IEEE Transactions on Vehicular Technology*, 2019, [33].
  - S. Nazari, J. Siegel, and A. Stefanopoulou, "Optimal energy management for a hybrid electric vehicle with a power split supercharger," in *2018 IEEE Vehicle Power and Propulsion Conference (VPPC)*. IEEE, 2018, pp. 1–6, [34].

- *Online Energy Management of a HEV with Power Split Supercharger*

  The drive cycle fuel consumption minimization, although very useful, is acausal and cannot be implement online. In Chapter V an equivalent consumption minimization strategy is developed to select both the PSS mode and the power split during hybrid mode. The PSS operation is simulated over standard EPA drive cycles with the developed engine mean value and vehicle models and the results are compared to

the DP solution. The simulation results are supplied to the engine dynamometer experimental setup to verify the fuel economy improvement predictions. The online energy management system for the power split supercharger is published in,

- S. Nazari, R. Middleton, J. Siegel, and A. Stefanopoulou, "Equivalent consumption minimization strategy for a power split supercharger," SAE Technical Paper, Tech. Rep., 2019-01-1207, [35].

The vehicle and driveline model used in this study along with a comprehensive study of supercharging influence on drive cycle fuel efficiency of a vehicle are presented in,

- S. Nazari, R. Middleton, K. Sugimori, J. Siegel, and A. Stefanopoulou, "Assessing a hybrid supercharged engine for diluted combustion using a dynamic drive cycle simulation," *SAE Journal of Alternative Powertrains*, 2019, [14].

- *Hybridization requirements with eco-driving*

  Eco-driving and hybridization both save fuel by reducing the energy loss during braking and using the engine efficiently. Considering this similarity, the hybridization requirements are different for the future connected and automated vehicles that can precisely optimize the vehicle velocity profile. Hence the necessary hybridization degree in an automated car following scenario is studied here. The fuel minimization problem is divided into two independent optimizations, one for the velocity profile and the other for the energy management of the PSS. Different motor sizes are considered for the PSS system and the resulting fuel economies are compared to a turbocharged engine and a full hybrid electric powertrain. This study is presented in Chapter VI and is published in the following work,

  - S. Nazari, N. Prakash, J. Siegel, and A. Stefanopoulou, "On the effectiveness of hybridization paired with eco-driving," in *2019 Annual American Control Conference (ACC)*. IEEE, 2019, [36].

  Finally, Chapter VII highlights the major conclusion and possible future work.

CHAPTER II

Modeling Framework

This chapter introduces the models used for control design, simulation, and analysis throughout this thesis. A Mean Value Model (MVM) is developed for a turbocharged spark ignition engine with Low Pressure Exhaust Gas Recirculation (LP-EGR) system, with the main goal of estimating the engine air path dynamics for a wide range of operating points. The MVM steady state and transient performance are compared to the engine dynamometer experimental data. Later, the model for a Power Split Supercharger (PSS) is presented. A short description of a GT-Power [37] engine model and its validation against experimental data is also included. This model is used to develop steady state fuel consumption maps. A vehicle model for a Ford Escape MY2015, along with a driver model are described at the final part of the chapter.

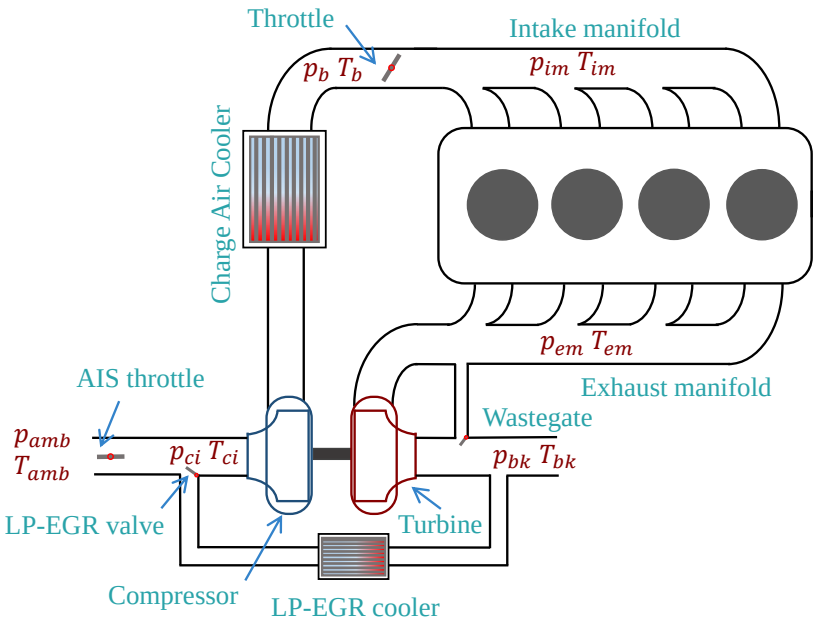

Figure 2.1: Schematic of turbocharged 4 cylinder engine with LP-EGR loop.

2.1 Engine Description

The modeled engine is a 1.6 liter, 4 cylinder four-stroke turbocharged gasoline fueled Spark Ignition Direct Injection (SIDI) engine. Figure 2.1 shows a schematic of the engine and its air path main components including: the cylinder block, intake and exhaust manifolds, turbocharger, Charge Air Cooler (CAC) and EGR intercooler. The geometry of the engine is summarized in Table 2.1.

Various actuators of the engine include: spark timing, fuel injectors, intake and exhaust cam timing, throttle, wastegate and EGR valve. The production sensors in this engine, which is without LP-EGR loop, include intake manifold temperature and pressure, pre-throttle pressure, engine speed and exhaust air fuel ratio sensor. More signals are available in the experimental test setup including pressure and temperature for ambient, compressor outlet, charge air cooler inlet and outlet, and turbine inlet and outlet, in addition to fuel mass flow rate, engine air mass flow rate, crankshaft torque, oxygen concentration before the throttle valve and fast differential pressure measurements across the LP-EGR valve.

2.2 Mean Value Engine Model

Mean value engine models are zero dimensional models with application to analysis, control design and diagnostics. In an MVM parameters and signals are averaged over one or several cycles, therefore, they have a frequency range of $0.1 - 5Hz$ [38]. The term mean value engine model was first used by Elbert Hendricks [39] and nowadays there is a rich literature on developing MVMs. The modeled dynamic states include the turbocharger speed, the pressure inside air path volumes, the EGR mixing dynamics and actuator dynamics. Whereas, the cylinder block, the turbocharger compressor and turbine, intercoolers and the valves are modeled as quasi-steady components. Finally, EGR transport delay and the engine reciprocating operation are modeled as transport delays.

Note that the MVM intends to model the engine air path dynamics, hence only the most important actuators impacting the engine air path are included in the model, which are the throttle valve, wastegate and EGR valve and it is assumed that the rest of actuators are always coordinated based on the baseline strategy, therefore their movement effect is embedded inside the model. In the following sections the models for different components

Table 2.1: Geometry of the modeled engine [2].

Attribute	Value	Units
Displacement	1.6	L
Compression ratio (geometric)	10:1	–
Bore	81.5	mm
Stroke	79	mm
Connecting rode length	131.5	mm

are described in details.

2.2.1 Flow Restriction Model

The throttle valve, wastegate, low pressure EGR valve, and the exhaust pipe, over which the flow pressure drops, are modeled as flow restriction components. Assuming that the sum of flow potential and kinetic energy remains constant when passing through a restriction, it can be implied that the flow enthalpy and hence its temperature remain constant from conservation of energy,

$$T_{\text{us}} = T_{\text{ds}} \tag{2.1}$$

where T_{us} and T_{ds} refer to the upstream and downstream temperature of the flow restriction component. Compressible turbulent flow model with linear region is used to estimate the mass flow across the flow restrictions [38],

$$\dot{m}(p_{\text{us}}, T_{\text{us}}, p_{\text{ds}}, A_{\text{eff}}) = A_{\text{eff}} \frac{p_{\text{us}}}{\sqrt{RT_{\text{us}}}} \Psi_{\text{li}}\big(\Pi(\frac{p_{\text{ds}}}{p_{\text{us}}})\big) \tag{2.2a}$$

$$\Pi(\frac{p_{\text{ds}}}{p_{\text{us}}}) = \max\big(\frac{p_{\text{ds}}}{p_{\text{us}}}, (\frac{2}{\gamma+1})^{\frac{\gamma}{\gamma-1}}\big) \tag{2.2b}$$

$$\Psi_0(\Pi) = \sqrt{\frac{2\gamma}{\gamma-1}\big(\Pi^{\frac{2}{\gamma}} - \Pi^{\frac{\gamma+1}{\gamma}}\big)} \tag{2.2c}$$

$$\Psi_{\text{li}}(\Pi) = \begin{cases} \Psi_0(\Pi) & \text{if} \quad \Pi \le \Pi_{\text{li}}, \\ \Psi_0(\Pi_{\text{li}}) \frac{1-\Pi}{1-\Pi_{\text{li}}} & \text{otherwise} \end{cases} \tag{2.2d}$$

where, p_{us} and p_{ds} stand for the upstream and downstream pressure, γ is the ratio of specific heats, R is the universal gas constant, and A_{eff} is the restriction effective area. $\Psi_{\text{li}}(\Pi)$ is used in (2.2a) instead of $\Psi_0(\Pi)$ to avoid infinite derivative when the ratio $p_{\text{ds}}/p_{\text{us}}$ is close to unity and satisfy the Lipschitz continuity condition, which is tied to the existence and uniqueness of differential equation solutions. The effective areas for wastegate and LP-EGR valve are given as the model input but for the throttle, which is a butterfly valve, the effective area is related to its opening angle using a quadratic polynomial.

2.2.2 Manifold Filling Dynamics

All volumes in the engine air path, including the intake and the exhaust manifolds are assumed as lumped volumes, meaning that all spatial information of the gas state is lumped into just one point. It is also assumed that the gas is ideal (i.e. $pV = mRT$) and the specific constant volume and constant pressure heat of the charge, C_v and C_p respectively, are constant.

Isothermal model, which assumes no temperature change in the system, is used for modeling the volumes. The differential equation for pressure is derived through differentiating

the ideal gas law,

$$\frac{dp}{dt} = \frac{RT}{V}\frac{dm}{dt}. \tag{2.3}$$

Conservation of mass implies that the rate of change of the mass in a volume is equal to the difference between inlet and outlet mass flows,

$$\frac{dm}{dt} = \dot{m}_{\text{in}} - \dot{m}_{\text{out}}. \tag{2.4}$$

Combining (2.3) and (2.4) yields the following model for manifold filling dynamics,

$$\frac{dp}{dt} = \frac{RT}{V}(\dot{m}_{\text{in}} - \dot{m}_{\text{out}}) \tag{2.5}$$

where p stands for pressure and V is the volume. Furthermore,

$$T = T_{\text{in}} = T_{\text{out}}. \tag{2.6}$$

Although this model violated the conservation of energy, due to the constant temperature assumption, it is capable of capturing the pressure dynamics in different volumes of the engine air path [38].

2.2.3 Cylinder Model

In this section quasi-steady models are introduced for estimating the cylinders inlet mass flow rate, produced torque and exhaust temperature. It is assumed that the engine maintains MBT spark timing and nominal inlet and exhaust valve timings in all operating points hence these actuators are not included in the cylinders block model as independent inputs.

2.2.3.1 Cylinder Mass Flow

The mass flow rate into the cylinders, $\dot{m}_{\text{cyl}}$, is related to the engine volumetric efficiency, η_{vol}, as follows:

$$\dot{m}_{\text{cyl}}(p_{\text{im}}, \omega_e, x_{\text{egr}}) = \eta_{\text{vol}}(p_{\text{im}}, \omega_e, x_{\text{egr}})\frac{V_D \omega_e p_{\text{im}}}{n_r R T_{\text{im}}} \tag{2.7}$$

where p_{im} is the intake manifold pressure, T_{im} is the intake manifold temperature, ω_e is the engine rotational speed, x_{egr} is the EGR mass fraction inside intake manifold, V_D is the engine displacement, and n_r is the number of engine revolutions per engine cycle which is equal to 2 for a four-stroke engine. The engine volumetric efficiency is a function of many parameters such as engine speed, intake manifold pressure, exhaust manifold pressure and intake manifold temperature. However, in this work only its dependency on engine

speed, intake manifold pressure and EGR concentration is included. The engine volumetric efficiency is regressed using the following equation,

$$\eta_{vol}(p_{\text{im}}, \omega_e, x_{\text{egr}}) = (1 + k_0 x_{\text{egr}})\big(k_1 + k_2\omega_e + (k_3 + k_4\omega_e)p_{\text{im}} + k_5 {p_{\text{im}}}^2\big) \tag{2.8}$$

where k_i's are constant coefficients. EGR mass fraction is defined as the ratio of EGR mass, m_{egr}, to the total mass of the charge inside the intake manifold, $m_{\text{egr}} + m_{\text{air}}$,

$$x_{\text{egr}} = \frac{m_{\text{egr}}}{m_{\text{air}} + m_{\text{egr}}}. \tag{2.9}$$

2.2.3.2 Produced Torque

The engine Indicated Mean Effective Pressure, IMEP, is modeled as follows,

$$\text{IMEP}(p_{\text{im}}, \omega_e, x_{\text{egr}}) = (1 + k_0 x_{\text{egr}})\big(k_1 + k_2 p^*_{\text{im}} + k_3\omega_e + k_4 {p^*}^2_{\text{im}} + k_5 p^*_{\text{im}}\omega_e + k_6\omega_e^2\big) \tag{2.10}$$

in which p^*_{im} is the partial pressure of the fresh charge inside intake manifold computed using Dalton's law of partial pressures,

$$p^*_{\text{im}} = (1 - y_{\text{egr}})p_{\text{im}} \tag{2.11a}$$

$$y_{\text{egr}} = \frac{\frac{x_{\text{egr}}}{M_{\text{egr}}}}{\frac{x_{\text{egr}}}{M_{\text{egr}}} + \frac{1 - x_{\text{egr}}}{M_{\text{air}}}} \tag{2.11b}$$

where y_{egr} is the mole fraction of burned residuals inside intake manifold, M_{egr} is the burned residuals molar mass and M_{air} is the air molar mass.

The cylinder outlet mass flow rate, $\dot{m}_{\text{cyl,out}}$, is computed as the sum of inlet charge mass flow rate and the engine fuel flow rate. The engine fuel flow rate, $\dot{m}_f$, is computed assuming stoichiometric air fuel ratio, AFR_{sto}, throughout the engine operating region

$$\dot{m}_f = \frac{\dot{m}_{\text{cyl}}}{A\text{FR}_{\text{sto}}} \tag{2.12}$$

$$\dot{m}_{\text{cyl,out}} = \dot{m}_{\text{cyl}} + \dot{m}_f. \tag{2.13}$$

The engine Pumping Mean Effective Pressure (PMEP) is computed as the difference between the intake manifold pressure and the exhaust manifold pressure, p_{em},

$$\text{PMEP}(p_{\text{im}}, p_{\text{em}}) = p_{\text{em}} - p_{\text{im}}. \tag{2.14}$$

The Friction Mean Effective Pressure (FMEP) is regressed as follows:

$$\mathrm{FMEP}(p_{\mathrm{im}}, \omega_e) = k_1 + k_2 p_{\mathrm{im}} + k_3 \omega_e + k_4 p_{\mathrm{im}}^2 + k_5 p_{\mathrm{im}} \omega_e + k_6 \omega_e^2. \tag{2.15}$$

Finally, the engine BMEP is computed using the engine IMEP, PMEP and FMEP as,

$$\mathrm{BMEP}(p_{\mathrm{im}}, \omega_e, x_{\mathrm{egr}}) = \mathrm{IMEP} + \mathrm{PMEP} - \mathrm{FMEP}. \tag{2.16}$$

The engine BMEP is calculated using measured engine torque in the engine dynamometer setup.

2.2.3.3 Exhaust Manifold Temperature

The gas temperature entering the exhaust manifold, T_{em}, is regressed against the intake manifold temperature, engine speed, EGR concentration, and the partial pressure of air in the intake manifold as,

$$\begin{aligned} T_{\mathrm{em}}(p_{\mathrm{im}}, \omega_e, T_{\mathrm{im}}, x_{\mathrm{egr}}) = (1 + k_0 x_{\mathrm{egr}})\big(k_1 + k_2 p_{\mathrm{im}}^* + \\ k_3 \omega_e + k_4 p^{*2}_{\mathrm{im}} + k_5 p_{\mathrm{im}}^* \omega_e + k_6 T_{\mathrm{im}}\big). \end{aligned} \tag{2.17}$$

2.2.3.4 Engine Reciprocating Behavior

The engine reciprocating performance is modeled by including delays between cylinder inlet and outlet variables, such that the engine produced BMEP is achieved after Induction to Power Stroke (IPS) delay and the engine exhaust temperature and outlet mass flow rate are gained after Induction to Exhaust Gas (IEG) delay [40],

$$\tau_{\mathrm{IPS}} = \frac{2\pi}{\omega_e} \tag{2.18a}$$

$$\tau_{\mathrm{IEG}} = \frac{3\pi}{\omega_e} \tag{2.18b}$$

where ω_e should be in rad/s.

2.2.4 Turbocharger Model

In an MVM compressor and turbine of the turbocharger are modeled as quasi-steady constant specific heat devices, meaning that their thermodynamic outputs can be computed from their performance maps. The performance maps commonly are defined as the compressor/turbine corrected/reduced mass flow rate and isentropic efficiency for different pressure

ratios and corrected or reduced speeds,

$$\dot{m} = f_1(p_{\text{us}}, p_{\text{ds}}, T_{\text{us}}, \omega_{\text{tc}}) \tag{2.19a}$$

$$\eta = f_2(p_{\text{us}}, p_{\text{ds}}, T_{\text{us}}, \omega_{\text{tc}}) \tag{2.19b}$$

where ω_{tc} is the turbocharger speed. Modeling the turbocharger for an engine MVM mostly includes finding the functions f_1 and f_2, and computing the outlet temperature and the component power using the mass flow rate and the isentropic efficiency.

2.2.4.1 Compressor

The compressor downstream temperature can be computed using the following equation,

$$T_{\text{ds}} = T_{\text{us}} + \frac{T_{\text{us}}}{\eta_c}\left(\left(\frac{p_{\text{ds}}}{p_{\text{us}}}\right)^{\frac{\gamma-1}{\gamma}} - 1\right) \tag{2.20}$$

where η_c is the isentropic efficiency. The compressor consumed power, P_{cmp}, is computed as:

$$P_{\text{cmp}} = \dot{m} C_p (T_{\text{ds}} - T_{\text{us}}) \tag{2.21}$$

In order to estimate the compressor mass flow rate a modified form of the model introduced by Jensen et al. [41] is used. This model uses dimensionless compressor energy and flow coefficients, Ψ and Φ respectively, defined as follows,

$$\Psi = \frac{C_p T_{\text{us}}\left(\frac{p_{\text{ds}}}{p_{\text{us}}}\right)^{\frac{\gamma-1}{\gamma}} - 1}{\frac{U^2}{2}} \tag{2.22a}$$

$$U = \frac{\pi}{60}\omega_{\text{cor}} D \tag{2.22b}$$

$$\Phi = \frac{4}{\pi}\frac{R T_{\text{us}}}{p_{\text{us}}}\frac{\dot{m}_{\text{cor}}}{U D^2} \tag{2.23}$$

where ω_{cor} is the compressor corrected speed in rpm, $\dot{m}_{\text{cor}}$ is the corrected mass flow rate, D is the compressor impeller diameter, R is the universal gas constant and U is the blade tip speed. The corrected mass flow rate and corrected speed are usually used in compressor

maps, which are defined as,

$$\omega_{\text{cor}} = \frac{\omega_{\text{tc}}}{\sqrt{\frac{T_{\text{us}}}{T_{\text{ref}}}}} \tag{2.24a}$$

$$\dot{m}_{\text{cor}} = \frac{\dot{m}\sqrt{\frac{T_{\text{us}}}{T_{\text{ref}}}}}{\frac{p_{\text{us}}}{p_{\text{ref}}}} \tag{2.24b}$$

where p_{ref} and T_{ref} are the reference pressure and temperature. The model fitted to the compressor mass flow rate is in the following form

$$\Phi = \frac{k_1(\text{Ma}) + k_2(\text{Ma})\Psi}{k_3(\text{Ma})\Psi + 1} \tag{2.25a}$$

$$\text{Ma} = \frac{U}{\sqrt{\gamma R T_{\text{us}}}} \tag{2.25b}$$

$$k_1 = k_{11} + k_{12}\text{Ma} + k_{13}\text{Ma}^2 + k_{14}\text{Ma}^3 \tag{2.25c}$$

$$k_i = k_{i1} + k_{i2}\text{Ma} + k_{i3}\text{Ma}^2 \qquad i = 2, 3 \tag{2.25d}$$

where Ma is the blade tip mach number.

It is possible that during transient operation of the engine, compressor pressure ratio drops to lower than unity. In this condition the compressor acts as a restriction, so it is necessary to include a model for overblown compressor to estimate the mass flow rate in this condition [37],

$$\dot{m}_{\text{res}} = \dot{m}_0 + a(1 - \text{PR})^b \tag{2.26}$$

where $\dot{m}_0$ is the compressor mass flow rate for pressure ratio equal to 1, PR is the compressor pressure ratio and a and b are constant coefficients.

Equation (2.27a) to (2.27d) describe the model used to estimate the compressor efficiency. The regression first correlates the dependence peak efficiency, η^*, and the corresponding pressure ratio, PR^*, at peak efficiency to compressor corrected speed, and then uses the functional form of Eq. (2.27c) to calculate the compressor isentropic efficiency,

$$\text{PR}^* = a_{11} + a_{12}\omega_{\text{cor}} + a_{13}\omega_{\text{cor}}^2 \tag{2.27a}$$

$$\eta^* = a_{21} + a_{22}\omega_{\text{cor}} + a_{23}\omega_{\text{cor}}^2 \tag{2.27b}$$

$$\eta_c = \begin{cases} k_1(\text{PR} - \text{PR}^*)^2 + k_2(PR - PR^*) + \eta^* & \text{if } PR \le PR^* \\ k_3(PR - PR^*)^2 + k_4(PR - PR^*) + \eta^* & \text{otherwise} \end{cases} \tag{2.27c}$$

$$k_i = k_{i1} + k_{i2}\omega_{\text{cor}} + k_{i3}\omega_{\text{cor}}^2 + k_{i4}\omega_{\text{cor}}^3 \tag{2.27d}$$

2.2.4.2 Turbine

The turbine downstream temperature can be computed using the turbine isentropic efficiency, η_t, as follows

$$T_{\text{ds}} = T_{\text{us}} - \eta_t T_{\text{us}} \left(1 - \left(\frac{p_{\text{ds}}}{p_{\text{us}}} \right)^{\frac{\gamma-1}{\gamma}} \right). \tag{2.28}$$

The turbine produced power, P_{trb}, is computed as,

$$P_{\text{trb}} = \dot{m} C_p (T_{\text{us}} - T_{\text{ds}}). \tag{2.29}$$

The standard model for compressible flow through a restriction is proposed to model the turbine mass flow,

$$\Pi_t = \frac{p_{\text{ds}}}{p_{\text{us}}} \tag{2.30a}$$

$$\Pi(\Pi_t) = \max(\Pi_t, \left(\frac{2}{\gamma + 1} \right)^{\frac{\gamma}{\gamma-1}}) \tag{2.30b}$$

$$\Psi(\Pi) = \sqrt{\frac{2\gamma}{\gamma - 1} \left(\Pi^{\frac{2}{\gamma}} - \Pi^{\frac{\gamma+1}{\gamma}} \right)} \tag{2.30c}$$

$$\dot{m}_{\text{red}} = A_{\text{eff}} . \Psi(\Pi) \tag{2.30d}$$

where, $\dot{m}_{\text{red}}$ is the reduced turbine mass flow rate. The effective area, A_{eff}, is adjusted to acquire the best fit [38, 41, 42]. In this work the effective area is fitted as,

$$A_{\text{eff}} = k_1 + k_2 \omega_{\text{red}} + (k_3 + k_4 \omega_{\text{red}}) \Pi_t \tag{2.31}$$

ω_{red} is the turbine reduced speed. The reduced parameters for a turbine are defined as,

$$\omega_{\text{red}} = \frac{\omega_{\text{tc}}}{\sqrt{T_{\text{us}}}} \tag{2.32a}$$

$$\dot{m}_{\text{red}} = \frac{\dot{m}_{\text{trb}} \sqrt{T_{\text{us}}}}{p_{\text{us}}}. \tag{2.32b}$$

The turbine efficiency is estimated using the Blade Speed Ratio (BSR) parameter [43], defined as,

$$\text{BSR} = \frac{\pi D \omega_{\text{red}}}{60 \sqrt{2 C_p (1 - \Pi_t^{\frac{\gamma-1}{\gamma}})}} \tag{2.33}$$

where D is the turbine impeller diameter. The turbine efficiency is approximated as a

quadratic polynomial in BSR,

$$\eta_t = k_1 + k_2 \mathrm{BSR} + k_3 \mathrm{BSR}^2 \tag{2.34a}$$

$$k_1 = k_{11} + k_{12}\omega_{\mathrm{red}} + k_{13}\omega_{\mathrm{red}}^2 \tag{2.34b}$$

$$k_i = k_{i1} + k_{i2}\omega_{\mathrm{red}} \qquad i = 2, 3. \tag{2.34c}$$

2.2.4.3 Turbocharger Shaft Dynamics

The turbocharger shaft speed is computed using the power balance between the compressor and the turbine,

$$\dot{\omega}_{\mathrm{tc}} = \frac{1}{J_{\mathrm{tc}}\omega_{\mathrm{tc}}}(P_{\mathrm{trb}} - P_{\mathrm{cmp}}) \tag{2.35}$$

where J_{tc} is the turbocharger shaft inertia.

2.2.5 Charge Air Cooler

The charge air cooler is modeled as a zero pressure drop device and its outlet temperature is computed as follows [44, 45],

$$T_{\mathrm{out}} = T_{\mathrm{in}} - \eta_{\mathrm{ic}}(T_{\mathrm{in}} - T_{\mathrm{ic}}^*) \tag{2.36a}$$

$$\eta_{\mathrm{in}} = k_1 + k_2 \dot{m}_c \tag{2.36b}$$

where the efficiency of temperature exchange, η_{ic} is linearly dependent on air flow, $\dot{m}_c$, and T_{ic}^* is the set point temperature of the cooler.

2.2.6 EGR Transport Delay and Mixing

Spark ignition engines run with stoichiometric air fuel ratio. High concentration of EGR can cause misfires and overestimation of EGR levels might lead to knock. In low pressure EGR systems, there is a long pipe between the EGR valve and the intake manifold and little mixing takes place in this pipe (see Figure 2.1), whereas the mixing is high within the intake manifold due to the geometry of intake manifold and the turbulence created by the throttle valve. Thus the EGR dynamics within inlet air path can be divided into two sub-models: the EGR dynamics from the air path inlet to the throttle valve and the EGR dynamics inside the intake manifold (after the throttle before the cylinders). In the following sections each model is described in details.

2.2.6.1 EGR Dynamics from Air Path Inlet to Throttle Valve

The flow inside a pipe can be modeled by a Partial Differential Equation (PDE) [46], discretization of both time and pipe length is required to solve this PDE, though. In this work a simplified approach is used to capture these dynamics, which is a transport delay followed by a mixing volume [38], as follows:

$$\frac{dx_{\text{egr},\theta}}{dt} = \frac{RT_b}{p_b V_{\text{mix}}} \dot{m}_{\text{cmp}} (x_{\text{egr,in}}(t - t_d) - x_{\text{egr},\theta}) \tag{2.37}$$

where $x_{\text{egr,in}}$ is the EGR concentration at the air path inlet and $x_{\text{egr},\theta}$ is the EGR concentration before the throttle valve. The variable $\dot{m}_{\text{cmp}}$ is the compressor mass flow rate (it is assumed that the mass flow rate of the mixing volume is equal to the compressor mass flow rate), p_b and T_b are pressure and temperature before the throttle valve, R is the universal gas constant, t stands for time and V_{mix} is the mixing volume, which is used as a tuning parameter to fit the model to the experiments. The transport delay, t_d, is the time that the cooled burned gases need to pass the inlet pipes and reach the throttle valve. This parameter can be estimated using the charge velocity inside the intake pipes, v, and pipes length, L,

$$t_d = \frac{L}{v} \tag{2.38a}$$

$$v = \frac{\dot{m}_{\text{cmp}} R T_b}{p_b A} \tag{2.38b}$$

where A is the inlet pipe cross section area. The parameter L is also used to fit the model to the experimental data. Figure 2.2(a) compares the modeled EGR dynamics of (2.37) to the engine data and Figure 2.2(b) shows the engine BMEP during the same time span. This

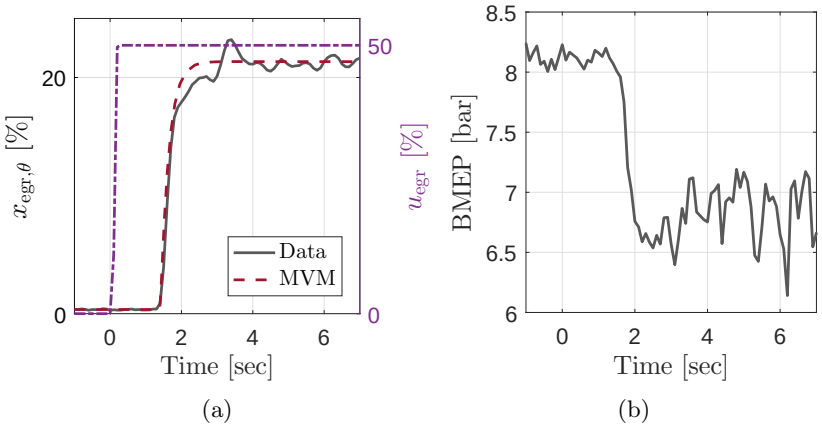

Figure 2.2: EGR transport delay and mixing, (a) EGR valve lift and pre-throttle EGR concentration, (b) corresponding variation in engine BMEP.

data was taken at 1750 rpm constant engine speed. A wide band oxygen sensor, placed before the throttle valve, was used for calculating the EGR concentration. It is assumed that the sensor lag is negligible compared to the transport delay. It is clear from the figure that the predicted dynamics is in agreement with the experimental data.

2.2.6.2 EGR Dynamics Inside Intake Manifold

Perfect mixing model for EGR and fresh charge is assumed inside the intake manifold,

$$\frac{dx_{\text{egr}}}{dt} = \frac{RT_{\text{im}}}{p_{\text{im}}V_{\text{im}}}\dot{m}_{\theta}(x_{\text{egr},\theta} - x_{\text{egr}}) \tag{2.39}$$

in which x_{egr} is the EGR concentration inside the intake manifold and $\dot{m}_{\theta}$ is the throttle mass flow rate.

2.3 Actuators Dynamics

The air path actuators that are modeled include throttle valve, wastegate and LP-EGR valve. Simple first order linear models were used for these actuators dynamics,

$$\dot{\theta}_t + \frac{1}{\tau_t}\theta_t = \frac{1}{\tau_t}u_t \tag{2.40a}$$

$$\dot{\theta}_{\text{wg}} + \frac{1}{\tau_{\text{wg}}}\theta_{\text{wg}} = \frac{1}{\tau_{\text{wg}}}u_{\text{wg}} \tag{2.40b}$$

$$\dot{\theta}_{\text{egr}} + \frac{1}{\tau_{\text{egr}}}\theta_{\text{egr}} = \frac{1}{\tau_{\text{egr}}}u_{\text{egr}}. \tag{2.40c}$$

The time constants τ_t, τ_{wg} and τ_{egr} are respectively selected as 40 ms, 125 ms and 40 ms [45].

2.4 Mean Value Model Validation

2.4.1 Steady State Validation

Figure 2.3 compares the mean value model produced BMEP, air flow rate, intake manifold pressure, exhaust manifold pressure and exhaust manifold temperature to the experimental data at different engine speeds and cEGR concentrations. For generating these results the throttle valve position from experiments is directly fed into the mean value model but due to the uncertainty in wastegate valve position (no feedback from wastegate position was available [47]) the wastegate valve is controlled to match the measured boost pressure. These results confirm that the MVM is capable of predicting the engine steady state performance everywhere with reasonable error considering the wide range of operation and the model simplicity.

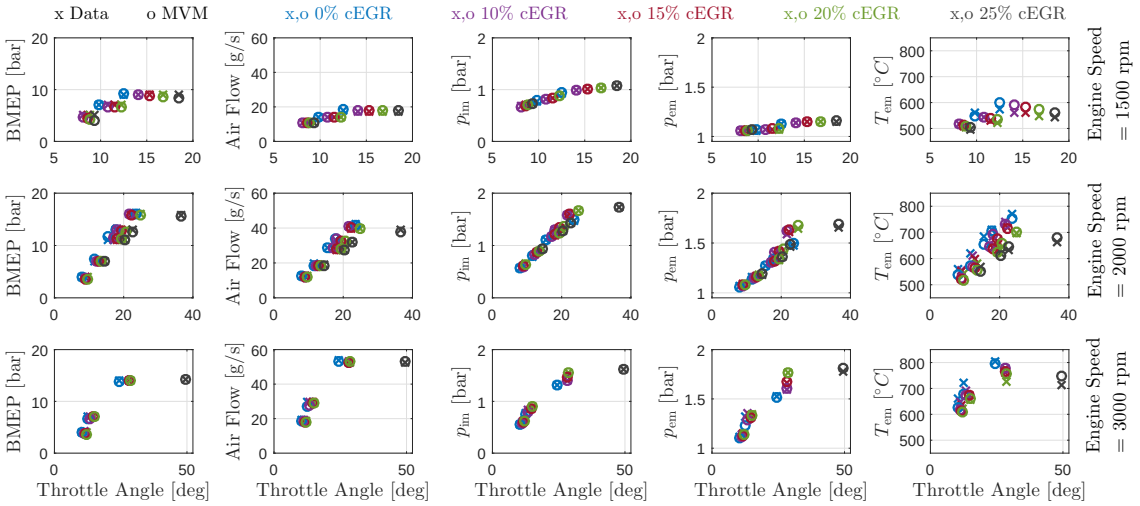

Figure 2.3: Comparing MVM steady state output to engine data for different cEGR concentrations and engine speeds. Respectively from left, produced BMEP, air flow, intake manifold pressure, exhaust manifold pressure and exhaust manifold temperature. Top row 1500 rpm engine speed, middle row 2000 rpm engine speed, and bottom row 3000 rpm engine speed.

2.4.2 Transient Response Validation

Figure 2.4 compares the experimental versus simulated baseline engine transient response to a load tip-in from a low load point to high load at 2000 rpm engine speed. Figure 2.4(a) displays the BMEP response and Figure 2.4(b) shows the intake manifold pressure response. Similar to steady state simulations, the throttle angle is directly fed into the simulation while the wastegate is controlled to match the measured boost pressure. This transient is without cEGR and the EGR valve is kept closed during the entire transient. These results confirm the mean value model ability in predicting the baseline engine dynamics with a good accuracy for the comparisons given in this work.

Inspecting the engine transient response two different features are detectable in both BMEP and intake manifold pressure responses marked on Figure 2.4(b).

- Part I, is the almost instantaneous response to opening the throttle valve. When the throttle valve opens, more air flows into the intake manifold rapidly till the intake manifold pressure reaches around the ambient pressure. This process, governed by the manifold filling dynamics, is quick and causes a fast jump in the engine produced BMEP.

- Part II, which is slower in intake manifold pressure rise, is due to the turbocharger acceleration. In this phase the turbocharger speed is increasing to produce higher boost pressure. This process depends on the turbocharger speed dynamics, which is slower relatively and is called the turbolag.

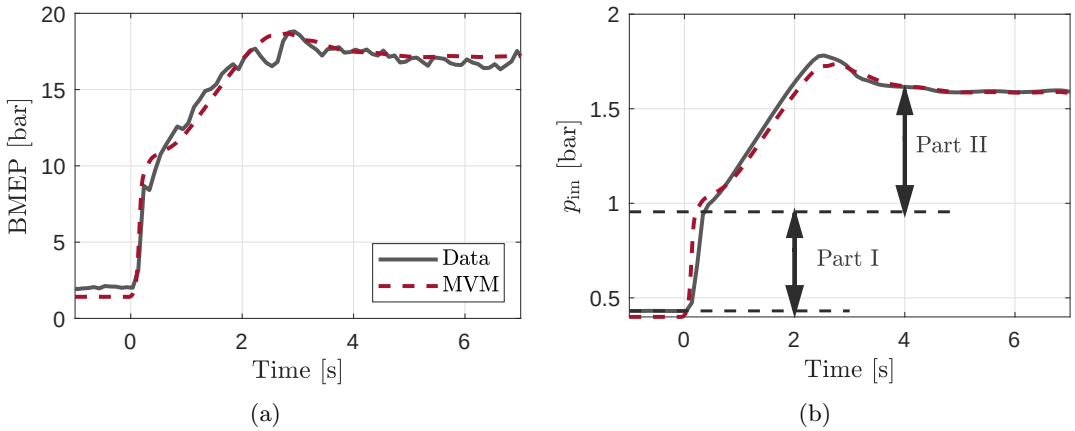

Figure 2.4: Transient performance comparison of the MVM against engine data at 2000 rpm constant engine speed, (a) BMEP response, (b) intake manifold pressure response.

2.5 Power Split Supercharger

The details of the Power Split Supercharger (PSS) are shown in Figure 2.5 including a planetary gear set, a motor, a roots type supercharger, a bypass valve and a brake clutch. The supercharger is directly connected to the sun gear, the motor is connected to the ring gear through an idler gear and the carrier is connected to the engine crankshaft through a set of belt and pulleys. The supercharger is a roots type blower with peak pressure ratio of 2.4, maximum flow rate of 575 kg/h and maximum rotor speed of 24000 rpm. The maximum efficiency of the device is 74%. It is sold commercially as a V400 [48]. The electric motor has a peak power of 12 kW and continuous power of 9 kW and uses a 48 V system.

This hybrid system can operate at different operating modes through controlling the motor, the supercharger bypass valve, and the brake, which are classified into two operating

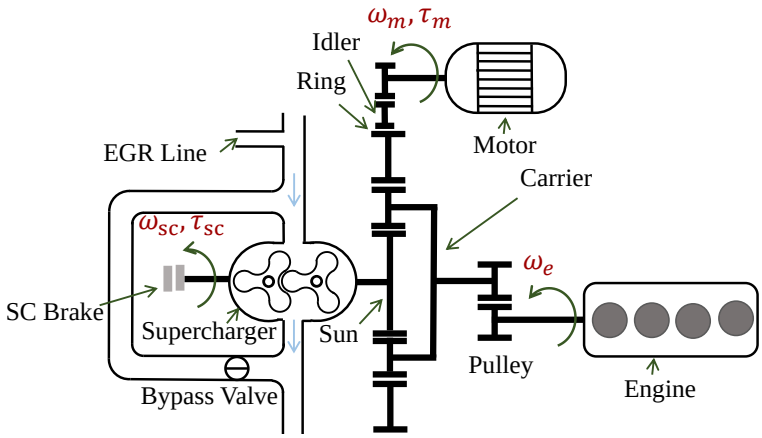

Figure 2.5: Power split supercharger with flow path and mechanical connection details.

modes of boosting and torque assist in this work. In boosting mode the supercharger boosts the engine inlet charge while in torque assist mode the motor can directly supply or draw torque from the engine crankshaft for start/stop, regenerative braking, generation or assisting the crankshaft during acceleration. The gear set equations of motion in each of these modes are described below.

2.5.1 Gear Set Equations of Motion

2.5.1.1 Torque Assist Mode

In torque assist mode, the following equation is used to compute the crankshaft acceleration,

$$I_t \frac{d}{dt}\omega_e = \tau_e - \tau_{\text{aux}} - \tau_{\text{tcp}} - \tau_{\text{cch}} - \frac{n_{\text{im}} n_{\text{ri}} (g_S + g_R)}{g_R \eta_{\text{gs}}} \tau_m \tag{2.41}$$

where τ_m is the motor torque, τ_{aux} is the auxiliaries torque, τ_{cch} is the torque converter clutch torque (from the drivetrain), τ_{tcp} is the torque converter pump torque, g_S is the sun gear numbers in the planetary gear set, g_R is the ring gear numbers, n_{im} is the idler to motor gear ratio, n_{ri} is the ring to idler gear ratio, η_{gs} is the gear set efficiency as follows,

$$\eta_{\text{gs}} = \eta_{\text{im}}^{\text{sgn}(\kappa_1)} \eta_{\text{ri}}^{\text{sgn}(\kappa_2)} \eta_{\text{rp}}^{\text{sgn}(F)} \tag{2.42}$$

where η_{im}, η_{ri} and η_{rp} are respectively idler to motor, ring to idler and ring to planets gear efficiency. sgn denotes the sigmoid function, and κ_1, κ_2 and F are defined as follows,

$$\kappa_1 = (I_m \dot{\omega}_m - \tau_m) \eta_{\text{im}}^{-\text{sgn}(\kappa_1)} \tag{2.43a}$$

$$\kappa_2 = (\kappa_1 n_{\text{im}} + \frac{I_i}{n_{\text{im}}} \dot{\omega}_m) \eta_{\text{ri}}^{-\text{sgn}(\kappa_2)} \tag{2.43b}$$

$$F = (\kappa_2 n_{\text{ri}} + \frac{I_r}{n_{\text{im}} n_{\text{ri}}} \dot{\omega}_m) \frac{\eta_{\text{rp}}^{-\text{sgn}(F)}}{g_R} \tag{2.43c}$$

The total inertia of the engine and rotary parts of the PSS system, I_t, is computed as follows,

$$I_t = I_e + I_c + \frac{(g_S + g_R)^2}{g_R^2} (I_m \frac{(n_{\text{im}} n_{\text{ri}})^2}{\eta_{\text{gs}}} + I_i \frac{n_{\text{ri}}^2}{\eta_{\text{ir}}^{\text{sgn}(\kappa_2)} \eta_{\text{rp}}^{\text{sgn}(F)}} + I_r \frac{1}{\eta_{\text{rp}}^{\text{sgn}(F)}}) \tag{2.44}$$

in which, I_c is the carrier gear inertia, I_i is the idler gear inertia, I_r is the ring gear inertia and I_m is the motor inertial.

In this mode the motor speed is related to the crank speed as follows,

$$\omega_m = \frac{n_{\text{ri}} n_{\text{im}} (g_S + g_R)}{n_p g_R} \omega_e. \tag{2.45a}$$

2.5.1.2 Boosting Mode

During the boosting mode the supercharger brake is released, the bypass is closed and the motor can control the supercharger speed and hence its produced boost pressure independently of the crankshaft speed. The planetary gear set equations of motion in this mode are in form of,

$$\tau_m - (I_m + \frac{I_i \eta_{\text{im}}^{\text{sgn}(\kappa_1)}}{n_{\text{im}}^2} + \frac{I_r \eta_{\text{im}}^{\text{sgn}(\kappa_1)} \eta_{\text{ri}}^{\text{sgn}(\kappa_2)}}{n_{\text{im}}^2 n_{\text{ri}}^2}) \dot{\omega}_m + \frac{F g_R \eta_{\text{gs}}}{n_{\text{im}} n_{\text{ri}}} = 0 \tag{2.46a}$$

$$\tau_e - \tau_{\text{tcp}} - \tau_{\text{cch}} - \tau_{\text{aux}} - F(g_S + g_R) - (I_c + J_e)\dot{\omega}_e = 0 \tag{2.46b}$$

$$\dot{\omega}_e - \frac{g_R \dot{\omega}_m}{(n_{\text{im}} n_{\text{ri}})(g_S + g_R)} - \frac{g_S \dot{\omega}_{\text{sc}}}{g_S + g_R} = 0 \tag{2.46c}$$

$$F g_S \eta_{\text{ps}}^{\text{sgn}(F)} - \tau_{\text{sc}} - I_{\text{sc}} \dot{\omega}_{\text{sc}} = 0 \tag{2.46d}$$

in which η_{ps} is the planet to sun gear efficiency. Note that the pulley ratio is equal to unity and its power transmission efficiency is assumed to be 100%.

2.5.2 Supercharger and Bypass Model

A third order polynomial is used to regress the supercharger corrected mass flow, $\dot{m}_{\text{cor}}$, versus the corrected speed, ω_{cor}, and pressure ratio, PR_{sc},

$$\dot{m}_{\text{cor}} = k_1 + k_2 \text{PR}_{\text{sc}} + k_3 \omega_{\text{cor}} + k_4 \text{PR}_{\text{sc}}^2 + k_5 \text{PR}_{\text{sc}} \omega_{\text{cor}} + k_6 \text{PR}_{\text{sc}}^3 \tag{2.47}$$

Figure 2.6 compares the fitted regression to the manufacturer supplied map.

A look up table based on the supercharger corrected speed and pressure ratio is used to compute its torque, τ_{sc},

$$\tau_{\text{sc}} = \Gamma(\text{PR}_{\text{sc}}, \omega_{\text{cor}}) \tag{2.48}$$

Compressible turbulent flow model (2.1) to (2.2d) is used to model the flow through the bypass valve with a 1^{st} order response time of 40 ms.

2.6 GT-Power Engine Model

A GT-Power model of the baseline engine was constructed following a framework previously used at The University of Michigan [49], with a semi-predictive Wiebe function

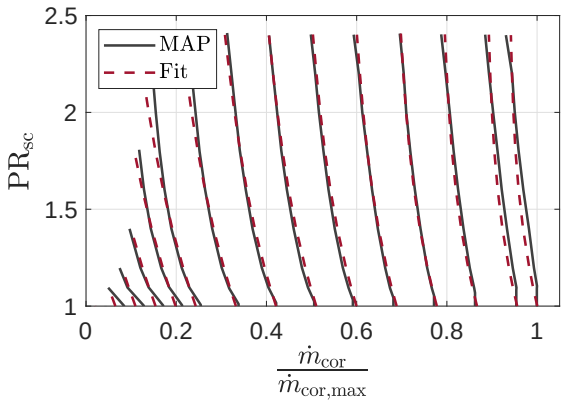

Figure 2.6: Supercharger mass flow rate model comparison to the device map. The individual lines are constant speed data.

combustion model derived from the literature [50] and tuned to experimental data. This model captures the 1-D manifold gas dynamics, valve lift and port flow behavior, heat transfer, turbocharger dynamics, knock onset and other details necessary to predict engine performance. Figure 2.7 compares the GT-Power model predicted Brake Specific Fuel Consumption (BSFC) to the experimental values. Figure 2.7(a) shows the experimental and the predicted BSFC for 1500 rpm and 2000 rpm engine speeds and from low load to high load. The bottom plot presents the relative model error. Figure 2.7(b) compares the GT-Power predicted BSFC reduction for different values of cEGR concentrations to the experiments for 2 operating points, 9 bar BMEP 1500 rpm and 11 bar BMEP 2000 rpm. The BSFC reduction is computed relative to the 0% cEGR point in each case. The spark

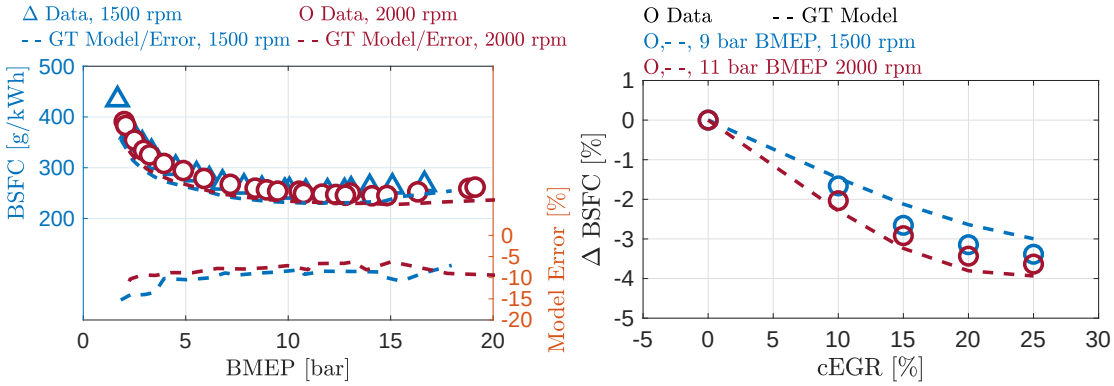

(a) BSFC without EGR

(b) BSFC improvement with EGR

Figure 2.7: The GT-Power predicted BSFC versus experimental values, (a) BSFC for the baseline turbocharged engine without cEGR for 1500 rpm and 2000 rpm engine speeds and a range of loads, along with the model error, (b) the percentage reduction in BSFC for different concentrations of cEGR at two operating points, 9 bar BMEP 1500 rpm and 11 bar BMEP 2000 rpm.

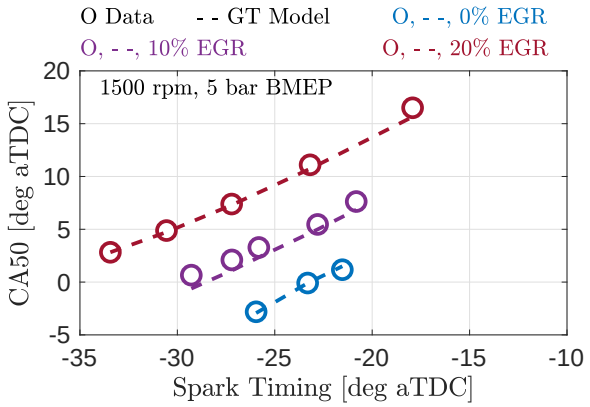

Figure 2.8: The GT-Power predicted CA50 for different spark timing and cEGR concentrations versus the experimental values for 5 bar BMEP 1500 rpm.

timing is selected for Maximum Brake Torque (MBT) subject to a knock constraint based on a 91 RON fuel [49, 51]. The GT-Power model slightly under-predicts the absolute BSFC value with a constant error of around 10%, while capturing the trends of BSFC variation with load and EGR well. This implies that the model can be used to study the relative benefit of different powertrains concepts. Finally, Figure 2.8 compares the model predicted CA50 to experimental values for 1500 rpm, 5 bar BMEP without cEGR and with 10% and 20% cEGR. The model captures the variation in the CA50 for different spark timing and cEGR concentrations accurately.

2.7 Vehicle Model

This section presents the vehicle and drivetrain model for a Ford Escape MY2015. Figure 2.9 shows the block diagram of the vehicle body and the drivetrain along with the exchanged signals between different component.

2.7.1 Vehicle Body Model

The vehicle longitudinal dynamics can be expressed as,

$$M_v \frac{d}{dt} v = F_t - F_b - F_l \tag{2.49}$$

$$M_v = m_v + \frac{I_w + I_g \gamma^2}{R_w^2} \tag{2.50}$$

where v is the vehicle speed, F_t is the tractive force, F_b is the braking force and F_l is the road load force, m_v is vehicle mass, I_w is the wheels inertia, I_g is the gear inertia, γ is the

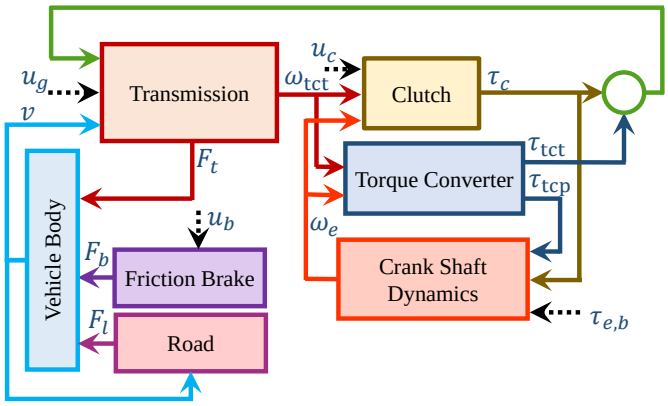

Figure 2.9: Vehicle and drivetrain model block diagram.

gear ratio, and R_w is the wheel radius. The road force is computed as,

$$F_l = C_{r,0} + C_{r,1}v + C_{r,2}v^2 \tag{2.51}$$

in which $C_{r,0}$, $C_{r,1}$ and $C_{r,2}$ are the chassis dynamometer correction factors from EPA reported values, shown in Table 2.2.

The braking force is described as,

$$\frac{1}{\theta_b}\dot{F}_b + F_b = K_b u_b \tag{2.52}$$

where u_b is the brake pedal position, K_b is a constant value and θ_b is a first order time constant, equal to 0.100 second used for simulating the brake dynamics.

2.7.2 Gearbox Model and Control

The gear box block computes the tractive torque transmitted to the wheels, τ_t, and the torque converter turbine speed, ω_{tct},

$$\tau_t = (\tau_{\text{cch}} + \tau_{\text{tct}})\gamma - \tau_{\text{loss}} \tag{2.53a}$$

$$\omega_{\text{tct}} = \omega_w \gamma \tag{2.53b}$$

Table 2.2: Vehicle parameters for MY2015 Ford Escape.

Vehicle Attribute	Value	Units
Test Weight	1758	kg
Tire Radius	431.8	mm
$C_{r,0}$	97.3	N
$C_{r,1}$	4.035	Ns/m
$C_{r,2}$	0.497	Ns^2/m^2

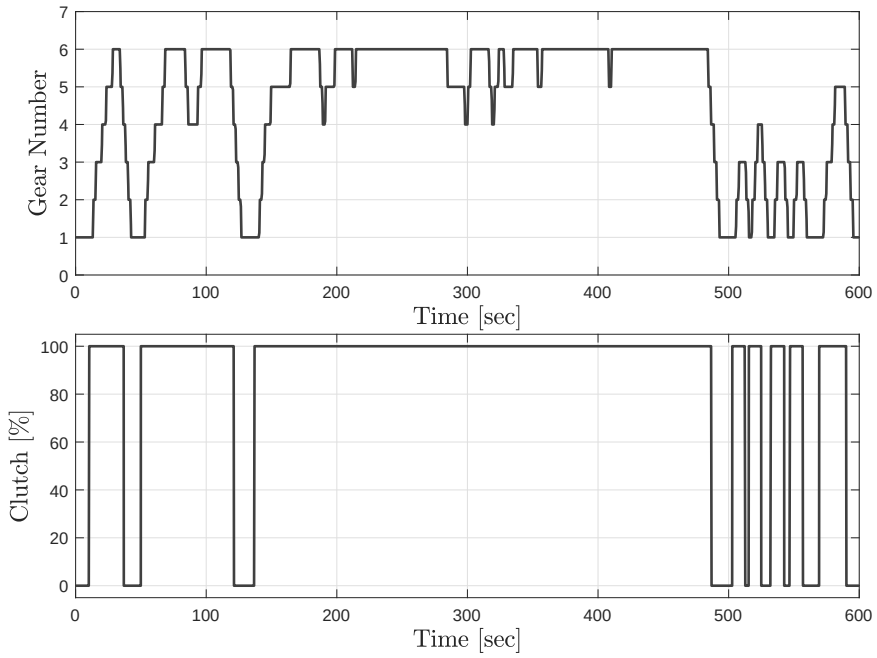

Figure 2.10: Gear shift, u_g, and clutch position, u_c, for the vehicle with PSS during the US06 drive cycle

in which τ_{tct} is the torque converter turbine torque, ω_w is the wheel rotational speed and τ_{loss} is the torque loss within the transmission, modeled as,

$$\tau_{\text{loss}} = \left(k_t|\tau_{\text{cch}} + \tau_{\text{tct}}|\right)^{\alpha_t} + \left(k_\omega \omega_{\text{tct}}\right)^{\alpha_\omega} \tag{2.54}$$

where, k_t, α_t, k_ω and α_ω are constant coefficients.

It is assumed that the shift duration is 0.5 second and the minimum time interval between two consecutive shifts is set to 2 seconds, unless the engine speed drops to less than 800 rpm. Figure 2.10 top subplot shows the gear number during the US06 drive cycle.

2.7.3 Torque Converter and Clutch Model

The torque converter block computes the turbine and pump torque based on the turbine to pump speed ratio, SR,

$$\text{SR} = \frac{\omega_{\text{tct}}}{\omega_{\text{tcp}}} \tag{2.55}$$

where, ω_{tcp} is the pump speed, which is also equal to the engine speed. The pump torque and the turbine torque are computed as follows,

$$\tau_{\text{tcp}} = \left(\frac{\omega_{\text{tcp}}}{K}\right)^2 \tag{2.56}$$

$$\tau_{\text{tct}} = \tau_{\text{tcp}} \times \text{TR} \tag{2.57}$$

where TR and K are the torque converter torque ratio and K-factor, defined as functions of speed ratio.

A tangent hyperbolic function is used for modeling the transmitted torque through the clutch, [52],

$$\tau_{\text{cch}} = u_c \tau_{\text{cap}} \tanh\left(\frac{\omega_{\text{tcp}} - \omega_{\text{tct}}}{C_c}\right) \tag{2.58}$$

where u_c is the clutch actuator position, which takes values of 1 and 0, τ_{cap} is the clutch torque capacity and C_c is a scaling factor for adjusting the clutch slip. The clutch is locked at all engine speeds larger that 1100 rpm and opens at engine speeds less than a 900 rpm. Figure 2.10 shows an example of the clutch performance during the US06 drive cycle.

2.8 Battery Model

The battery current, I_b, is computed using its terminal voltage, U_b, and the battery power, which is the sum of the motor power and the auxiliary power, P_{aux},

$$I_b = \frac{P_b}{U_b} \tag{2.59a}$$

$$P_b = P_m + P_{\text{aux}}. \tag{2.59b}$$

The battery terminal voltage is computed using a single resistance circuit model with R_b as the internal resistance and U_{oc} as the open circuit voltage,

$$U_b = \frac{1}{2}U_{\text{oc}} + \sqrt{\frac{U_{\text{oc}}^2}{4} - P_b R_b} \tag{2.60a}$$

$$U_{\text{oc}} = f(\zeta) \tag{2.60b}$$

in which ζ is the battery state of charge defined as the ratio of the battery charge to charge capacity, C_n. The battery state of charger dynamics are as follows,

$$\dot{\zeta} = -\frac{I_b}{3600 C_n}. \tag{2.61}$$

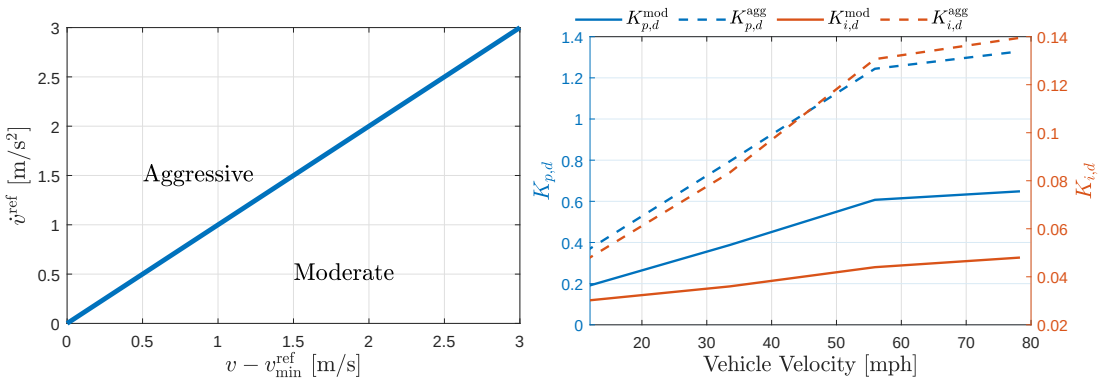

(a) (b)

Figure 2.11: Driver model, (a) driver gain selection logic, (b) driver gains.

2.9 Driver Model

The driver model introduced in [53] is used for tracking the drive cycle. The driver model is a switching gain PI controller,

$$u_d = K_{p,d}(v^{\text{ref}} - v) + \int K_{i,d}(v^{\text{ref}} - v) \tag{2.62a}$$

$$u_{\text{acc}} = \text{sat}(u_d)_0^{100} \tag{2.62b}$$

$$u_b = -\text{sat}(u_d)_{-100}^{0} \tag{2.62c}$$

in which u_{acc} is the acceleration pedal position, u_b is the brake pedal position, sat denotes saturation function, v^{ref} is the drive cycle reference speed and $K_{p,d}$ and $K_{i,d}$ are the driver proportional and integral gains, which switch values based on the relative vehicle speed compared to the drive cycle minimum permitted speed, $v^{\text{ref}}_{\text{min}}$ and the drive cycle 1 second ahead acceleration preview, $\dot{v}^{\text{ref}}$,

$$\dot{v}^{\text{ref}} = v^{\text{ref}}(t+1) - v^{\text{ref}}(t) \tag{2.63}$$

where t is in seconds. Figure 2.11(a) shows the criteria for changing the driver gains. When a fast acceleration is necessary or the vehicle speed is close to the minimum permitted speed the driver gains switch to aggressive gains, otherwise it uses moderate gains. Figure 2.11(b) show both aggressive and moderate proportional and integral gains scheduled all against the vehicle speed. All gains increase with the vehicle speed implying higher driver alertness at higher vehicle speeds.

CHAPTER III

Control of Hybrid Boosting in Highly Diluted Internal Combustion Engines

Boosting and downsizing guides the engine operating points into more efficient areas and thus improves the vehicle fuel consumption [54]. However, turbocharged downsized engines suffer from two main drawbacks. One is the drive-ability challenges associated with the engine turbolag and the other is the knock propensity at medium to high loads, which is often remedied by employing sub-optimal policies for spark and air fuel ratio. Consequently, the fuel efficiency of turbocharged engines diminishes at boosted points, which are not frequently visited in standard drive cycles, but depending on the driving style can increase the vehicle off-cycle fuel consumption.

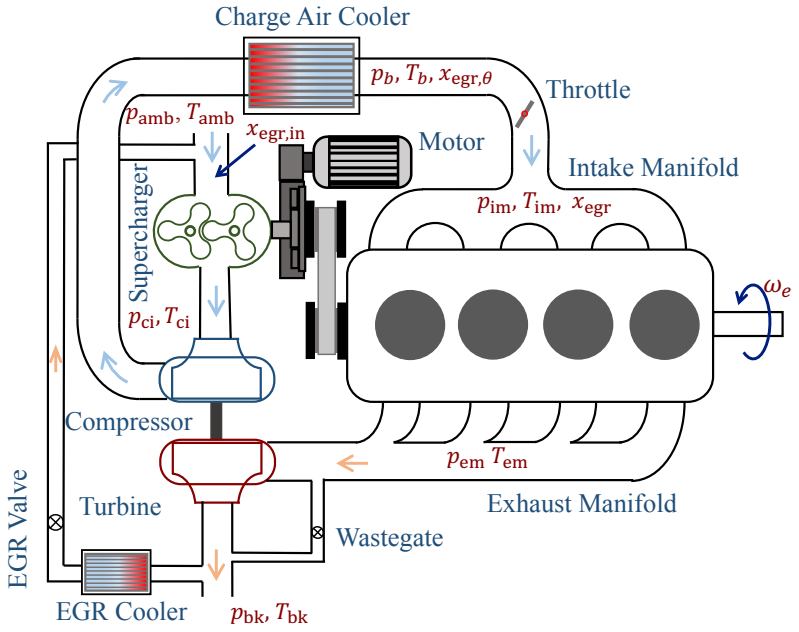

Figure 3.1: Schematic view of twincharged 4 cylinder SIDI engine with EGR loop and power split supercharger

In this chapter flexible boosting, enabled by the power split supercharger (also called hybrid supercharger), with high externally diluted combustion is proposed to address both of the aforementioned issues and to push the limits of downsizing and boosting further. The planetary gear set and the motor decouple the supercharger boost from the engine speed, creating a high bandwidth high stroke boost actuator similar to electric boosting systems [11, 18]. This benefit comes at the expense of an extra fuel penalty compared to turbocharging method, which takes advantage of waste energy recovery but has a lower bandwidth. Hence the control design of such system is critical to the engine fuel consumption. In a twincharged engine, with both a turbocharger and a supercharger, the engine boost pressure regulation transforms into a Dual-Input/Single-Output (DISO) problem, which is atypical of DISO problems addressed in literature [55–57] since both actuators have large stroke. An effective controller can incorporate the benefits of both boosting methods to achieve fast engine torque response and high fuel efficiency.

Although engine air path hybridization can also be achieved through electrically assisting the turbocharger [7,58], the power split supercharger is only partially powered by the electric motor thus can maintain a near charge sustaining operation with sufficient control design. The performance of the hybrid boosting can be compared with the electric boosting in [18] shown for electric supercharging with the same motor and supercharger. In addition, this system can further increase the vehicle fuel economy through start/stop and regenerative braking. The electric motor can easily replace the vehicle alternator to charge the battery further lowering the overall system cost. This configuration can be used for comparison between the hybrid boosting and torque assist with the same motor, shown in this chapter. A comparison between electrically assisted turbocharging and torque assist is carried out in [7] for minimizing the vehicle acceleration time, showing higher capability of boosting strategy in maximizing the vehicle acceleration but with higher fuel consumption.

The main contribution of this chapter is the design of a decentralized controller for air path management of a turbocharged Spark Ignition (SI) engine equipped with a hybrid supercharger. This controller coordinates throttle, wastegate, motor torque and EGR valve in the nonlinear air path of the engine, to achieve fast and efficient engine operation. This work also quantifies the hybrid system benefits for both variable speed boosting and torque assist modes, and a controller for transition between these two modes is proposed.

This chapter is organized as follows. First the turbocharged SI engine BSFC improvement due to cEGR is quantified using dynamometer engine testing and the adverse influence of cEGR on the turbolag is shown. In section 3.3 the designed controllers for both the twincharged engine and the baseline turbocharged engine are formulated. In section 3.4 the controllers performance for a large torque tip-in at constant engine speed is shown and validated on a high fidelity GT-Power engine model. The controller performance during varying engine speed is shown by simulation over the US06 drive cycle. Finally, in section 3.5 the powertrain transient response upgrade through torque assist is quantified and compared

against hybrid boosting policy in terms of both response time and the consumed energy for a range of transients.

3.1 Engine Description

The baseline engine in this study is a 1.6 liter Ford EcoBoost engine introduced in the previous chapter, without LP-EGR loop. The modified engine employes a power split supercharger at the low pressure side of the turbocharger and an LP-EGR loop. Figure 3.1 shows a schematic view of the modified super-turbo twincharged engine. The mean value engine model, used for analysis here, is modified for the twincharged engine to include the PSS shaft dynamics and pressure dynamics inside the added air path volumes. Note that in this chapter, the term Power Split Supercharger (PSS) and the term Hybrid Supercharger (HSC) are used interchangeably.

3.2 Cooled EGR Influence on Steady State and Transient Operation of the Turbocharged Engine

3.2.1 Steady State Fuel Consumption Reduction

The cooled EGR effect on fuel consumption reduction of the studied engine was shown in [6] through GT-Power simulations. Here the cEGR benefit is quantified through experimental data. The engine fuel flow rate was measured for different cEGR levels, while the spark timing was swept to determine the MBT spark timing or the knock limited spark timing at measured operating condition. Figures 3.2(a) to 3.2(d) show the engine BSFC versus spark timing represented in degrees before Top Dead Center (deg bTDC) for 4 different engine conditions, selected based on the operating points visitation frequency of the studied engine during EPA standard drive cycles, detailed in [59]. In the presented plots in Figure 3.2 the blue diamond indicates the baseline engine BSFC and spark timing without cEGR. The violet line, red line, green line, and the gray line respectively show the BSFC variation versus spark timing for 10%, 15%, 20% and 25% of cEGR concentration. The MBT spark timing, if not knock limited, is the minimum of the BSFC plots. As the level of cEGR increases, the minimum of BSFC-spark timing plots decreases and a more advanced spark timing is necessary for MBT combustion phasing. Table 3.1 summarizes the BSFC improvement for the four represented operating conditions in Figures 3.2(a) to 3.2(d).

A more complete picture on fuel consumption reduction for different cEGR concentrations is given in Figures 3.3(a), 3.3(b), and 3.3(c), which show the experimental BSFC increase for a range of engine operating points with 10%, 15% and 20% cEGR, respectively. With 10% cooled EGR, the fuel consumption decreases by 1.5%-3.0% for the majority of the operating points, 15% cooled EGR reduces the fuel consumption by 2.5%-3.5% and 20% cEGR decreases the fuel consumption by 3.0%-4.0% over most operating points. These results show that for cEGR concentrations up to 20% around 1.0% improvement in engine

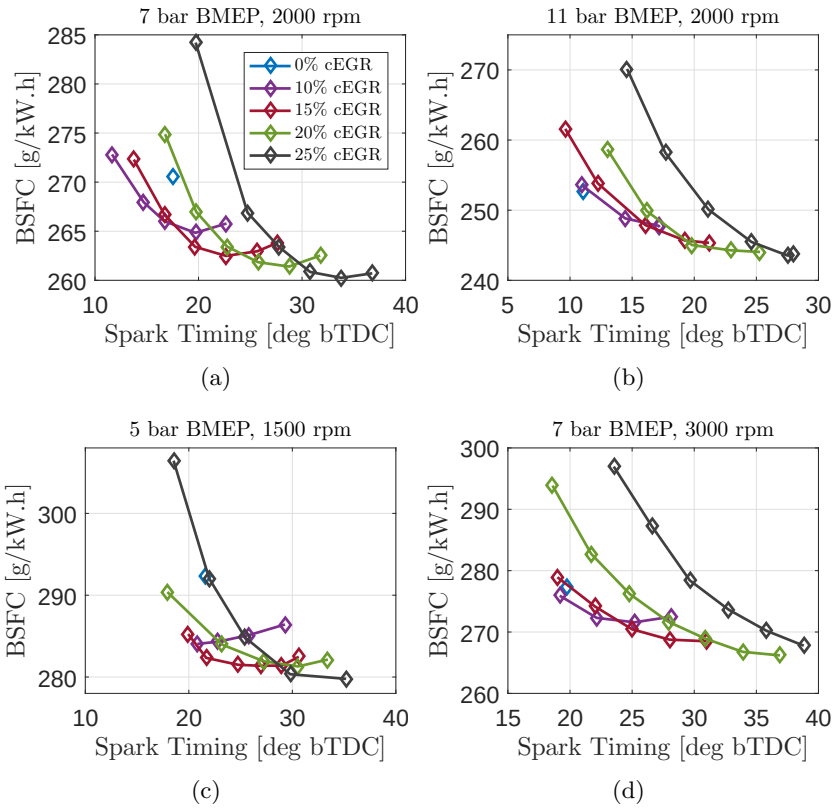

Figure 3.2: Spark sweep experimental results for different cEGR level, (a) 7 bar BMEP, 2000 rpm engine speed, (b) 11 bar BMEP, 2000 rpm engine speed, (c) 5 bar BMEP, 1500 rpm engine speed, (d) 7 bar BMEP, 3000 rpm engine speed.

BSFC is achieved for every 5% of included cEGR but increasing the EGR level beyond 20% results in a smaller BSFC improvement, probably due to combustion efficiency deterioration.

3.2.2 Transient Response Deterioration with Cooled EGR

Figure 3.4 shows the influence of cooled EGR on the transient response of the engine, using MVM simulations. The shown transient is a torque tip-in from 15% → 95% of full load at 2000 rpm constant engine speed. Figure 3.4(a) shows the BMEP response. The 0 to 90% response time of the engine increases from 1.5 seconds to 2.3 seconds with 20% cEGR

Table 3.1: Measured BSFC reduction for various points in Figures 3.2(a) to 3.2(d).

Engine BMEP [bar]	Speed [rpm]	10% cEGR	15% cEGR	20% cEGR	25% cEGR
7	2000	2.2%	3.1%	3.5%	3.9%
11	2000	2.0%	2.9%	3.4%	3.6%
5	1500	2.8%	3.7%	3.8%	4.5%
7	3000	2.1%	3.2%	4.0%	–

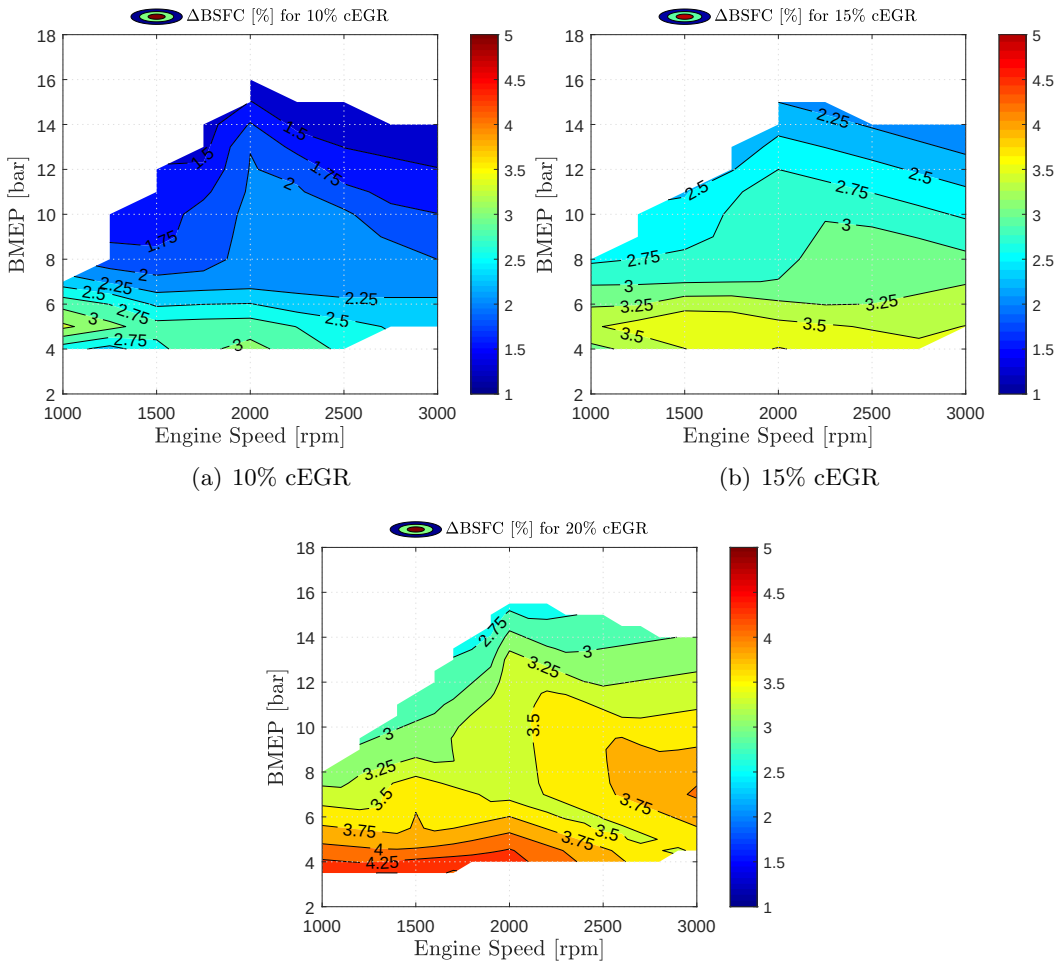

(a) 10% cEGR

(b) 15% cEGR

(c) 20% cEGR

Figure 3.3: Engine steady state fuel consumption improvement with, (a) 10% cooled EGR included, (b) 15% cooled EGR included, (c) 20% cooled EGR included.

included [6]. The main reason for the slower engine response and larger turbolag with cEGR is that higher intake manifold pressure, shown in Figure 3.4(b), and hence higher boost pressure is required for producing the same amount of torque due to partial pressure of burnt gases in the engine inlet air path when cEGR is present. Therefore, for a specific load tip-in with cEGR, the target boost pressure should be higher, meaning that the turbocharger should speed up to a higher value to provide the required boost pressure. In other words, for a specific transient in terms of the turbocharger speed and boost pressure the engine goes through a longer transient when cEGR is used compared to the same torque transient without cEGR. Other parameters such as reduced exhaust gases specific enthalpy due to lower exhaust temperature with cEGR and the bigger air path volumes also contribute to the increased response time. So although including cEGR decreases the engine fuel consumption, it slows the engine air path response to a torque demand, which can adversely impact the

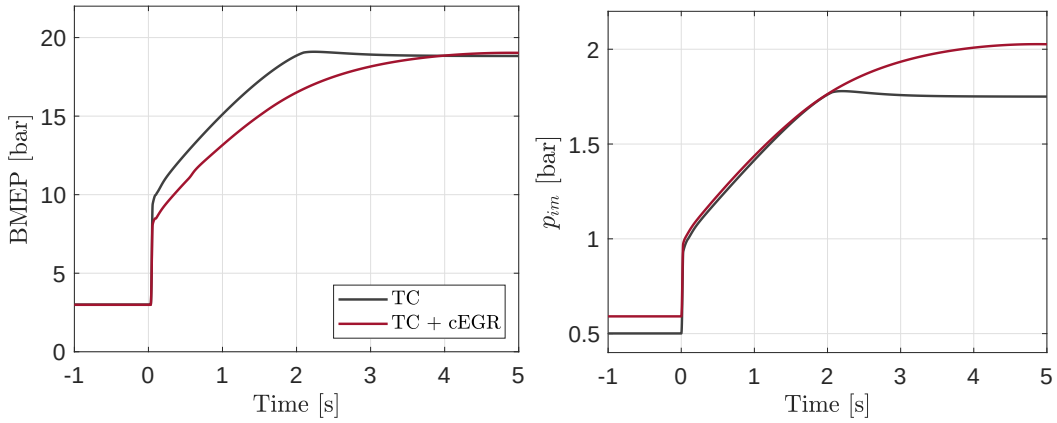

(a) BMEP (b) Intake manifold pressure

Figure 3.4: Turbocharged engine turbolag deterioration with cooled EGR, (a) BMEP response with 20% cEGR, (b) intake manifold pressure response with 20% cEGR.

vehicle drive-ability and even the tracking performance of the vehicle in an aggressive driving profile and hence its fuel economy if not compensated [60].

In this work hybrid power split supercharging, which produces flexible boost pressure control, is pursued for mitigating the enlarged engine turbolag with cEGR. The success of such solution depends of the effective coordination of all engine air path actuators, which is presented in the next section along with the closed loop control design for the baseline turbocharged engine used to achieve the results shown in Figure 3.4.

3.3 Closed Loop Control Design

3.3.1 Twincharged Engine Controller

The intake manifold pressure and its EGR concentration are the critical variables dictating the flow and composition into the cylinders. Moreover, the pre-throttle (boost) pressure is associated with fast manifold filling and consequently the engine transient response. Hence, the boost pressure is also selected as a control variable within the decentralized controller of the twincharged engine air path shown in Figure 3.5. The four actuators for controlling these three variables are the throttle valve, wastegate, the supercharger manipulated by the motor, and the EGR valve. The throttle valve is used for controlling the intake manifold pressure, EGR valve is employed for regulating the EGR concentration and wastegate and motor are coordinated for boost pressure tracking. The desired intake manifold pressure, p^d_{im}, is scheduled against the acceleration pedal position, u_{acc}, engine speed and the desired EGR concentration, x^d_{egr},

$$p^d_{\text{im}} = f(u_{\text{acc}}, \omega_e, x^d_{\text{egr}}). \tag{3.1}$$

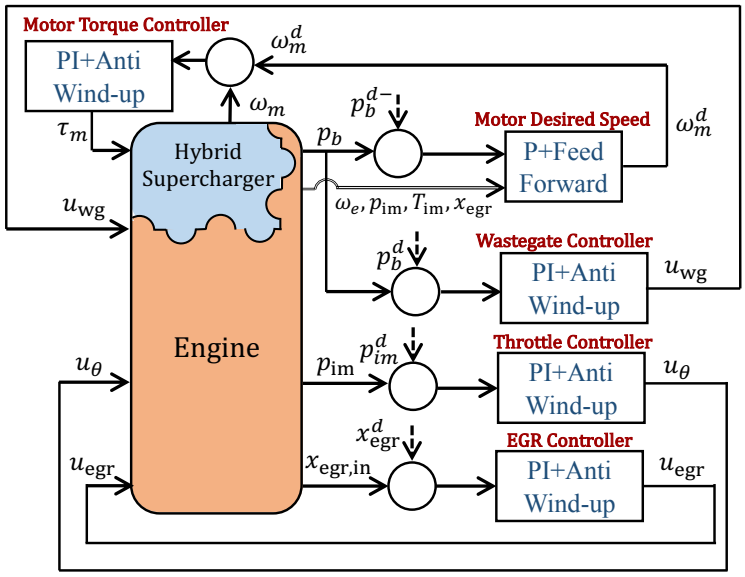

Figure 3.5: Air path actuators controllers with hybrid supercharger (PSS) in the boosting mode.

The desired boost pressure, p_b^d, is selected as 0.1 bar larger than the desired intake manifold pressure for boosted points and 0.1 bar larger than ambient pressure, p_{amb}, for non-boosted points to keep a small boost reserve across the throttle valve leading to faster manifold filling,

$$p_b^d = 0.1 + \max(p_{\text{amb}}, p_{\text{im}}^d). \tag{3.2}$$

In the following parts first the boost pressure coordination method is explained followed by the intake manifold pressure controller and EGR controller.

3.3.1.1 Boost Pressure Control

The wastegate and motor are used for controlling the engine boost pressure. A number of methods are proposed for designing DISO control systems [55–57]. Master-slave strategy is one of the most popular control methods suggested for DISO systems. This approach relies on one high bandwidth low stroke actuator (fine actuator) and a second low bandwidth high stroke actuator (coarse actuator). The fine actuator controller is often a proportional controller while the course actuator controller does integral action and tracks the steady state value [57].

The pressure ratio across the supercharger is governed by its speed, ω_{sc}, which can be controlled by the motor, ω_m. Therefore the motor controller commands the desired motor speed within the master-slave boost controller in Figure 3.5. The wastegate is used for steady state tracking and the supercharger as a transient response enabler. Although the

supercharger is mechanically coupled to the crankshaft, its speed is decoupled from the engine speed through the planetary gear set and the motor, hence it has similar response time as electric superchargers. The open loop bandwidth of the motor and wastegate are however governed by the manifold filing dynamics involved. In the particular setup studied, for a unit step in boost pressure at wide open throttle and 2000 rpm engine speed bandwidths are 0.65 Hz and 0.5 Hz, respectively for motor and wastegate. With the current air path plumbing the supercharger has to fill a larger volume, almost twice that of the compressor, due to the volume of connecting pipes between TC and the supercharger. Despite their similar bandwidth, the supercharger has a larger DC gain than the wastegate, capable of producing a boost pressure of more than 3 bar compared to 2 bar for the TC. This high DC gain allows achieving fast boost pressure control with the supercharger, but there is a higher fuel penalty associated with its operation because the supercharger uses crank and electric power to boost the engine, while the turbocharger takes advantage of waste energy recovery from the exhaust gas. So it is possible to generate a fast boost response with the supercharger but for the fuel economy sake it is desired to uses it less, similar to a fine actuator.

A proportional plus feed forward controller is used for commanding the motor speed, $\omega_{m,b}$, and a Proportional plus Integral (PI) controller with anti-windup loop is used for the wastegate effective diameter command, u_{wg}, as follows

$$\omega_{m,b} = \omega_{\mathrm{m}}^{\mathrm{ff}} + K_{\mathrm{em}}(p_b - p_b^{d-}) \tag{3.3a}$$

$$u_{\mathrm{wg}} = K_{p,\mathrm{wg}}(p_b - p_b^d) + \int K_{i,\mathrm{wg}}(p_b - p_b^d + K_{b,\mathrm{wg}}(u_{\mathrm{wg}} - \tilde{u}_{\mathrm{wg}}))dt \tag{3.3b}$$

where K_{em} is the motor controller proportional gain, $\tilde{u}_{\mathrm{wg}}$ is the non-saturated wastegate control command, $K_{p,\mathrm{wg}}$, $K_{i,\mathrm{wg}}$ and $K_{b,\mathrm{wg}}$ are respectively the proportional, integral and back-calculation anti-windup gain of the wastegate controller. The error signal in (3.3a) is computed based on the minimum required boost pressure, $p_b^{d-} = p_{\mathrm{im}}^d$, instead of the p_b^d, which is 0.1 bar higher than the p_{im}^d at the boosted points. This selection of the error signal enables the high stroke supercharger to operate as a low stroke actuator and bypass in steady state, and enables using the supercharger even less and saving fuel. Table 3.2 lists the controller gains.

The motor speed feedforward command, ω_m^{ff}, is the speed that produces a pressure ratio of unity across the supercharger. This speed is calculated from the engine breathing model, the supercharger map and the engine speed per (2.46c), which indicates that the engine speed is a measured disturbance on the hybrid supercharger, therefore including ω_e in the feedforward command reduces the calibration effort,

$$\omega_{\mathrm{m}}^{\mathrm{ff}} = \omega_{\mathrm{m}}^{\mathrm{ff}}(\omega_e, p_{\mathrm{im}}, x_{\mathrm{egr}}, T_{\mathrm{im}}). \tag{3.4}$$

Note that the twincharged engine air path regulation problem can be realized as a 3 input 3 output problem, in which the supercharger speed, throttle valve position and wastegate effective diameter are three system inputs and intake manifold pressure, boost pressure and compressor inlet pressure are the system outputs. Multivariable control approaches (MIMO) can be pursued for control design, but the MIMO controller performance would require different linearization for various load steps, thus the calibration effort of the MIMO controller is not trivial compared to an easily implementable decentralized controller structured based on the system dynamics and actuator priorities assigned. Later section shows that the fixed gain controller performs adequately in simulating a full drive cycle.

The low level motor controller receives torque command, thus a PI controller with saturation and anti-windup structure is designed to command the motor torque,

$$\tau_m = \min\Big(\max\big(\tilde{\tau}_m, \tau^{\min}(\omega_m)\big), \tau^{\max}(\omega_m)\Big) \tag{3.5a}$$

$$\tilde{\tau}_m = \int K_{i,m}(\omega_m^d - \omega_m + K_{b,m}(\tau_m - \tilde{\tau}_m))dt + K_{p,m}(\omega_m^d - \omega_m) \tag{3.5b}$$

where $\tau^{\max}(\omega_m)$ and $\tau^{\min}(\omega_m)$ are the maximum and minimum motor torque limits as functions of the motor speed, $K_{i,m}$ and $K_{p,m}$ are respectively the integral and the proportional gains of the controller and $K_{b,m}$ is the anti-windup gain. The desired motor speed, ω_m^d depends on the hybrid supercharger (PSS) mode. During the boosting mode $\omega_m^d = \omega_{m,b}$ from (3.3a).

The hybrid supercharger has to coordinate the brake and bypass valve with the motor torque to switch between different operating modes. Figure 3.6 shows the finite state machine designed for starting the hybrid supercharger, using it for boosting and braking it at the end of transient. During the steady state operation, the supercharger is stopped and bypassed. The motor speed when the supercharger is stopped is $\omega_{m,0}$ from (2.45a). Only when a large transient is commanded, which is specified as the desired intake manifold pressure to be 0.1 bar higher than the boost pressure the hybrid supercharger is used. To do so, the brake is released so that the supercharger gets powered by the motor. The motor speed decreases as it gradually loaded to speed up the supercharger. The bypass valve should remain open at this stage because, if the supercharger speed is not high enough, it will act as a restriction to the flow. When the motor speed reaches its feedforward speed the bypass valve closes and the supercharger is ready to control the engine boost pressure. When the desired intake manifold pressure is achieved and the supercharger pressure ratio drops to unity, the bypass opens, the motor brakes the supercharger and the brake locks the sun gear. Note that during a transient drive cycle when the supercharger is not boosting the engine, the motor can be used for regenerative braking or start/stop, similar to a regular parallel hybrid powertrain, hence the supercharger is locked at its default position. Please see [33] for more information on using the the PSS as a hybrid powertrain.

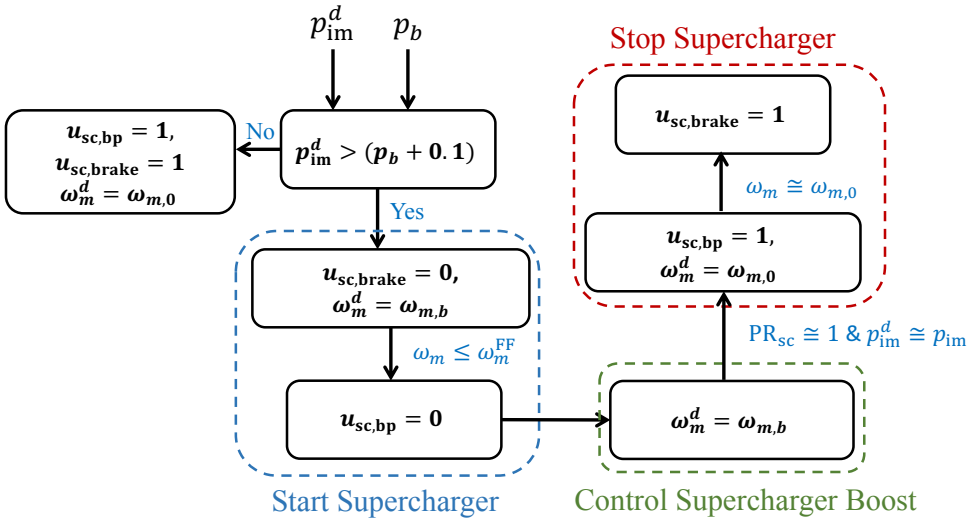

Figure 3.6: Finite state machine for hybrid supercharger (PSS) mode change.

Table 3.2: Twincharged engine closed loop controllers gains

Controller	K_P	K_I	K_b
Throttle	200	400	3
Wastegate	30	50	5
Motor Speed	14000	-	-
Motor Torque	0.02	0.03	1.5

3.3.1.2 Intake Manifold Pressure Control

The intake manifold pressure is highly coupled to the throttle valve movement, hence the throttle valve is used to track the intake manifold pressure to its desired value with a PI and anti-windup controller,

$$u_\theta = K_{p,\theta}(p^d_{\text{im}} - p_{\text{im}}) + \int K_{i,\theta}(p^d_{\text{im}} - p_{\text{im}} + K_{b,\theta}(u_\theta - \tilde{u}_\theta))dt \tag{3.6}$$

where u_θ and $\tilde{u}_\theta$ are the saturated and non-saturated throttle commanded angle, $K_{p,\theta}$, $K_{i,\theta}$ and $K_{b,\theta}$ are respectively proportional, integral and anti-windup gains listed in Table 3.2.

3.3.1.3 EGR Control

Although fixed cEGR concentration in the intake manifold is desired during a transient response, a controller that manages the large transport delay between the EGR loop and the EGR concentration into the intake manifold requires a significant effort [61]. To simplify the task and allow the hybrid supercharger evaluation, the EGR concentration is regulated at the air path inlet (the supercharger upstream) using a decentralized PI controller with anti-windup. The EGR concentration at the air path inlet, $x_{\text{egr,in}}$, is computed by measuring

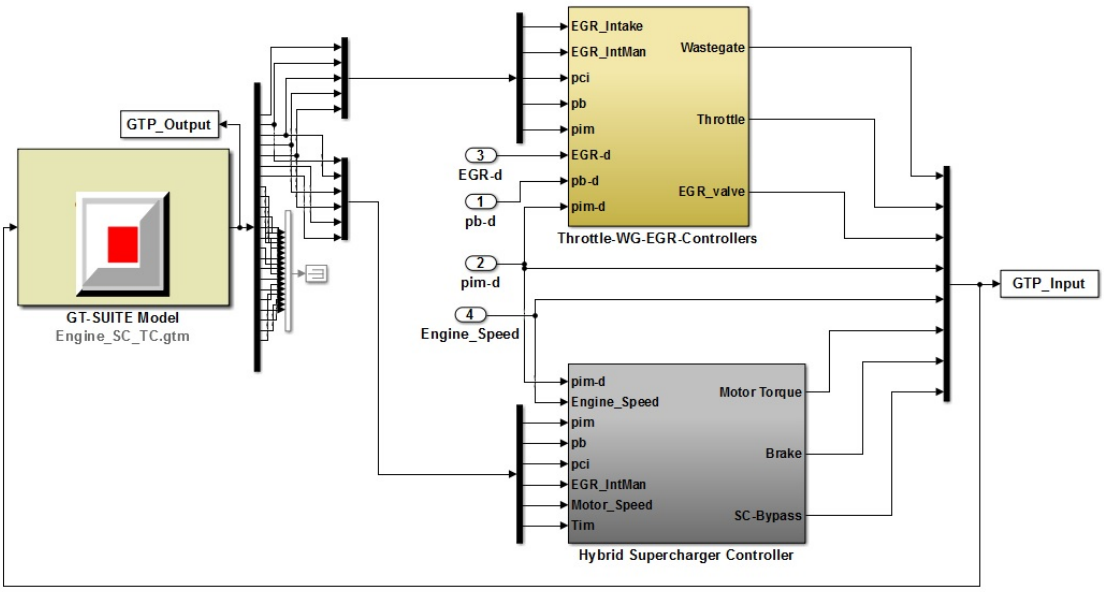

Figure 3.7: Controllers in loop with GT-Power engine model.

the air flow and calculating the EGR flow through the EGR valve using the filtered pressure differential across the EGR orifice [62],

$$u_{\text{egr}} = K_{p,\text{egr}}(x^d_{\text{egr}} - x_{\text{egr,in}}) + \int K_{i,\text{egr}}(x^d_{\text{egr}} - x_{\text{egr,in}} + K_{b,\text{egr}}(u_{\text{egr}} - \tilde{u}_{\text{egr}}))dt \tag{3.7}$$

in which u_{egr} is the EGR valve commanded effective diameter, $\tilde{u}_{\text{egr}}$ is the non-saturated control signal, x^d_{egr} is the desired EGR concentration, $K_{p,\text{egr}}$, $K_{i,\text{egr}}$ and $K_{b,\text{egr}}$ respectively stand for the proportional, integral and anti-windup gains of the controller. The desired EGR concentration is selected equal to 0.2 ($x^d_{\text{egr}} = 0.2$) for the cases with EGR, chosen based on the fuel economy improvement results shown in section 3.2.1.

3.3.2 Baseline Engine Controller

The baseline engine air path control problem, which is without the hybrid supercharger and EGR loop, reduces to a throttle-wastegate coordination for intake manifold and boost pressure control. Different control approaches are introduced in literature, including multi-variable [63], nonlinear [64] and PID [65] controllers. A decentralized controller is designed for fast throttle and wastegate coordination, in which the throttle valve controls the intake manifold pressure and the wastegate is used to control the engine boost pressure. The throttle valve command is computed from (3.6) and the wastegate command from (3.3b). The desired boost pressure is selected according to (3.2).

Sequential loop closing method was used to tune the designed controller, in which first

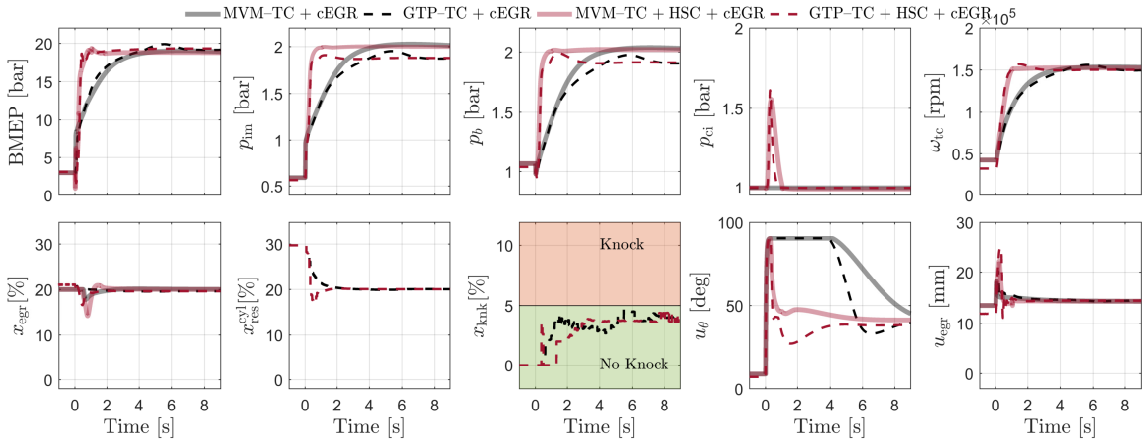

Figure 3.8: Comparison of the engine response during a large load tip-in (15→95% of full load) at 2000 rpm constant engine speed.

the throttle loop, which naturally has a larger bandwidth, is closed and then the wastegate loop is adjusted to acquire the desired boost pressure response. The controller gains of the baseline turbocharged engine are selected such that the bandwidth of the throttle loop is around 0.6 Hz and the bandwidth of the wastegate loop is around 0.1 Hz for the majority of operating points based on the linear analysis. The baseline production engine is not equipped with EGR loop, however, this work also addresses the EGR influence on the baseline turbocharged engine. To avoid misunderstanding, referring to the baseline means that no EGR is used but when EGR is included it is referred to as turbocharged engine with EGR.

3.4 Controller Validation and Closed Loop Simulation Results

3.4.1 Constant Speed Torque Tip-ins

This section shows the designed controller closed loop performance and its validation on a high fidelity GT-Power engine model for a constant speed torque tip-in. The GT-Power model uses a semi-predictive Wiebe function combustion model derived from the literature [50] and captures the 1-D manifold gas dynamics, valve lift and port flow behavior, heat transfer, turbocharger and supercharger dynamics, knock onset and other details necessary to predict engine performance. The model validation was shown in the previous chapter. Figure 3.7 shows the GT-Power engine model coupled to a MATLAB Simulink model that includes the designed air path controllers in the previous section. The GT-Power signals are filtered using a moving average filter and sampled at 200 Hz rate for use in the controllers.

Figure 3.8 compares the MVM transient response for twincharged and turbocharged engines (red and black solid lines respectively) to the GT-Power model response (dashed lines) with controllers of Table 3.2. For all shown cases 20% cEGR is included. The studied

transient is a 3 to 19 bar BMEP tip-in, corresponding to 15→95% load change, at 2000 rpm constant engine speed. The designed controllers have satisfactory performance on both MVM and the high fidelity model. The top left plot shows the BMEP response, in which the engine BMEP is calculated based on the crank output torque and zero auxiliary loads ($\tau_{\text{aux}} = 0$), hence the load from the planetary gear set partially powering the supercharger is included in the shown response. The 0 to 90% response time of the engine with 20% cEGR from MVM simulation is upgraded to 0.5 second with the hybrid supercharger and designed controllers, showing a significant improvement compared to the turbocharged engine with EGR, which has a 0 to 90% response time of 2.3 seconds. The crank output BMEP response is not smooth due to the torque interaction between the planetary gear set and the engine.

The top second, third and forth subplots show the intake manifold pressure, the boost pressure and the compressor inlet pressure, respectively. Both intake manifold pressure and boost pressure have faster transients with the hybrid supercharging system. The compressor inlet pressure, which is also the supercharger discharge pressure, is larger than unity only during the first second of the transient and it approaches unity when the transient is over, displaying the master-slave performance for the controller. There is a steady state offset between the MVM and GT-Power model within the required intake manifold pressure at 19 bar BMEP. The top right subplot shows the turbocharger speed during the studied transient. The turbocharger response is faster with hybrid supercharging system because the target torque is achieved faster and thus more energy is available to spin the turbocharger.

The bottom left subplot in Figure 3.8 shows the cEGR concentration inside the intake manifold during the transients. The x_{egr} in the intake manifold drops from 20% to 14% which could bring the engine closer to knock if spark is not adjusted. The next subplot shows the burned residuals fraction in cylinder 1 at combustion start, $x_{\text{res}}^{\text{cyl}}$, available from the GT-Power simulation. This plot shows that during the simulated transient $x_{\text{res}}^{\text{cyl}}$ does not exceed its value at low load, where it has stable operation, thus engine misfire is not expected. The third subplot shows the unburned mass fraction at knock onset, x_{knk}, for cylinder 1 from the GT-Power model. An Arrhenius auto-ignition delay integral [66] based on the ignition delay expression of Hoepke et al. [51] is used to predict the end gas auto ignition. The GT-Power model computes the unburned mass fraction when the auto-ignition delay integral reaches unity. The knock free operation is considered less than 5% unburned mass fraction at knock onset. As seen in this plot, the engine maintains knock free operation during the shown transients. The next two plots show the throttle and EGR valve command. The throttle valve is partially closed at low load, when the tip-in is applied it opens to allow more air flow into the cylinders, but it eventually closes to regulate the intake manifold pressure. The throttle valve remains open for a longer time interval for the turbocharged engine because the target intake manifold pressure is achieved slower. The wastegate valve remains fully closed throughout the shown transient for all the shown cases, thus not represented as a separate plot. The reason is that at both high and low load the desired boost pressure

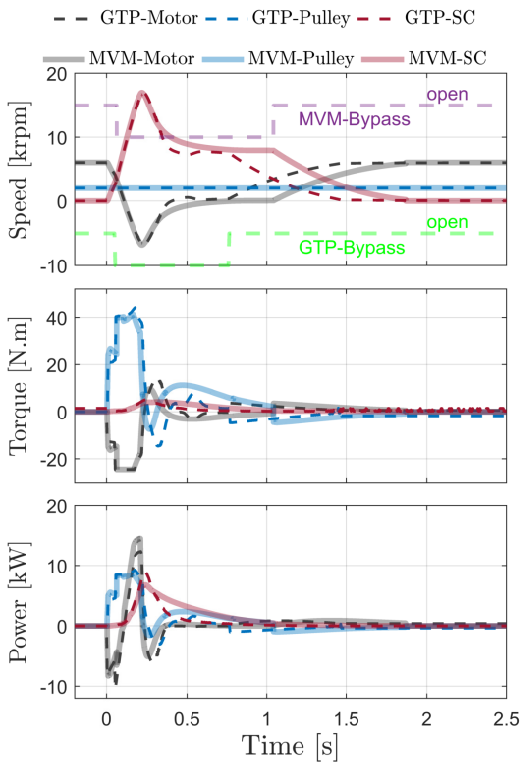

Figure 3.9: Planetary gear set nodes speed, torque and power during a large load tip-in (15→95% of full load) at 2000 rpm constant engine speed.

$(\max(p^d_{\text{im}}, p_{\text{amb}}) + 0.1$ bar) is not achieved.

Figure 3.9 shows the speed, torque and power for the motor, supercharger and the pulley during the studied transient. Before the transient the supercharger (red) is stopped ($\omega_{sc} = 0$). When the transient starts the supercharger brake opens and the motor speed (black) decreases to increase the supercharger speed and consequently its pressure ratio. Then the bypass valve closes and the motor speed is controlled to achieve the desired boost pressure. Finally, when the transient is complete and the supercharger pressure ratio drops to unity, the bypass opens and the motor speed increases to stop the supercharger. The bypass valve position is also displayed on the plot (dashed violet for MVM and dashed green for GT-Power), where high means open and low means closed. Note that the target intake manifold pressure is lower in the GT-Power simulation hence the supercharger is braked and bypassed earlier within the shown response, which causes the observed differences between the GT-Power simulation and MVM simulation after t=0.75 second.

The second subplot in Figure 3.9 represents the torques. In order to avoid imposing a large torque on the engine crank during the supercharger start phase, when the engine is producing a small torque, the motor torque controller switches gains and has less aggressive gains (equal to half of the motor torque controller gains for boosting mode, shown in Table

3.2). The effect of this gain switching strategy is evident in torque plots. At the start of the transient some motor torque is applied, but when the bypass valve closes, the motor torque increases (in magnitude) to the maximum permissible amount.

The motor, supercharger and pulley power are represented in the bottom plot. Note that the pulley ratio is unity in Figure 3.1. The motor power (black) is the motor electrical power, a positive sign means motoring and a negative sign stands for generating. The device switches between motoring and generating several times during the investigated transient. When the motor torque and speed have same signs the electric machine is working as a motor, while having opposite sign means generating. A positive pulley power (blue) means that the power direction is from the engine crank into the planetary gear system and a negative sign indicates the reverse direction. The supercharger power (red) is always positive because it is always a power consumer. Integrating the MVM supercharger consumed power, the supercharger required work, W_{sc}, to do the transient is 2.6 kJ, while the energy taken from the engine crank shaft, W_{pulley}, is 2.2 kJ and the electrical energy used by the motor, W_{motor}, is 1.0 kJ, which shows that most of the supercharger consumed power is from the crankshaft.

3.4.2 Hybrid Supercharger Performance on Drive Cycle

While the simulations presented in the previous section focused on constant engine speed torque tip-ins, this part briefly investigates the twincharged engine operation during a transient drive cycle using MVM. Figure 3.10(a) shows the speed profile of the US06 drive cycle, which is a part of the EPA standard test procedure for vehicle's fuel economy assessment. Two segments of the drive cycle are marked with red dashed squares and the engine operation during these two segments are shown in Figure 3.10(b) and Figure 3.10(c). Furthermore, the battery State of Charge (SoC) variation during the drive cycle is represented under the speed profile in Figure 3.10(a).

The modeled vehicle for this study is a Ford Escape MY2015 with 6 speed automatic transmission. The details of the vehicle, driveline, driver, and battery model were presented in the previous chapter. The battery capacity is considered 1.2 kWh based on the hybrid supercharger manufacturer recommendation. The SoC drops only around 0.7% at the end of cycle, because as seen in Figures 3.9, 3.10(b) and 3.10(c) the motor supplies only a small part of the power consumed by the supercharger. Although this result indicates a smaller battery can be used for the hybrid supercharger system, the battery sizing requires enabling all micro-hybrid functionalities of the hybrid system such as start/stop and regenerative braking and is left for future development.

Figure 3.10(b) shows the powertrain parameters during t = 50 – 53 seconds and Figure 3.10(c) shows the same parameters for t = 503 – 506 seconds. The top left subplots show the engine speed (gray) and the supercharger speed (red). The top right subplots represent the intake manifold pressure (gray) and the compressor inlet pressure (SC discharge, red)

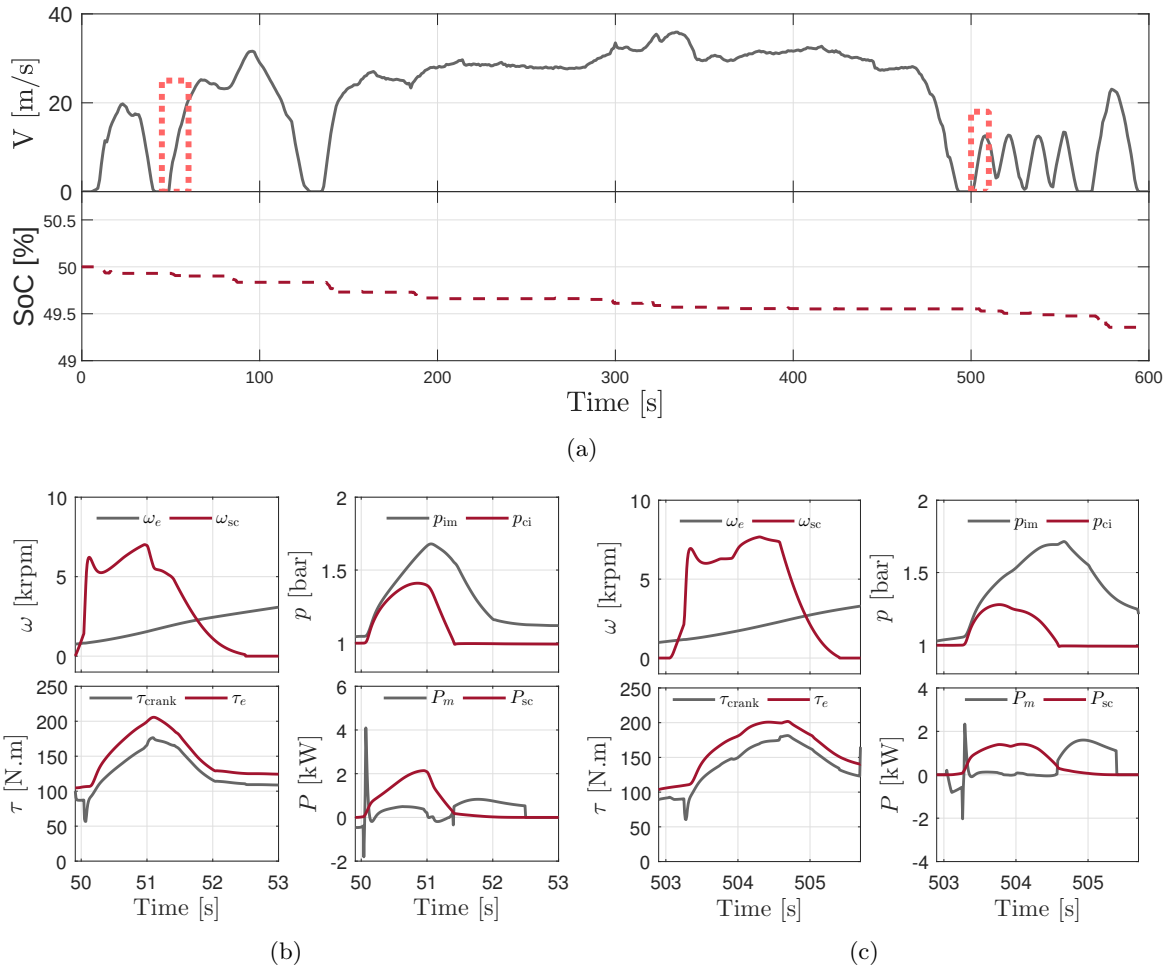

Figure 3.10: The hybrid supercharger performance during a transient drive cycle using MVM, (a) the US06 drive cycle speed profile and two selected transients, (b) the powertrain and hybrid supercharger parameters during t=50-53 seconds, (c) the powertrain and hybrid supercharger parameters during t=503-506 seconds.

during the shown time interval. The supercharger is braked and bypassed when not in use. The bottom left subplot shows the engine produced torque (red), τ_e, and the crankshaft torque delivered to the torque converter and friction clutch, τ_{crank}. The observed torque undershoot at the beginning of the vehicle acceleration is due to speeding up the supercharger. Although this abrupt drop could cause Noise, Vibration and Harness (NVH) issues, the torque undershoot is for a very short time interval, hence the energy taken from the crankshaft is small and the associated engine speed drop is less than 5 rpm. The last subplot shows the supercharger consumed power (red) and the motor power (gray). Similar to constant speed engine transients, the motor switches from generating to motoring when speeding up the supercharger, then the motor partially powers the supercharger and when boosting from the supercharger is not required anymore, it brakes the supercharger.

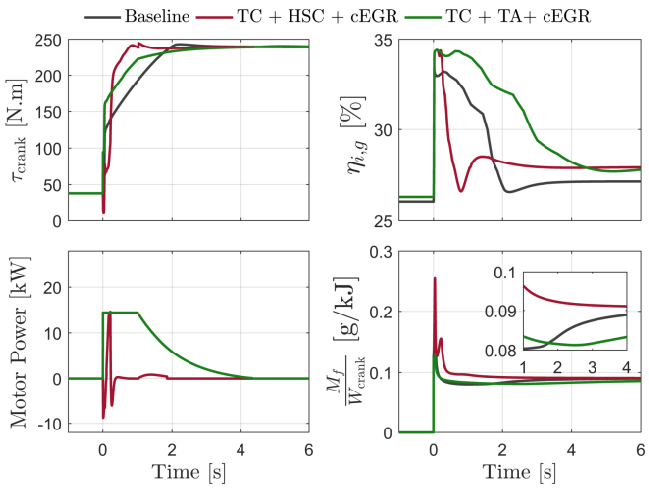

Figure 3.11: Engine transient response comparison for baseline, with hybrid supercharging and with torque assist for a large torque tip-in at 2000 rpm constant engine speed using MVM.

3.5 Hybrid Supercharging v.s. Torque Assist

The supercharger, motor and planetary gear set can improve the engine transient torque response in two ways, one is through variable speed supercharging and the other is through adding the motor torque directly into the engine crank, known as torque assist. In this section the engine transient response with 20% cEGR is compared for these two strategies. A gain scheduled proportional controller based on the error in the intake manifold pressure is designed for controlling the motor torque during a load tip-in for torque assist strategy in addition to throttle-wastegate coordination,

$$\tilde{\tau}_{\text{m}} = K_{\text{TA}}(p_{\text{im}}^{d} - p_{\text{im}}) \tag{3.8}$$

where K_{TA} is the proportional gain.

Figure 3.11 compares a 3 to 19 bar BMEP load tip-in at 2000 rpm constant engine speed with torque assist (TC + TA + cEGR, green) to a transient response with variable speed supercharging (TC + HSC + cEGR, red) both with 20% cEGR and the response of the baseline engine (gray) without cEGR. The top left plot shows the crank output torque response. The torque assist improves the crank torque response time to 1.0 seconds (compare to 0.5 seconds for hybrid supercharging, 1.5 seconds for baseline without cEGR and 2.3 seconds for turbocharged with 20% cEGR). Although the torque response is slower compared to variable speed supercharging, the crank output torque is smooth similar to the baseline engine response. The bottom left subplot compares the motor power for torque assist to motor power for hybrid boosting. The torque assist strategy requires 30.0 kJ energy from

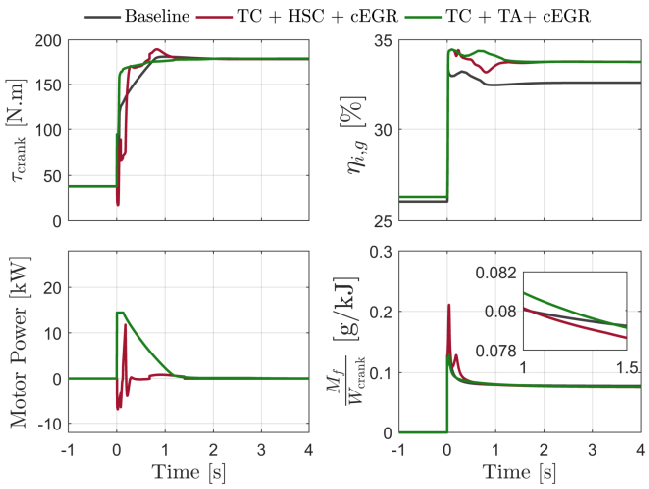

Figure 3.12: Engine transient response comparison for baseline, with hybrid supercharging and with torque assist for a moderate torque tip-in at 2000 rpm constant engine speed using MVM.

the battery to do this transient, which is 9 times larger than the total energy consumed to speed up the transient using variable speed supercharging.

Although the hybrid boosting strategy requires less power for speeding up the engine transient response to a torque demand, in terms of the total consumed fuel by the engine and motor the story could be different. The top right subplot in Figure 3.11 shows the engine gross indicated efficiency, $\eta_{i,g}$, for different strategies. $\eta_{i,g}$ is computed using the engine fuel flow rate (calculated from the fueling map of the engine) and gross power. The bottom right subplot shows the ratio of total fuel mass, M_f, to the work given to the engine crank shaft, W_{crank}, with integration started at $t = 0$. The total fuel flow rate is computed as the sum of the engine fuel flow rate and the fuel flow rate associated with the electric power assuming 30% efficiency for electric power production from fuel. A part of this plot is zoomed in to clarify some details. The red line lies above the green line for the shown time interval, meaning that the engine with hybrid boosting strategy consumes more fuel for the same work transferred to the crank shaft, confirming the result found in [7]. The reason lies in the shape of boosted engines efficiency map, an example of which can be found in [67]. Boosted engines have lower efficiency at highly boosted points due to the necessary suboptimal measures employed in these points, such as spark retardation and fuel enrichment employed for knock and over-temperature protection. As it is clear from the $\eta_{i,g}$ plot, with hybrid boosting strategy the engine operating points would immediately shift into high boost low efficiency region, hence resulting in a higher fuel consumption. Consequently, the operating points of the hybrid boosting case lie within the low efficiency region for a longer time compared to the torque assist case.

Based on this fact, the outcome should be different when the transient target load remains

within the high efficiency region of the engine map. Figure 3.12 shows such transient, which is a 3 to 14 bar BMEP transient at 2000 rpm engine speed. As clear from the torque response plot the torque assist strategy has faster response, and the engine efficiency is high after the transient. In this case, the ratio of total fuel mass to crank work is slightly lower for the hybrid boosting strategy, shown in the bottom right subplot, indicating that hybrid boosting has a lower fuel consumption for moderate load tip-ins. Note that the steady state efficiency of both supercharged and torque assist cases is higher than the baseline engine due to the involved cEGR.

Figure 3.13 compares the 0 to 90% response time of the baseline engine (Figure 3.13(a)) to turbocharged engine with 20% cEGR (TC + cEGR, Figure 3.13(b)) and the twincharged engine with 20% cEGR when the hybrid supercharger is enabled (TC + HSC + cEGR, Figure 3.13(c)) and when the supercharger is locked and bypassed and the torque assist mode is enabled (TC + TA + cEGR, Figure 3.13(d)). The simulated transients are constant speed torque tip-ins starting from 3 bar BMEP. The horizontal axis shows the engine speed and the vertical axis represents the transient target BMEP. The controllers are gain scheduled for producing the results of Figure 3.13. An example of transients in Figures 3.13(a) and 3.13(b) were shown in Figure 3.4 and examples of transients in Figures 3.13(c) and 3.13(d) were shown in Figures 3.8, 3.11, and 3.12.

While Figure 3.13(b) confirms that cooled EGR slows down the turbocharged engine air path dynamics for medium to large torque transients, the results presented in Figure 3.13(c) and Figure 3.13(d) substantiate that both hybrid supercharging and torque assist are capable of eliminating or mitigating the enlarged engine turbolag associated with cEGR. The results show that the hybrid supercharging strategy can reduce the engine response time for the entire range of investigated transients to less than 0.5 second while the torque assist strategy performance is limited to small torque increase requests. Note that the limitations depend on the motor maximum torque thus proportional to electric machine cost.

Figure 3.14(a) shows the total energy consumed ($W_{\text{motor}} + W_{\text{pulley}}$) for transients of Figure 3.13(c) and Figure 3.14(b) represents the required electrical energy corresponding to transients in Figure 3.13(d). As seen the total required work is significantly lower for the supercharging strategy. The work spent for speeding up the transients can be recovered from the cEGR benefits. It will be interesting to know how long the engine should work at high load to recover the electric energy consumed for speeding up the transient from the cEGR fuel economy benefits. This waiting time, τ_{wait}, for 1% improvement in the engine BSFC is computed and the result is shown in Figure 3.15(a) and Figure 3.15(b) for supercharging and torque assist strategies respectively. For example, for the sample transient in Figure 3.8, which requires 1.0 kJ energy from the battery, 2.4 seconds wait time at high load after doing the tip-in is required to recover the consumed electric power for 1% improvement in the engine BSFC, and if the engine BSFC improvement is 4%, due to 20% of cEGR, this wait time will be 0.6 seconds, while the corresponding number for torque assist strategy is

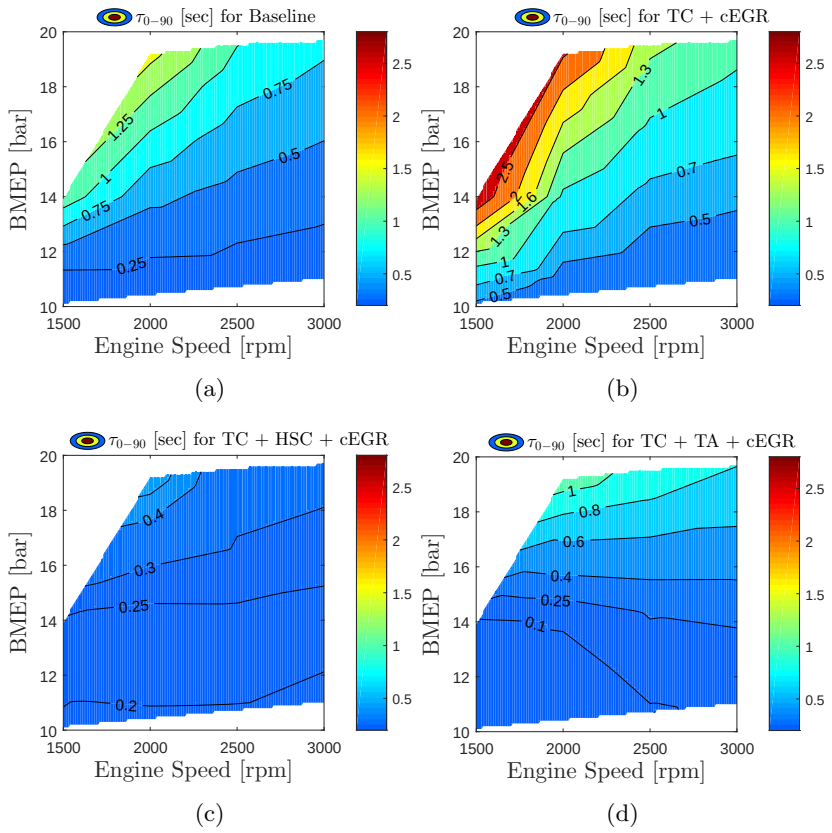

Figure 3.13: The engine 0 to 90% response time for a constant speed load tip-in starting from 3 bar BMEP, (a) response time of baseline engine without cEGR, (b) response time with 20% cEGR, (c) response time with hybrid supercharging, (d) response time with torque assist.

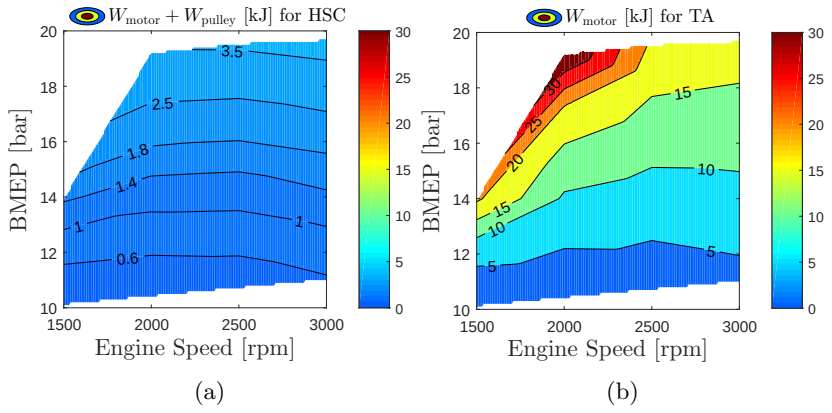

Figure 3.14: Consumed energy for speeding up the constant speed load tip-ins shown in Figures 3.13(c) and 3.13(d), (a) total consumed energy for hybrid supercharging, (b) consumed energy for torque assist.

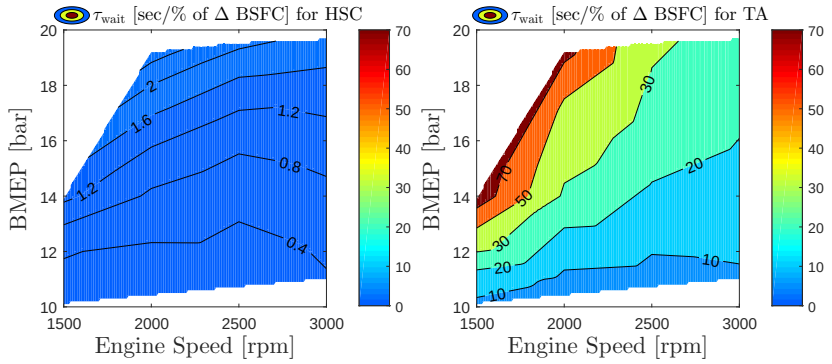

(a) (b)

Figure 3.15: Wait time at high load after the tip-in to recover the consumed electric energy during transient from cEGR benefits per percent of BSFC improvement, (a) wait time if using hybrid supercharging strategy, (b) wait time if using torque assist.

20 seconds from Figure 3.15(b).

In summary, in the case of limited available energy, hybrid boosting is more effective for engine transient response enhancement, whereas in terms of fuel consumption depending on the transient either of the strategies might be fuel economic. Indeed, in a vehicle the fuel optimal strategy also depends on the electric energy generation efficiency and the duration of the transient, thus a full drive cycle simulation is needed to determine the fuel efficient strategy for each vehicle acceleration and electric boosting should not be simply excluded from tip-ins as in [68].

3.6 Summary

This chapter presented a decentralized controller for a twincharged engine air path control problem with a power split supercharger and cooled EGR. The proposed controller uses a master-slave structure to control the engine boost pressure. In this controller the high stroke supercharger is slaved to the turbocharger, so that the supercharger is used during transients and the turbocharger tracks the steady state boost pressure. This structure minimizes the supercharger usage and improves the vehicle fuel economy since there is a higher fuel penalty for the supercharger operation compared to the turbocharger. The designed controller was validated against a high fidelity GT-Power engine model and the performance of the controller during both constant and varying engine speed transients was shown. It was shown that the power split supercharger with the designed controller is capable of reducing the engine response time to less than 0.5 second for a range of transients.

This chapter also studied the torque assist strategy, with the PSS motor, for transient response improvement of the turbocharged engine. The mean value simulation results indicate that although both supercharging and torque assist strategies are capable of improving the

engine torque response time, the supercharging strategy is more effective and requires less energy specially for large transients, for which the torque assist capability could be restricted by the energy available in the battery and hence has more restricted opportunities in an aggressive drive cycle. However, in terms of the fuel efficiency depending on the transient and the electric energy availability either of the strategies can be fuel optimal.

CHAPTER IV

Optimal Energy Management for a Mild Hybrid Vehicle with Electric and Hybrid Engine Boosting Systems

Hybridization is one of the promising solutions for the ever-tightening fuel economy regulations. The resulting flexibility, from dual energy source of a hybrid electric vehicle permits using the engine more efficiently and saving fuel. A mild hybrid powertrain, typically realized with a low voltage system (48 V) requires a small battery pack and low-power electric machines. The motor in a mild hybrid system is not capable of propelling the vehicle

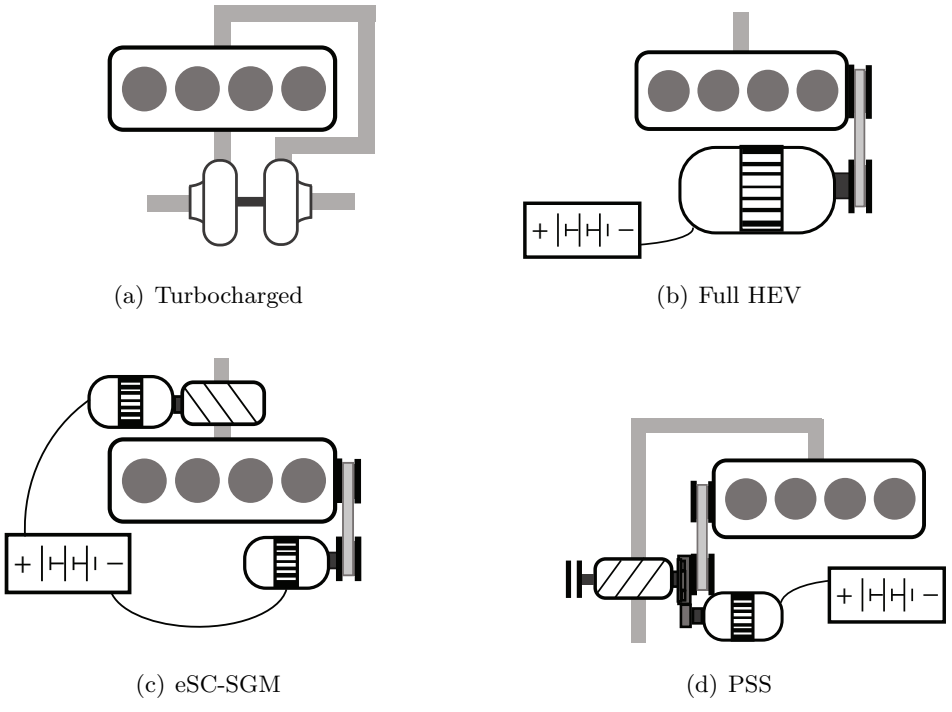

(a) Turbocharged

(b) Full HEV

(c) eSC-SGM

(d) PSS

Figure 4.1: Schematic of studied powertrains, (a) turbocharged powertrain, (b) full parallel hybrid electric powertrain, (c) electric supercharger with starter generator motor, (d) power split supercharger.

due to limited available torque, but it can help reducing the vehicle fuel consumption by decreasing the engine idling time, guiding its operating points into more efficient areas, and partial regenerative braking at a low cost [25, 26].

To lower the cost and simplify the powertrain, full hybrids use downsized Naturally Aspirated (NA) internal combustion engines. The limited torque of the motor in a mild hybrid cannot augment a downsized engine to full torque performance, and requires either a large NA engine or a boosted downsized one. With the electric storage capability supporting a mild hybrid system, it is possible to use an electrified boosting device, which unlike broadly used turbochargers, has the ability of fast engine torque management [10, 12, 18]. Electric boosting was not attractive to industry in the past because the 12 V battery systems are not capable of providing sufficient power [69–71].

In this chapter the hybrid functionalities of the power split supercharger, is used to augment the performance of a downsized NA engine. PSS is capable of both parallel hybrid operation and power split boosting, but not at the same time. Figure 4.1(d) shows a schematic view of an engine with PSS and Figure 4.2 displays more details about the system in a vehicle configuration. PSS is configured with a supercharger, a motor and a planetary gear set. The motor can supply/draw torque directly from the engine crankshaft or drive the supercharger for flexible boost pressure production. During vehicle acceleration, when the requested driver torque exceeds the naturally aspirated limit of the ICE, the Energy Management System (EMS) of the vehicle has to decide whether to use the hybrid system in supercharging mode or to supply the motor torque directly into the engine crankshaft to meet the driver demand. So the optimal control problem is formulated with a binary variable defining the boosting or torque assist mode and a continuous variable defining the torque provided by the motor.

This structure change increases the complexity of the energy management problem, because the limits of the engine produced torque and the availability of the motor for torque assist/regeneration depends on a new optimization variable, which is the PSS operating mode. The EMS for HEVs with such system has not advanced yet. The closest analogy in literature are HEVs equipped with electrified turbochargers (eTC) [7, 72, 73]. Note that unlike the studied system, in these HEVs the electric motor coupled to the turbocharger shaft is used for turbo-lag reduction and not boosting during steady state. These systems have two separate electric motors, for boosting and torque assist, thus their powertrain structure and limits are not coupled to an optimization input.

An alternative to the PSS is an electric Supercharger (eSC) with a Starter-Generator Motor (SGM) as shown in Figure 4.1(c). This system provides both mild hybrid capabilities and flexible supercharging but with two separate motors. Therefore, it is a more flexible structure but also heavier and more expensive. Unlike the PSS, which mostly uses crank energy to power the supercharger, the eSC uses solely electric energy, which involves electro-mechanical conversion and storage losses, but the energy can be produced from regenerative

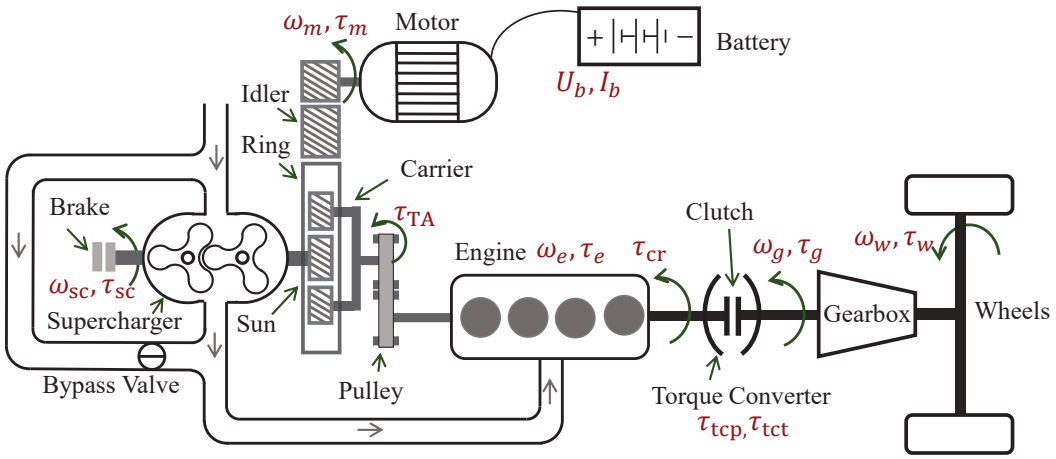

Figure 4.2: Schematic view of the vehicle and drivetrain with the power split supercharger.

braking. Hence, the effectiveness of this structure compared to the PSS remains to be explored in this work.

This chapter formulates the optimal energy management of a downsized engine with the power split supercharger, the double motor system (eSC-SGM) and a full parallel HEV, displayed in Figure 4.1(b), and compares the relative fuel consumption of these configurations under optimal energy management strategy to each other and a baseline turbocharged engine, shown in Figure 4.1(a). Furthermore, this work answers the critical question that during high torque demands whether the limited available electrical energy should be added to the engine air path to feed more air into the ICE and produce a higher torque from it, or the electrical energy should be supplied directly to the crankshaft, and how does the solution changes for different driving profiles, battery sizes, and compressor efficiencies. Both mild hybrid systems are capable of start/stop, regenerative braking, torque assist/regeneration, and variable speed supercharging, while the full hybrid is equipped with a larger motor and high voltage electrical system. All powertrains use the same cylinder block, but the boosted engines can produce a higher torque equivalent to a larger naturally aspirated ICE. In the final part of the paper a consumption minimization rule for selecting the PSS mode is introduced, in which the equivalent fuel consumption of the motor is found through inverting the solution of the optimization. This rule is integrated into the optimal control problem and its effectiveness is compared against the optimal solution and two simpler rules.

4.1 Studied Vehicle and Powertrains

The modeled vehicle is a Ford Escape MY2015 with 6 speed automatic transmission. The baseline engine is a 1.6L EcoBoost gasoline 4 cylinder 4 stroke spark ignition turbocharged engine. The alternative powertrains use EcoBoost engine after removing its turbocharger.

Figure 4.2 shows a schematic view of the vehicle with a PSS and the associated variables of various components.

The PSS system consists of a planetary gear set, a motor, a roots supercharger, a brake, and a bypass valve. The supercharger is connected to the sun gear within the planetary gear set, the motor is connected to the ring gear through the idler gear and the carrier is connected to the engine crankshaft through a set of belt and pulleys. The motor is powered by a 48 V system and has a nominal power of 9 kW and a peak power of 12 kW. In boosting mode, realized by releasing the brake and closing the bypass, the motor adjusts the supercharger produced boost pressure independently of the engine speed, which is superior to conventional mechanical supercharging due to fast engine torque response and lower throttling losses. In parallel hybrid mode, achieved by engaging the brake and bypassing the supercharger, the motor can supply/draw torque from the crankshaft for start/stop, regenerative braking, torque assist or regeneration. This operation mode is called torque assist mode throughout this work.

In the hybrid configuration with electric supercharger and starter generator motor (called eSC-SGM in this work), the same roots compressor as in the PSS is used. Moreover, both electric motors in this system are similar to the PSS motor. The motor in the full HEV powertrain has a nominal power of 45 kW and peak power of 60 kW with 300 V electric system and it is placed in parallel to the engine as shown in Figure 4.1(b).

4.2 Vehicle Model for Optimal Energy Management

4.2.1 Vehicle and Driveline Model

Given the vehicle speed profile, the vehicle tractive force, F_t, is computed from the vehicle effective mass, M_v, acceleration and road resistance force, F_r,

$$F_t = M_v \frac{d}{dt} v + F_r \tag{4.1a}$$

$$M_v = m_v + \frac{J_w + \gamma^2 (J_e + J_g)}{r_w^2} \tag{4.1b}$$

$$F_r = C_0 + C_1 v + C_2 v^2 \tag{4.1c}$$

where, v is the vehicle speed, m_v is the vehicle mass and γ is the gear ratio. The second term in (4.1b) is the rotational mass of the engine, gear and wheels, calculated from their inertia, J_e, J_g and J_w, wheels radius, r_w and gear ratio. The EPA reported dynamometer correction factors, C_0, C_1 and C_2 are used for computing the road resistance force. The road grade in (4.1) is assumed to be zero. The torque at the wheels, τ_w, and the wheels rotational speed, ω_w, are given by:

$$\tau_w = F_t r_w \tag{4.2a}$$

$$\omega_w = \frac{v}{r_w}. \tag{4.2b}$$

The rotational speed on the engine side of the gearbox, ω_g is as follows:

$$\omega_g = \gamma \omega_w. \tag{4.3}$$

It is assumed that when the engine is on at low vehicle velocity the engine speed, ω_e, does not drop to less than its idle speed, $\omega_{e,idle}$, and when the engine is turned off the engine speed drops to zero. It is also assumed that at any engine speed larger than the idling speed the torque converter is locked,

$$\omega_e = \begin{cases} \max(\omega_g, \omega_{e,\text{idle}}) & \text{if} \quad u_e = 1 \\ 0 & \text{otherwise} \end{cases} \tag{4.4}$$

in which u_e is the engine on/off control signal and $u_e = 1$ indicates that the engine is turned on. The torque converter pump torque, τ_{tcp}, and turbine torque, τ_{tct}, are computed from the torque converter K-factor, K, and its torque ratio, TR, both of which are function of the turbine to pump speed ratio, SR,

$$\text{SR} = \frac{\omega_{\text{tct}}}{\omega_{\text{tcp}}} \tag{4.5a}$$

$$\tau_{\text{tcp}} = \left(\frac{\omega_{\text{tcp}}}{K}\right)^2 \tag{4.5b}$$

$$\tau_{\text{tct}} = \tau_{\text{tcp}} \times \text{TR} \tag{4.5c}$$

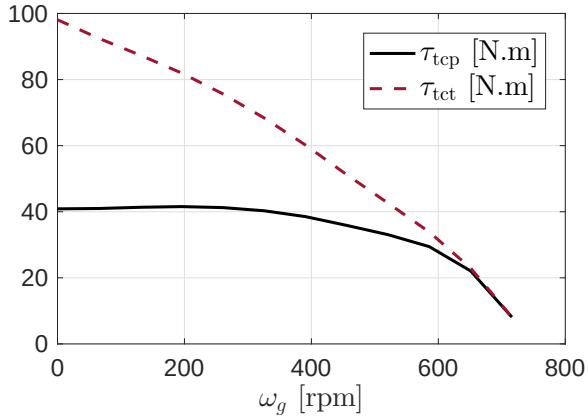

Figure 4.3: The torque converter pump and turbine transmitted torque at engine idling.

where ω_{tct} is the torque converter turbine speed, and ω_{tcp} is the torque converter pump speed equal to the engine speed. Figure 4.3 shows the transmitted torque trough the pump and turbine when the clutch is unlocked. Define τ_g as requested torque by the speed profile on the gearbox shaft as follows:

$$\tau_g = \frac{\tau_w}{\gamma}\eta_g^{-\text{sgn}(\tau_w)} \tag{4.6}$$

in which η_g is the gear box efficiency. The torque on the crankshaft, τ_{cr}, transmitted through the clutch and pump, is computed as,

$$\tau_{\text{cr}} = \begin{cases} \tau_g & \text{if} \quad \omega_e = \omega_g \\ \tau_{\text{tcp}} + \max(0, \tau_g - \tau_{\text{tct}}) & \text{otherwise.} \end{cases} \tag{4.7}$$

The above equation implies,

- When the torque converter clutch is locked the torque on the engine shaft is equal to the drive cycle requested torque.
- When the torque converter clutch is not locked, if the drive cycle requested torque is larger than the turbine torque, $\tau_g > \tau_{\text{tct}}$, then the rest of the requested torque is transmitted through the slipping clutch.
- When the torque converter clutch is not locked, if the drive cycle requested torque is smaller than the turbine torque, $\tau_g < \tau_{\text{tct}}$, such as when braking, no torque is transmitted through the clutch, the torque on the engine shaft is equal to τ_{tcp} and the extra torque transmitted through the turbine is wasted in the friction brakes, i.e. no regenerative braking is possible in this operating condition.

4.2.2 Powertrain Model with PSS

4.2.2.1 Engine Model

The engine and motor have to supply the driver requested torque,

$$\tau_e = \max(\tau_e^{\min}, \tau_{\text{cr}} - \tau_{\text{TA}}) \tag{4.8}$$

$$\tau_b = \min(0, \tau_{\text{cr}} - \tau_{\text{TA}}) \tag{4.9}$$

where τ_{TA} is the torque from the motor transmitted through the pulley to the crankshaft, $\tau_e^{\min}$ is the minimum engine torque and τ_b is the part of the crankshaft torque dissipated in friction brakes. During vehicle deceleration ($\tau_{\text{cr}} < 0$) the electric motor can recuperate part of the vehicle kinetic energy and the rest is dissipated in the friction brakes.

The Supercharger brake position, u_{br}, is used for representing the PSS two modes. When the supercharger is braked, $u_{\text{br}} = 1$, the NA engine produces a lower torque but it can receive

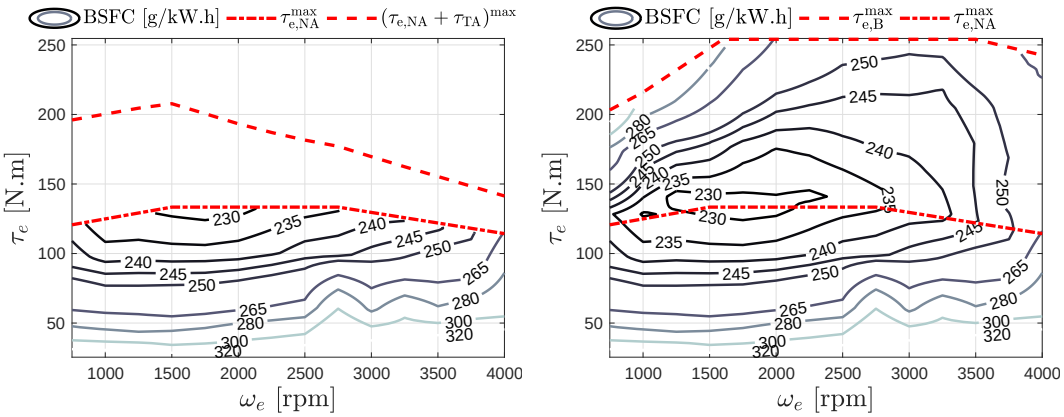

(a) Torque assist mode

(b) Boosting mode

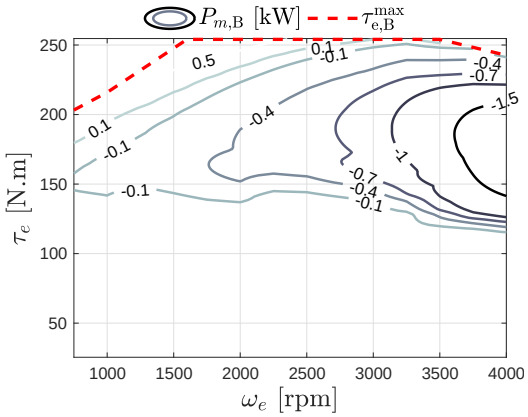

(c) Motor power for boosting

Figure 4.4: Contours of BSFC for, (a) the naturally aspirated 1.6 L (b) the supercharged engine using PSS (c) motor power in boosting mode.

torque assist from the motor. The NA engine torque limit is shown in Figure 4.4(a) along with the maximum powertrain torque in torque assist mode $(\tau_{e,\mathrm{NA}}+\tau_{\mathrm{TA}})^{\max}$ and the engine BSFC map. When the brake is released, $u_{\mathrm{br}}=0$, the engine has to supply all the requested torque. In this mode the engine can produce a higher torque because the supercharger supplies more air into the engine. Figure 4.4(b) shows the maximum engine produced torque and BSFC map in boosting mode. The engine BSFC map is produced using the GT-Power engine model. Finally, the engine maximum produced torque is set to zero when turned off.

This mode switch and system structure change are modeled through imposing input dependent constrains on the engine and motor produced torque

$$\tau_e^{\max}=\begin{cases}0 & \text{if} \quad u_e=0\\ \tau_{e,\mathrm{B}}^{\max}(\omega_e) & \text{if} \quad u_{\mathrm{br}}=0, u_e=1\\ \tau_{e,\mathrm{NA}}^{\max}(\omega_e) & \text{otherwise.}\end{cases} \tag{4.10}$$

Engine BSFC is used for computing the engine fuel flow rate, $\dot{m}_f$. A minimum fuel flow rate, $\dot{m}_{f,\min}$, is imposed[1]

$$\mathrm{BSFC} = \Gamma(\tau_e, \omega_e) \tag{4.11a}$$

$$\tilde{\dot{m}}_f = P_e \times \mathrm{BSFC} \tag{4.11b}$$

$$\dot{m}_f = \max(\tilde{\dot{m}}_f, \dot{m}_{f,\min}) \tag{4.11c}$$

where P_e is the engine brake power.

4.2.2.2 Motor Model

- Torque assist mode.

  The motor torque is an independent input when the PSS is in torque assist mode but not in boosting mode because in this mode the motor torque and speed depend on the engine required boost pressure. To overcome this complexity a new parameter is defined as the commanded torque assist, $\tau_{m,\mathrm{TA}}$, constrained according to the hybrid mechanism mode as follows:

$$\tau_{m,\mathrm{TA}}^{\min} \le \tau_{m,\mathrm{TA}} \le \tau_{m,\mathrm{TA}}^{\max} \tag{4.12a}$$

$$\tau_{m,\mathrm{TA}}^{\max} = \begin{cases} 0 & \text{if} \quad u_e = 0 \quad \text{or} \quad u_{\mathrm{br}} = 0 \\ \tau_m^{\max} & \text{otherwise} \end{cases} \tag{4.12b}$$

$$\tau_{m,\mathrm{TA}}^{\min} = \begin{cases} 0 & \text{if} \quad u_e = 0 \quad \text{or} \quad u_{\mathrm{br}} = 0 \\ \tau_m^{\min} & \text{otherwise} \end{cases} \tag{4.12c}$$

  where $\tau_m^{\max}$ and $\tau_m^{\min}$ are respectively the motor maximum and minimum torque limits, $u_e = 0$ means engine is turned off and $u_{\mathrm{br}} = 0$ stands for boosting mode for PSS. The motor speed, ω_m and the torque transmitted to/from the engine crankshaft, τ_{TA}, are related to the engine speed and the commanded motor torque assist as follows,

$$\omega_{m,\mathrm{TA}} = \frac{n_{\mathrm{im}} n_{\mathrm{ri}} (g_S + g_R)}{g_R} \omega_e \tag{4.13a}$$

$$\tau_{\mathrm{TA}} = \frac{n_{\mathrm{im}} n_{\mathrm{ri}} (g_S + g_R)}{g_R} \tau_{m,\mathrm{TA}} \tag{4.13b}$$

  where n_{im} and n_{ri} are idler to motor and ring to idler gear ratios, g_R is the ring gear teeth number and g_S is the sun gear teeth number. The power transfer efficiency is assumed to be 100% within the planetary gear set. Note that the PSS pulley ratio is equal to 1.

[1] The minimum fuel flow rate is assumed to be 1.0 $\frac{\mathrm{kg}}{\mathrm{h}}$.

- Boosting mode.

  When the supercharger brake is released the motor drives the supercharger to supply the required air into the engine. The motor torque and speed are computed as follows in this case

$$\tau_{m,\mathrm{B}} = -\frac{g_R}{n_{\mathrm{im}} n_{\mathrm{ri}} g_S} \tau_{\mathrm{sc}} \tag{4.14a}$$

$$\omega_{m,\mathrm{B}} = \frac{(g_S + g_R) n_{\mathrm{im}} n_{\mathrm{ri}}}{g_R} \Big(\omega_e - \frac{g_S}{g_S + g_R} \omega_{\mathrm{sc}} \Big) \tag{4.14b}$$

  where τ_{sc} is the supercharger torque and ω_{sc} is the supercharger rotational speed, both depending on the engine operating point.

$$\tau_{\mathrm{sc}} = \Lambda(\tau_e, \omega_e) \tag{4.15a}$$

$$\omega_{\mathrm{sc}} = \Pi(\tau_e, \omega_e) \tag{4.15b}$$

The manufacturer provided map is used for computing the motor power,

$$P_m = \Gamma(\omega_m, \tau_m) \tag{4.16}$$

where the motor speed and torque, ω_m, τ_m, are as follows

$$(\tau_m, \omega_m) = \begin{cases} (\tau_{m,\mathrm{B}}, \omega_{m,\mathrm{B}}) & \text{if} \quad u_{\mathrm{br}} = 0 \\ (\tau_{m,\mathrm{TA}}, \omega_{m,\mathrm{TA}}) & \text{otherwise.} \end{cases} \tag{4.17}$$

Figure 4.4(c) shows the motor power at boosting mode computed using $\tau_{m,\mathrm{B}}$ and $\omega_{m,\mathrm{B}}$. For most of operating points the motor power is negative, meaning that it generates some power during boosting. During high load operating conditions, such as when climbing a hill, the motor will be slightly charging the battery, while the supercharger is boosting the engine. This feature allows continuous employment of the PSS at high load points without concerns regarding battery depletion.

4.2.3 Powertrain Model for eSC-SGM

The engine with electric supercharger and starter generator motor has two separate motors for torque assist and boosting, thus the supercharger is always available for boosting and the engine maximum torque limit is equal to the boosting limit shown in Figure 4.5.

$$\tau_e^{\max} = \begin{cases} 0 & \text{if} \quad u_e = 0 \\ \tau_{e,\mathrm{B}}^{\max}(\omega_e) & \text{otherwise.} \end{cases} \tag{4.18}$$

The engine torque limit with eSC is higher at low engine speeds compared to the PSS,

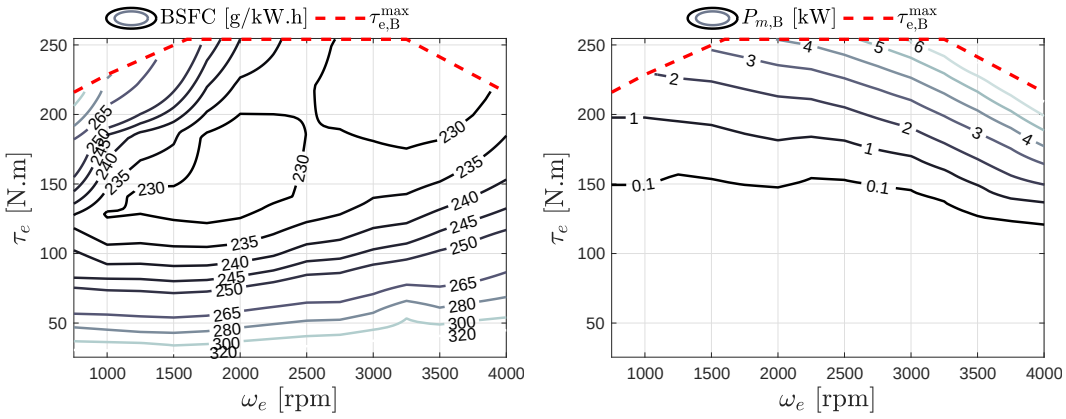

(a) BSFC

(b) Motor power for boosting

Figure 4.5: The electrically supercharged engine, (a) BSFC contour, (b) motor power for supercharging.

due to the removed parasitic loss of the supercharger. At high engine speeds the engine with eSC produces a lower torque because the supercharger power is restricted to 10 kW. Figure 4.5(a) shows the engine with eSC BSFC map. Compared to BSFC map of the engine with PSS, shown on Figure 4.4(b), the efficiency sweet spot of the engine with eSC covers a larger area. The reason is that unlike the PSS, the electric supercharger is not powered by the engine. The eSC energy consumption penalty is paid through electric energy though, shown in Figure 4.5(b).

4.3 Optimal Control Problem

Table 4.1 shows a summary of optimal control problem for energy management of the vehicle with different powertrains. For the vehicle with turbocharged engine, there is no hybridization and the engine has to support the drive cycle requested torque, hence only the gear shifts, u_g, are optimized. The cost function for this case penalizes the fuel flow rate, $\dot{m}_f$, and the gear change. The variable k refers to the k^{th} step time. The problem sampling time, T_s, is taken equal to 1 second, n_g is the gear number and N is the problem horizon, equal to the full drive cycle horizon. Note that using gear shift as the optimization input results in a more natural gear strategy, which is one shift up or down at a time, instead of selecting an arbitrary gear number at each step time. The weighting factor α controls the frequency of gear shifts [31], taken equal to 0.4 for all cases.

The modeled inputs for the optimal control problem of the full HEV and the vehicle with eSC-SGM are the gear shift, engine on/off command, u_e, and the motor torque (τ_m for the full HEV and the starter/generator motor torque, $\tau_{m,\mathrm{TA}}$ for eSC-SGM system). For both systems the battery state of charge, ζ, the gear number and the engine on/off state, x_e, are the modeled system states. The fuel penalty β is associated with each engine cranking,

Table 4.1: Summary of optimal control problem for energy management of different powertrains.

Turbocharged • input: gear shift, $\begin{bmatrix} u_g \end{bmatrix}$. • state: gear number, $\begin{bmatrix} n_g \end{bmatrix}$. • cost function: $J = \sum_{k=1}^{N} \Big(\dot{m}_f(k) T_s + \alpha \lvert n_g(k) - n_g(k-1) \rvert \Big)$	**Full HEV** • inputs: motor torque, gear shift, engine on/off, $\begin{bmatrix} \tau_m, & u_g & u_e \end{bmatrix}$. • states: state of charge, gear number, engine on/off, $\begin{bmatrix} \zeta & n_g & x_e \end{bmatrix}$. • cost function: $J = \sum_{k=1}^{N} \Big(\dot{m}_f(k) T_s + \alpha \lvert n_g(k) - n_g(k-1) \rvert + \beta \max\big(x_e(k) - x_e(k-1), 0\big) \Big)$
eSC-SGM • inputs: SGM torque, gear shift, engine on/off, $\begin{bmatrix} \tau_{m,\mathrm{TA}} & u_g & u_e \end{bmatrix}$. • states: state of charge, gear number, engine on/off, $\begin{bmatrix} \zeta & n_g & x_e \end{bmatrix}$. • cost function: $J = \sum_{k=1}^{N} \Big(\dot{m}_f(k) T_s + \alpha \lvert n_g(k) - n_g(k-1) \rvert + \beta \max\big(x_e(k) - x_e(k-1), 0\big) \Big)$	**PSS** • inputs: commanded torque assist, gear shift, engine on/off, PSS mode, $\begin{bmatrix} \tau_{m,\mathrm{TA}} & u_g & u_e & u_{\mathrm{br}} \end{bmatrix}$. • states: state of charge, gear number, engine on/off, $\begin{bmatrix} \zeta & n_g & x_e \end{bmatrix}$. • cost function: $J = \sum_{k=1}^{N} \Big(\dot{m}_f(k) T_s + \alpha \lvert n_g(k) - n_g(k-1) \rvert + \beta \max\big(x_e(k) - x_e(k-1), 0\big) + \lambda\big(1 - u_{\mathrm{br}}(k)\big) \Big)$

and is taken as 0.28 grams of fuel in the optimization cost function. The optimal control problem for the vehicle with PSS is described in more details in the following section.

4.3.1 Optimal Control Problem for Engine with PSS

The cost function for the vehicle with PSS penalizes the fuel consumption, gear shift, engine cranking and the PSS mode, u_{br}, as follows:

$$\min \Bigg\{ \sum_{k=1}^{N} \Bigg(\dot{m}_f(k) T_s + \alpha \lvert n_g(k) - n_g(k-1) \rvert + \beta \Big(\max\big(x_e(k) - x_e(k-1), 0\big) \Big) + \lambda\big(1 - u_{\mathrm{br}}(k)\big) \Bigg) \Bigg\} \tag{4.19}$$

in which λ is a very small number to keep the PSS in torque assist mode ($u_{\mathrm{br}} = 1$) as default. This term only plays a role when neither supercharging nor torque assist are used such as when the engine is turned off. Similar to other hybrid powertrains, the modeled system states include the battery state of charge, gear number, and the engine on/off state. The optimization inputs are the commanded torque assist, gear shift command, the PSS mode,

and the engine on/off command. The problem constraints are:

$$\zeta(k+1) = \zeta(k) - \frac{I_b(k)}{3600 C_n} T_s \tag{4.20a}$$

$$n_g(k) = u_g(k) + n_g(k-1) \tag{4.20b}$$

$$x_e(k) = u_e(k) \tag{4.20c}$$

$$\zeta^{\min} \leq \zeta(k) \leq \zeta^{\max} \tag{4.20d}$$

$$I_b^{\min} \leq I_b(k) \leq I_b^{\max} \tag{4.20e}$$

$$\tau_{m,\mathrm{TA}}^{\min} \leq \tau_{m,\mathrm{TA}}(k) \leq \tau_{m,\mathrm{TA}}^{\max} \tag{4.20f}$$

$$\tau_e^{\min} \leq \tau_e(k) \leq \tau_e^{\max} \tag{4.20g}$$

$$\omega_e^{\min} \leq \omega_e(k) \leq \omega_e^{\max} \tag{4.20h}$$

$$u_g(k) \in \{-1, 0, 1\} \tag{4.20i}$$

$$n_g(k) \in \{1, 2, \cdots, 6\} \tag{4.20j}$$

$$u_{\mathrm{br}}(k), u_e(k) \in \{0, 1\} \tag{4.20k}$$

$$u_e(k) = 1 \ \text{ if } \ v(k) > 0 \tag{4.20l}$$

$$\tau_e(k) \not> 0 \ \text{ if } \ \tau_{\mathrm{cr}}(k) < 0 \tag{4.20m}$$

$$\zeta(N) = \zeta(0) \tag{4.20n}$$

where (4.20a) is the state of charge dynamics, I_b is the battery current and C_n is the battery capacity. The constraint (4.20b) presents the gear state, and (4.20c) defines the engine on/off state. The constraint (4.20d) limits the battery state of charge, (4.20e) constrains the battery current, (4.20f) restricts the commanded torque assist, (4.20g) and (4.20h) confine the engine speed, ω_e, and torque, τ_e, (4.20i) limits the gear shift to one gear up and down at each step time, (4.20j) restricts the gear number to 1 to 6, (4.20k) limits the engine mode and the PSS mode to on/off and boosting/torque assist respectively, (4.20l) permits turning off the engine only when the vehicle is stopped, (4.20m) does not permit regenerative braking and generation simultaneously and (4.20n) imposes charge sustaining condition. Similar constraints are imposed for the optimal control problem of other powertrains.

A numerical optimization method has to be used to find the global optimum solution of (4.19). Dynamic Programming (DP) and stochastic dynamic programming [31, 74], are among the most popular approaches. Pontryagin's Minimum Principle (PMP) [75,76], convex optimization [77], model predictive control [78], and equivalent consumption minimization [79–81] are other well established methods. In this work, a MATLAB-based dpm function [82] that applies dynamic programming is used for finding the solution of this discretized optimal control problem. Note that DP is acausal and solved backwards in time, hence cannot be implemented online, nevertheless it provides a benchmark for evaluating different powertrains and finding optimal policies.

4.4 Optimization Results

4.4.1 Fuel Consumption Under Optimal Energy Management

Table 4.2 presents the predicted Fuel Economy (FE) numbers for the baseline turbocharged engine with optimized gear ratio, compared to the FE of the electrified and hybridized powertrains with the same engine under optimal energy management. A 1.2 kWh battery is assumed for all the cases. The fuel economy improvement compared to the baseline turbocharged engine is written in parenthesis next to the reported FE number for each case. The results indicate that up to 32.9% FE increase is possible on the FTP75 drive cycle with the PSS. The FE improvement for the engine with eSC-SGM is similar to the PSS case despite its higher flexibility. The larger motor for the full HEV permits recovering a larger part of the energy wasted during vehicle braking, resulting in a larger FE improvement of 45.4% on this cycle.

A comprehensive study on supercharging impact on drive cycle fuel consumption of a vehicle is carried out by authors in [13]. It was shown that with the PSS solely used as a supercharger the reduced backpressure contributes to around 1% fuel consumption reduction on FTP75 and HWFET drive cycles, while the higher fuel penalty associated with the transients increases the US06 cycle fuel consumption.

Both the PSS and eSC-SGM systems increase the vehicle FE on HWFET by only 4.3%, which is significantly smaller than the FTP75 benefit, because HWFET cycle does not contain as many braking and stopping instances, hence there is less opportunity for fuel consumption reduction. Similarly, the FE improvement for the full HEV is also small at 6.5%.

The higher flexibility of eSC-SGM system indicates an advantage over the US06 cycle, where both the supercharger and the starter-generator motor can feed the powertrain to meet the cycle high torque demand efficiently. Nevertheless, the full HEV provides a significantly larger FE benefit over the US06, compared to both mild hybrid systems, mainly because the smaller motor in these systems can only partially recover the wasted energy during aggressive braking instances in the US06 cycle.

The last row in Table 4.2 shows the fuel economy of different systems on combined cycle computed with allocated weights of 0.55 and 0.45 to the FTP75 and HWFET cycles fuel consumption respectively [83]. On the combined cycle both mild hybrid systems provide the same FE increase of 20.7% which is around 75% of the full HEV benefit that is 28.2% improvement compared to the baseline turbocharged engine.

4.4.2 Optimized Supercharging and Torque Assist Share

This part takes a closer look into the supercharging versus torque assist share for the PSS and eSC-SGM. Figure 4.6 displays the optimal trajectories for a segment of the US06 drive cycle. The top left subplot represents the vehicle velocity, v. The bottom left subplot

Table 4.2: DP drive cycle simulation results. The numbers in parenthesis show the relative fuel economy improvement compared to the turbocharged engine

Drive cycle	Turbocharged FE [mpg]	Engine + PSS FE [mpg]	Engine + eSC-SGM FE [mpg]	Full HEV FE [mpg]
FTP75	34.79	46.25 (32.9%)	46.21 (32.8%)	50.60 (45.4%)
HWFET	48.57	50.67 (4.3%)	50.68 (4.3%)	51.74 (6.5%)
US06	30.29	32.46 (7.2%)	32.86 (8.5%)	35.83 (18.3%)
Combined	39.88	48.14 (20.7%)	48.12 (20.7%)	51.11 (28.2%)

shows the gear number. The black line shows the gear number for the engine with PSS, the red line stands for the engine with eSC-SGM and the dashed green line represents the full HEV. The full HEV shifts up faster at the beginning of the transient and downshifts less during the accelerations. The middle top subplot represents the engine torque and its lower subplot shows the torque assist from the motor on the crankshaft, τ_{TA}. The right top subplot shows the electric power used for boosting the engine, $P_{m,\mathrm{B}}$, and the bottom plot shows the PSS operating mode during the shown time interval, where $u_{\mathrm{br}} = 1$ stands for the torque assist mode and $u_{\mathrm{br}} = 0$ represents boosting mode.

The optimal solution for full HEV in Figure 4.6 keeps the engine torque around naturally aspirated torque limit (around 130 N.m, see Figure 4.4(a)), where the engine is highly efficient, and uses the torque assist from the motor to meet the cycle demanded torque. The engine with PSS often uses the PSS in boosting mode to provide large torque demands and uses torque assist for augmenting the engine torque at medium torques. Note that in boosting mode the PSS motor generates some electric power, hence its boosting power sign is negative (the PSS motor power map in boosting mode is shown in Figure 4.4(c)). The

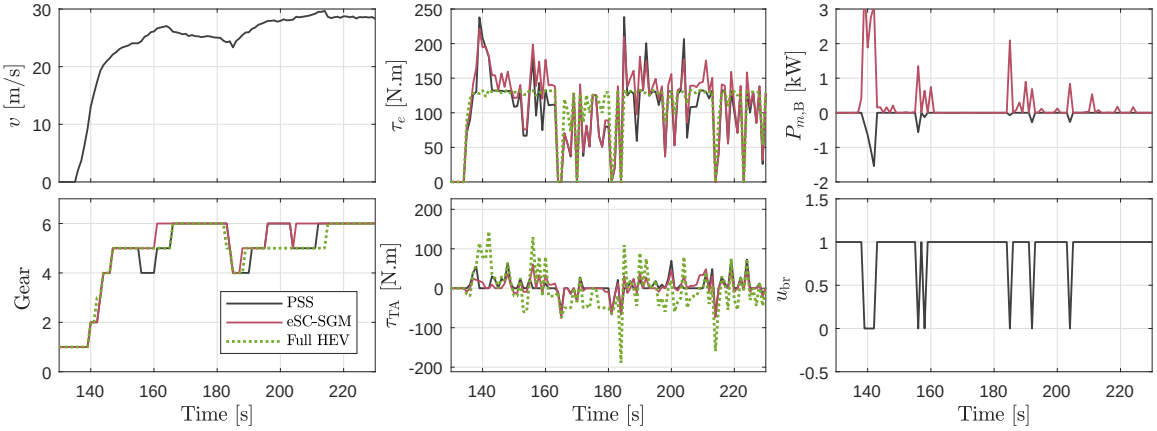

Figure 4.6: Optimal trajectories for engine with PSS compared to eSC-SGM and full HEV from dynamic programming. Top row from left: vehicle speed profile, engine torque, and power used for boosting the engine, bottom row from left: gear number, the torque assist from the motor on the crankshaft, and the PSS operating mode.

engine with eSC on the other hand, uses help from both the supercharger and SGM to meet large torque requests. In the following sections the power share between the engine and the motor is explained in more details and its sensitivity to the battery size and the supercharger efficiency is explored. In order to realize different battery sizes, the capacity, C_n, and the internal resistance, R_b, of the battery model are scaled as,

$$C_{n,s} = \alpha_s C_n \tag{4.21}$$

$$R_{b,s} = \frac{R_b}{\alpha_s} \tag{4.22}$$

where $C_{n,s}$ is the scaled battery capacity, $R_{b,s}$ is the scaled battery internal resistance, and α_s is a scaling factor. For example the internal resistance of a 0.6 kWh battery is twice the internal resistance of a 1.2 kWh battery. The battery mass is also scaled to take into account the weight difference.

4.4.2.1 Engine with PSS

Figure 4.7(a) shows the PSS optimal operating mode for the three studied cycles with a 1.2 kWh battery. The red markers indicate boosting and blue ones represent torque assist mode. The FTP75, HWFET and US06 operating points are shown with stars, triangles and circles respectively. The horizontal axis is the engine speed and the vertical axis is the requested crank torque. The yellow area, which is under the engine maximum produced torque in boosting mode, $\tau_{e,B}^{\max}$, and above the maximum powertrain torque when the PSS is in torque assist mode, $(\tau_{e,\mathrm{NA}} + \tau_{\mathrm{TA}})^{\max}$, is the operating points that can be achieved only through supercharging. An operating point lying within the green area, which is above the NA torque limit of the engine, $\tau_{e,\mathrm{NA}}^{\max}$, and under $(\tau_{e,\mathrm{NA}} + \tau_{\mathrm{TA}})^{\max}$, can be realized with either torque assist or supercharging mode. In the green region the optimal solution from DP mostly chooses torque assist except for some operating points on the US06 and HWFET cycles, most of which lie within the efficiency sweet spot of the engine. This result is in agreement with the authors finding in [32] and previous chapter, which focused on the design of low-level controllers for the PSS system in a super-turbo configuration. It was shown that for a typical constant speed torque tip-in, supercharging can be the fuel optimal strategy for medium load points, because the operating point remains within the high efficiency region of engine map.

On the FTP75 cycle the optimal controller always chooses torque assist mode when both modes are possible due to the higher availability of electric energy from regenerative braking on this cycle. Figures 4.7(b) and 4.7(c) show the PSS operating mode for a 0.6 kWh and a 0.3 kWh battery. For a smaller battery the occasions that the optimal controller picks supercharging mode over torque assist mode increases. The first reason is that less electric energy is available in a smaller battery and since boosting mode consumes less electric power, it is more favorable for a smaller battery. Second, the internal resistance of a battery is

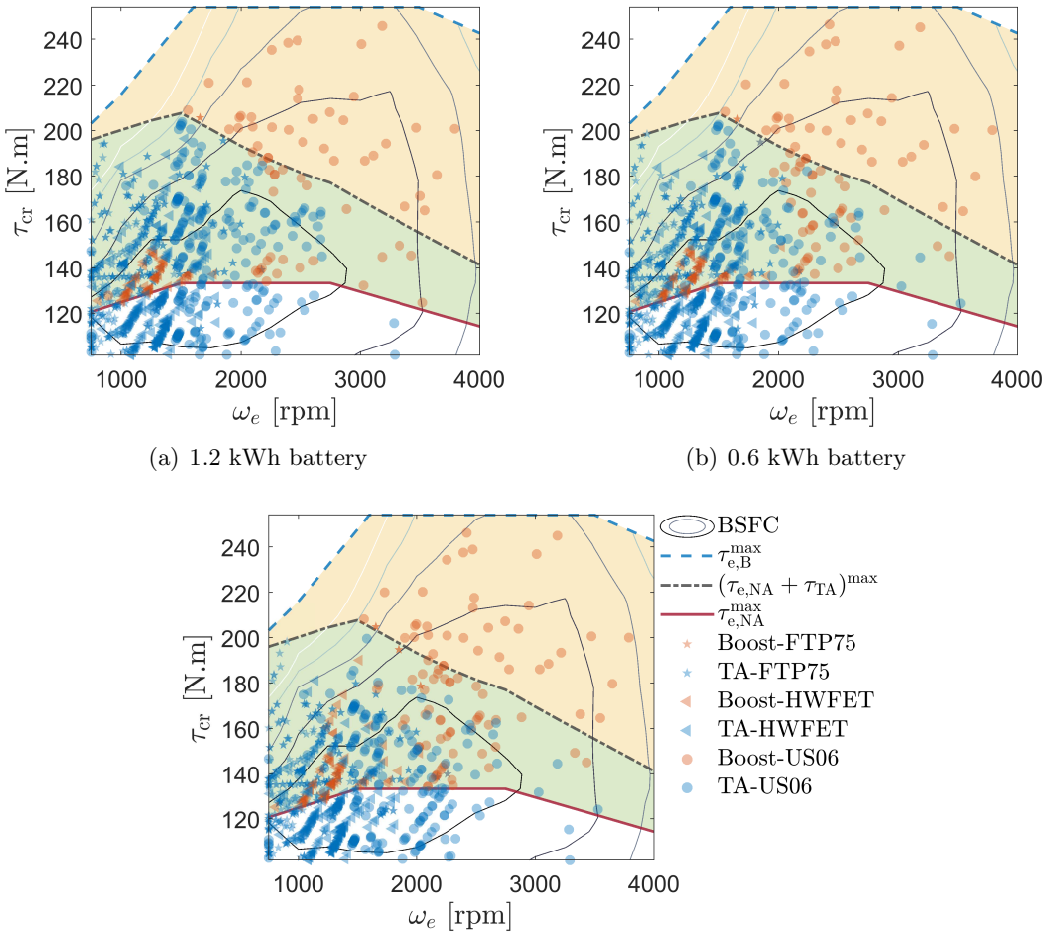

(a) 1.2 kWh battery

(b) 0.6 kWh battery

(c) 0.3 kWh battery

Figure 4.7: Optimal power split supercharger mode based on the requested torque on crankshaft and engine speed for different drive cycles. Blue markers stand for torque assist and red markers represent supercharging mode for (a) a 1.2 kWh battery, (b) a 0.6 kWh battery, (c) a 0.3 kWh battery.

inversely proportional to its capacity, resulting in a larger battery loss for a smaller battery. Consequently, the torque assist option becomes less efficient as the battery size decreases.

4.4.2.2 Engine with eSC-SGM

Both the PSS and eSC provide flexible engine boost pressure control. However, the PSS is mostly powered by the crankshaft, while eSC is powered by the battery, thus it is more flexible in terms of energy source. This section investigates the sensitivity of supercharging versus torque assist share in eSC-SGM system to the battery size and supercharger consumed power. In addition, the sensitivity of fuel consumption of this system to the supercharger consumed power is explored.

- Sensitivity to the Battery Size: Figure 4.8 shows the engine with eSC-SGM operating points over the US06 drive cycle on top of the engine BSFC map. The circles show the operating points with a 1.2 kWh battery and the stars show the operating points with a 0.3 kWh battery. Unlike the PSS, the optimal controller uses the electric supercharger even at high load as long as the engine operating point lies within the high efficiency area. Therefore, using the eSC can be more efficient compared to boosting with PSS, because the optimal EMS produces the electric energy efficiently.

  The operating points in Figure 4.8 are colored based on the SGM torque sign. The red color shows that SGM torque is positive meaning that it supplies torque into the engine crankshaft, a blue marker stands for generating and yellow means no torque from SGM. When the engine produces a torque larger that its naturally aspirated limit ($\tau_e > \tau_{e,\mathrm{NA}}$), the SGM is always assisting the crankshaft. This reveals that electric supercharging and generating simultaneously is not an efficient strategy; and it is only efficient to generate when the engine is not boosted.

  The points with star markers show the engine operating points with a 0.3 kWh battery. As explained in the previous section a smaller battery means that the electrical path will be less fuel efficient due to the higher battery losses. Similar to the PSS, the optimal controller uses the eSC more with a smaller battery. This fact is evident in Figure 4.8 since the boosted points have shifted slightly upward with the smaller battery.

- Sensitivity to the Supercharger Consumed Power: The roots supercharger used in this study typically has lower efficiency (less than 70%) compared to the centrifugal

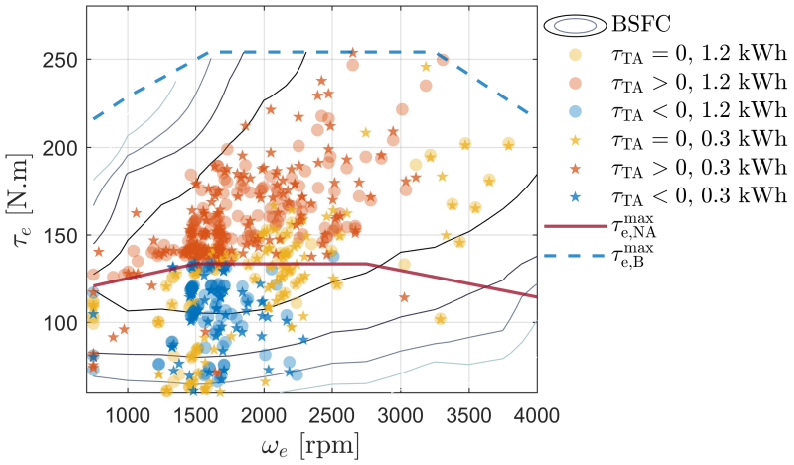

Figure 4.8: Optimal engine operating points with eSC-SGM over the US06 and with two different battery sizes. Red markers mean that the SGM supplies torque to the crankshaft, blue markers mean SGM draws torque from the crankshaft for power generation and yellow means SGM torque is set to zero.

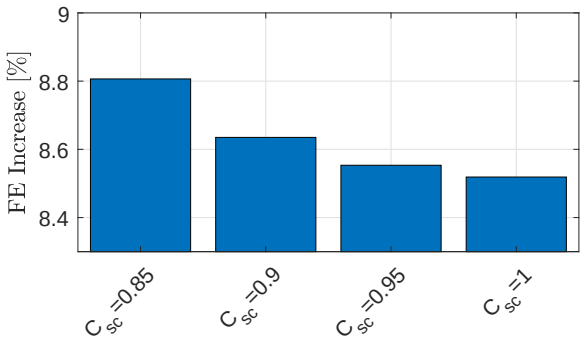

Figure 4.9: The sensitivity of FE gain of eSC-SGM configuration compared to turbocharged engine over the US06 cycle to the supercharger power multiplier, C_{sc}. A smaller C_{sc} means a more efficient supercharger.

type (up to 85%). In this part the power consumed by the supercharger is adjusted by a factor to mimic a more efficient supercharger as follows:

$$\hat{P}_{\text{m,B}} = C_{\text{sc}} \times P_{\text{m,B}}(\tau_e, \omega_e) \tag{4.23}$$

where $P_{\text{m,B}}(\tau_e, \omega_e)$ is the supercharger consumed power from Figure 4.5(b), $\hat{P}_{\text{m,B}}$ is the scaled power, and C_{sc} is a scaling factor. A smaller C_{sc} means a more efficient supercharger. Figure 4.9 shows the sensitivity of the FE gain of the engine with eSC-SGM over the US06 cycle to the C_{sc}. The FE gain is the relative reduction compared to the baseline turbocharged engine. For every 5% improvement in the supercharger efficiency the drive cycle fuel economy gain of the system increases by less than 0.1% on average, such that for a 15% more efficient supercharger the FE gain increases from 8.5% to 8.8%.

A more efficient supercharger also influences the supercharging share. As the supercharger becomes more efficient, the optimal EMS uses the supercharger more and SGM less during high torque requests. Figure 4.10 compares a sample vehicle acceleration with the roots supercharger (C_{sc} = 1) and with an extremely efficient supercharger (C_{sc} = 0.85). As seen the EMS assigns a larger torque share to the engine (bottom left subplot) and less to the torque assist from SGM (top right subplot), while the supercharger consumed power remains smaller for the efficient supercharger case.

4.5 Rule-based Controller for PSS Mode

For a vehicle equipped with the power split supercharger, when the driver torque demand exceeds the naturally aspirated limit of the engine, the vehicle energy management system has to choose between supplying the motor torque directly into the crankshaft or using it for driving the supercharger and boosting the engine. This system mode switch converts the

continuous optimization problem to be solved within an online optimization-based controller (MPC for example) into a nonlinear non-convex mixed integer optimization problem, which is challenging to solve. The alternative approach is to extract a rule for selecting the hybrid mechanism mode based on the global optimization results found here. In this part, three different rules are proposed for selecting the PSS operating mode and the effectiveness of each rule is evaluated by incorporating it into the optimal control problem and comparing the results to the case where the PSS mode is selected by the optimizer. This method is preferred to a feedforward simulation for evaluating the effectiveness of the PSS mode selection rules because this approach isolates the effect of the rule-based strategy on fuel consumption. In a feedforward simulation, the FC depends on the online power split and gear shift controllers in addition to the PSS mode rule-based controller.

4.5.1 Method 1: Boost Assist Rule (BAR)

This rule simply uses the supercharger for all crankshaft requested torques, τ_{cr} from (4.7), larger than the naturally aspirated limit of the engine (above the white region in Figure 4.7)

$$u_{\text{br}}^{\text{BAR}} = \begin{cases} 0 & \text{if} \quad \tau_{\text{cr}} > \tau_{e,\text{NA}}^{\max} \\ 1 & \text{otherwise} \end{cases} \tag{4.24}$$

where $u_{\text{br}}^{\text{BAR}}$ is the PSS mode from boost assist rule. By looking at the DP results it is clear that the preferred time for boosting is when the requested torque is larger than $(\tau_{\text{TA}}+\tau_{e,\text{NA}})^{\max}$, the yellow area in Figure 4.7, however we considered this additional strategy to understand that if the PSS system is used only as a boosting device during large torque requests, how different the vehicle FC would be compared to the other strategies.

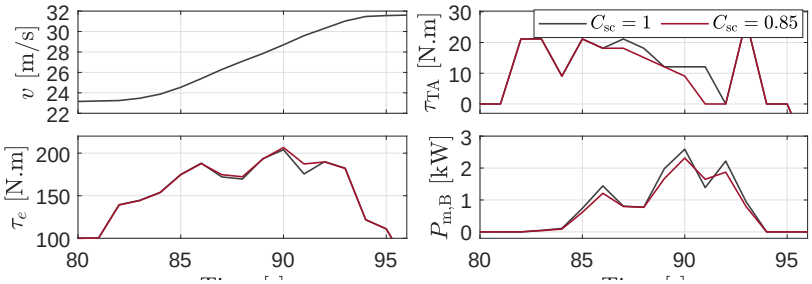

Figure 4.10: Optimal trajectories for the existing supercharger, $C_{\text{sc}} = 1$, and an efficient supercharger $C_{\text{sc}} = 0.85$. Top plots from left: vehicle speed and SGM torque on the crankshaft, bottom from left: engine torque and the boosting motor power.

4.5.2 Method 2: Torque Assist Rule (TAR)

For a large battery as seen in Figure 4.7(a) the optimal controller mostly uses torque assist mode when the torque demand can be realized through both modes. Thus, the second method to control the PSS is to use boosting whenever the requested torque is higher than $(\tau_{\text{TA}} + \tau_{e,\text{NA}})^{\max}$, above the green area in in Figure 4.7,

$$u_{\text{br}}^{\text{TAR}} = \begin{cases} 0 & \text{if} \quad \tau_{\text{cr}} > (\tau_{\text{TA}} + \tau_{e,\text{NA}})^{\max} \\ 1 & \text{otherwise} \end{cases} \tag{4.25}$$

where $u_{\text{br}}^{\text{TAR}}$ is the PSS mode from torque assist rule.

4.5.3 Method 3: Consumption Minimization Rule (CMR)

The third rule selects the PSS mode to minimize the equivalent fuel flow rate of the engine and motor,

$$u_{\text{br}}^{\text{CMR}} = \begin{cases} 0 & \text{if} \quad \tau_{\text{cr}} > (\tau_{\text{TA}} + \tau_{e,\text{NA}})^{\max} \\ 1 & \text{if} \quad \tau_{\text{cr}} \leq \tau_{e,\text{NA}}^{\max} \\ \underset{u_{\text{br}}=0,1}{\arg\min}(\dot{m}_{f,\text{eq}}) & \text{otherwise} \end{cases} \tag{4.26}$$

where $u_{\text{br}}^{\text{CMR}}$ is the PSS mode from consumption minimization method and $\dot{m}_{f,\text{eq}}$ is the equivalent fuel flow rate of the engine and motor computed by assigning an effective specific fuel consumption, α_{eq}, to electric power generation. This strategy uses the boosting mode when the requested torque exceeds the maximum powertrain torque in torque assist mode, yellow area in Figure 4.7, and uses torque assist when the requested torque is less than the naturally aspirate torque limit of the engine. In the green area, which is $(\tau_{e,\text{NA}} + \tau_{\text{TA}})^{\max} \geq \tau_{\text{cr}} > \tau_{e,\text{NA}}^{\max}$, an optimization problem is solved within the DP code to determine the most efficient PSS mode for the given inputs (torque assist, gear number, engine on/off). The equivalent fuel consumption of the engine and motor at each mode is computed as:

- Boosting mode ($u_{\text{br}} = 0$):

$$\dot{m}_{f,\text{eq}} = \dot{m}_f(\tau_e, \omega_e) + \alpha_{\text{eq}} P_m(\tau_e, \omega_e) \tag{4.27a}$$

$$\tau_e = \tau_{\text{cr}} \tag{4.27b}$$

- Torque assist mode ($u_{\text{br}} = 1$):

$$\dot{m}_{f,\text{eq}} = \dot{m}_f(\tau_e, \omega_e) + \alpha_{\text{eq}} P_m(\tau_{\text{m}}, \omega_m) \tag{4.28a}$$

$$\tau_e = \tau_{\text{cr}} - \tau_{\text{TA}} \tag{4.28b}$$

$$\tau_{\text{TA}} = \frac{n_{\text{im}} n_{\text{ri}} (g_S + g_R)}{g_R} \tau_m. \tag{4.28c}$$

The torque assist from the motor on the crankshaft, τ_{TA}, is related to the motor torque though (4.28c). Note that when $\tau_{\text{cr}} > \tau_{e,\text{NA}}$, for both PSS modes the motor power is nonzero, with the difference that in boosting mode the motor power is a function of engine operating point but in torque assist mode the motor power is an independent input.

Inverse optimization approach is used for finding the cost function of an optimization problem given the optimization solution [84]. In this problem it is assumed that DP results are a solution to the following optimal control problem and the value of α_{eq} is inferred accordingly,

$$\dot{m}_{f,\text{eq}} = \min_{\tau_{\text{TA}}, u_{\text{br}}} \left(\dot{m}_f + \alpha_{\text{eq}} P_m \right) \tag{4.29}$$

in which the dependency on speed and torque is dropped from $\dot{m}_f$ and P_m. For simplifying the problem and applying Karush-Kugn-Tucker (KKT) condition let's only consider the points that the PSS is in torque assist mode. Define the optimization variable as $X = [\tau_e \;\; \tau_m]^T$. The optimal control problem of (4.29) converts to the following minimization problem with equality constraints,

$$\min_X J(X) = \min_X \left(\dot{m}_f(X) + \alpha_{\text{eq}} P_m(X) \right) \tag{4.30}$$

subject to,

$$g(X) = \tau_{\text{cr}} - \tau_e - \frac{n_{\text{im}} n_{\text{ri}} (g_S + g_R)}{g_R} \tau_m = 0. \tag{4.31}$$

The constraint $g(X)$ states that the requested torque on the crankshaft is equal to the engine torque and the torque assist from the motor. Define the Lagrangian, $L(X)$, for the above optimization problem as follows:

$$L(X) = J(X) + pg(X) \tag{4.32}$$

where p is the Lagrange multiplier. Denote the DP solution by X^*. Then $g(X^*) = 0$, since this constraint was included in DP formulation. The DP solution must satisfy the stationary

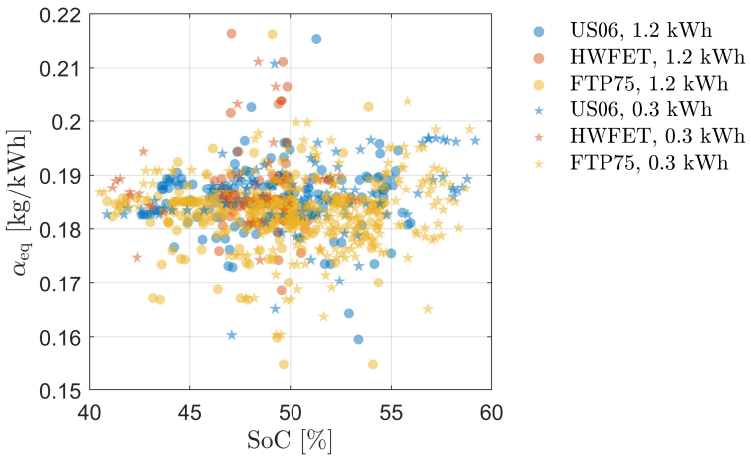

Figure 4.11: The motor equivalent fuel consumption coefficient produced by inverting DP optimization results.

condition, which is:

$$\nabla_X L(X^*) = 0. \tag{4.33}$$

Imposing the above condition and assuming that the variation of motor efficiency with respect to motor torque is small ($\frac{\partial \eta_m}{\partial \tau_m} \approx 0$, since the motor speed is far from zero when the engine is on), the value of α_{eq} is estimated as follows:

$$\alpha_{\text{eq}} = \frac{\eta_m^{\text{sgn}(\text{P}_\text{m})}}{\omega_e} \frac{\partial \dot{m}_f}{\partial \tau_e}. \tag{4.34}$$

For each operating point above NA torque limit of the engine one value of α_{eq} is found from (4.34). Figure 4.11 shows the computed value of α_{eq} from DP results and for two battery sizes and different drive cycles. The units of α_{eq} in this work is [kg/kWh]. The horizontal axis show the battery SoC for each point. As seen the value of α_{eq} varies between 0.15 to 0.22 for different operating points and drive cycles. The average value of α_{eq} is similar for the two batteries, equal to 0.185, which is used for determining the PSS mode under CMR rule. Note that although the value of α_{eq} varies dynamically over the drive cycles, it is shown that a constant value of equivalence factor can produce near optimal results [80]. In addition, the goal of this work was to produce simple yet effective rules for controlling the PSS mode, hence the average value of α_{eq} is used and the capability of the method in producing near optimal solution is shown in following paragraphs.

The rule (4.26) with the found value of α_{eq} is incorporated into the optimization problem (4.19) and solved using DP. Figures 4.12(a) and 4.12(b) show the resulting PSS mode

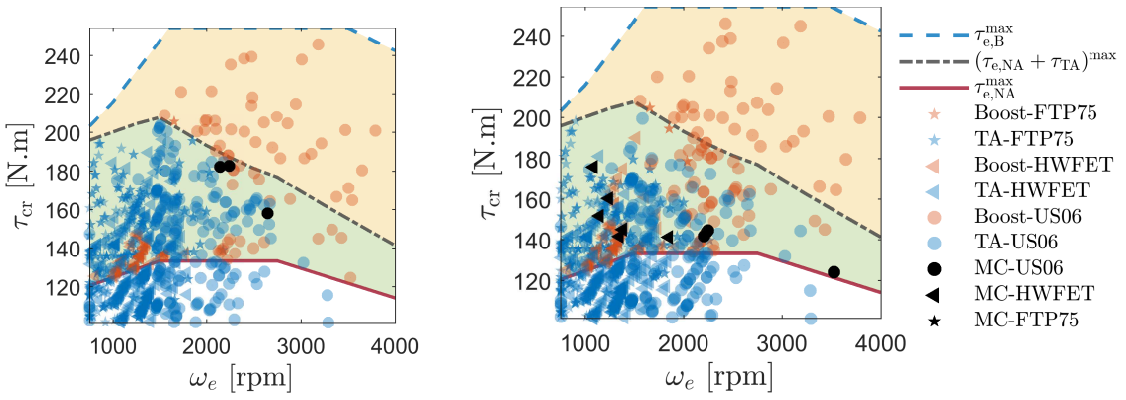

(a) 1.2 kWh battery

(b) 0.3 kWh battery

Figure 4.12: The optimal PSS model under consumption minimization rule with a, (a) 1.2 kWh battery, (b) 0.3 kWh battery. The misclassified points are shown with black markers.

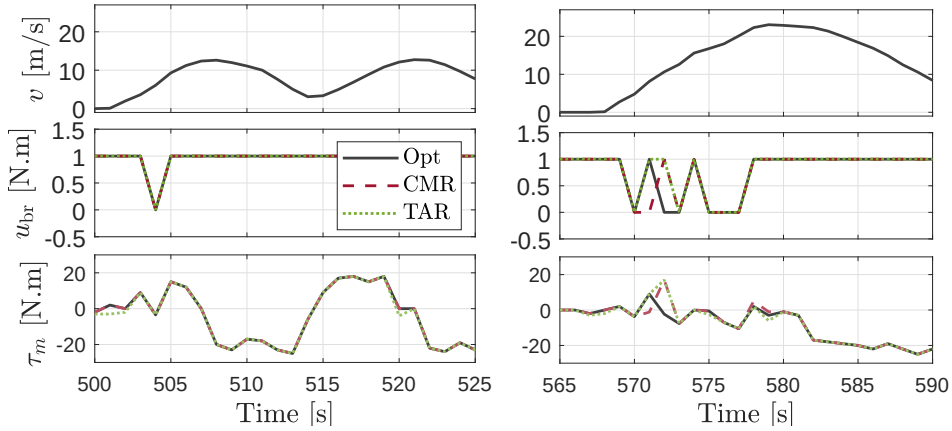

(a)

(b)

Figure 4.13: Comparison between the optimal PSS mode and the operating modes from the CMR and TAR rules for two segments of the US06 cycle. (a) t=500-525 seconds, (b) t=560-590 seconds. The top plot shows the vehicle velocity, the middle plot shows PSS mode from the rules compared to DP optimized mode, and the bottom plot shows the motor torque.

with a 1.2 kWh and a 0.3 kWh battery respectively, over different drive cycles. The misclassified (MC) points are marked with black markers, acquired by point to point comparison. Compared to optimal PSS mode shown in Figures 4.7(a) and 4.7(c) this rule generates the wrong mode for only 3 instances with the 1.2 kWh battery and for 9 instances with the 0.3 kWh battery out of around 500 points where both boosting and torque assist mode are probable. Note that the battery loss is not reflected in the computed value of α_{eq}, yet a single value of α_{eq} produces acceptable results for different battery sizes.

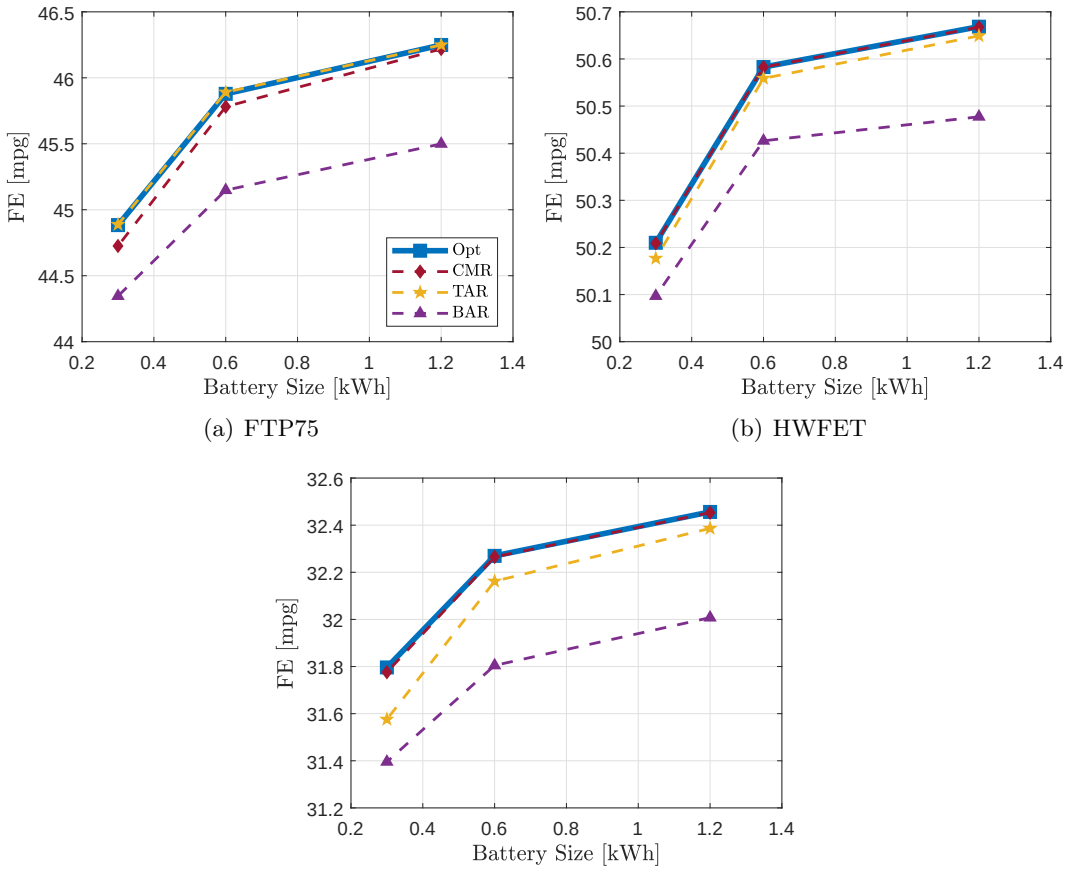

(a) FTP75

(b) HWFET

(c) US06

Figure 4.14: The fuel consumption of the engine with PSS for different battery sizes and PSS mode selection methods, (a) the FTP75 cycle, (b) the HWFET cycle, (c) the US06 cycle.

Figure 4.13 compares the optimal PSS mode to the TAR and CMR strategies for two segments of the US06 cycle. The top plots show the vehicle velocity profile and the bottom plots show the DP generated motor torque trajectory. With the PSS in torque assist mode ($u_{\text{br}} = 1$), positive motor torque stands for supplying torque to the crankshaft and negative torque means generating. Both rules produce correct mode most of the time, except for few instances around t=570 seconds. Also the DP generated motor torque in both cases is close to the case with optimum PSS mode on the bottom plot.

4.5.4 Fuel Consumption Under Rule-based PSS Mode

This section incorporates rules (4.24), (4.25), and (4.26) into the optimal control problem of (4.19), reducing the number of inputs to 3 (gear shift, engine on/off, and commanded torque assist), and compares their DP fuel consumption to each other and the case that PSS mode is an optimization input. Figures 4.14(a), 4.14(b), and 4.14(c) compare the fuel

economy of the vehicle over the FTP75, HWFET, and the US06 cycle under optimized PSS mode and with different battery sizes to FE of the vehicle with the introduced rules for selecting PSS mode. For all the studied cases the FE decreases for a smaller battery size, which is due to the more constrained operation and larger battery losses for a smaller battery. The boost assist rule (BAR, purple line) produces the worst FE numbers, showing that using the PSS merely as a flexible boosting source during large torque demands is not an efficient policy.

The torque assist rule (TAR, yellow line) generates the best FE numbers over the FTP75 and consumption minimization rule (CMR, red) yields better results over the HWFET and the US06 cycle. It can be concluded that both methods yield near optimal FE over the HWFET and the FTP75 but over the US06 TAR FE deviate from the optimal case, specially for smaller batteries. Note that the point by point comparison in Figure 4.12(b) showed that operating mode of the PSS under consumption minimization rule for all points over the FTP75 cycle matches the optimal cases. However, Figure 4.14(a) shows the FC of vehicle under CMR is slightly lower than the optimal case. The reason is that the optimal controller with included CMR produces a marginally different gear shift strategy.

4.6 Fuel Economy Improvement for Naturalistic Drive Cycles

This section extends the FE evaluation of the PSS system to naturalistic cycles beyond the standard EPA cycles studied in the previous section. Real world driving data was previously collected by the University of Michigan Transportation Research Institute as part of an Integrated Vehicle-Based Safety Systems program study. Instrumented MY2006 and MY2007 Honda Accords were driven for daily tasks in southeast Michigan while the vehicle telemetry was recorded. From this data set 67 cycles were selected for analysis of the PSS system. Figure 4.15 shows some key statistics of the cycles studied, the corresponding values for each EPA cycle are also shown as vertical dashed lines. Figure 4.15(a) shows the distribution of cycle length in seconds, which varies from short cycles of less than 500 seconds to long cycles having a duration around 4000 seconds. Figure 4.15(b) shows the distribution of cycle mean velocity, revealing that the majority of the cycles studied have a mean velocity of less than 30 mph, close to the FTP75 cycle mean velocity of 21 mph. Figure 4.15(c) and Figure 4.15(d) show the distribution of cycle maximum velocity and maximum acceleration, showing that most cycles have accelerations faster than the FTP75 and HWFET but smoother than the US06.

The optimal energy management strategy given in equation (4.19) was solved with dynamic programming for both the turbocharged and PSS equipped vehicles over all 67 cycles. Figure 4.16 shows the FE improvement for different cycles versus the cycle average velocity. The corresponding values for the FTP75, HWFET, and the US06 cycles are shown with a star, a diamond and a triangle respectively. These results show that the FE benefit of the PSS system is larger for cycles with a lower average velocity, with the standard EPA

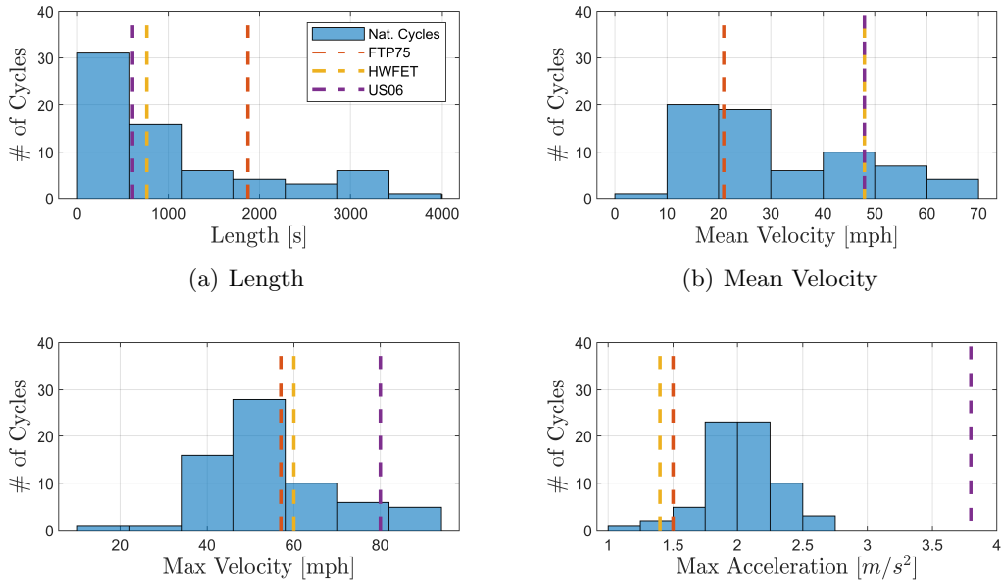

(a) Length

(b) Mean Velocity

(c) Maximum Velocity

(d) Maximum Acceleration

Figure 4.15: The statistics of the studied naturalistic drive cycles and comparison to EPA standard cycles, (a) time length, (b) mean velocity, (c) maximum velocity, (d) maximum acceleration.

cycles follow the same trend. This finding is not surprising given that a cycle with lower average velocity most likely has more braking and stopping instances, during which the PSS system can effectively improve the fuel economy. Figure 4.17 shows few examples of the velocity profiles of the cycles studied, with the improvement in FE provided by the PSS in the caption.

4.7 Summary

This chapter formulated an optimization problem for energy management of two mild hybrid systems both capable of boosting and parallel hybrid operation, one with a single motor (PSS), and the other with two separate motors for boosting and torque assist (eSC-SGM). The optimization cost function for the PSS engine penalizes the fuel flow rate, gear shifts, engine cranking for start/stop, and the PSS mode to keep the brake locked as default. The modeled states are the battery state of charge, gear number, and engine on/off state. The optimization inputs include the gear shift command, the engine start/stop, the PSS mode, and the motor torque when the PSS is in torque assist mode. Input dependent constraints were used to model the switching system structure in different modes. The optimal control problem was discretized and solved using dynamic programming.

It was shown that both mild hybrid systems are capable of improving the vehicle fuel economy on combined cycle by 20.7%, which is around 75% of a full HEV benefit. While, on

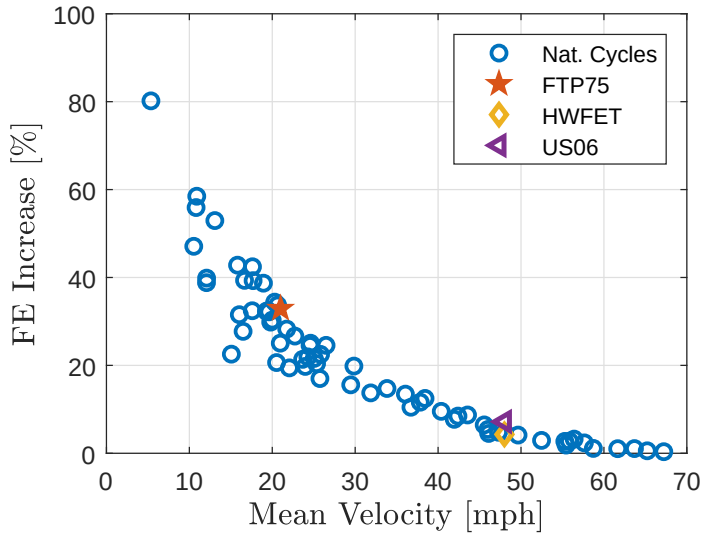

Figure 4.16: The vehicle with PSS fuel economy improvement compared to the baseline turbocharged engine for the studied naturalistic drive cycles and standard cycles, plotted against the drive cycle mean velocity.

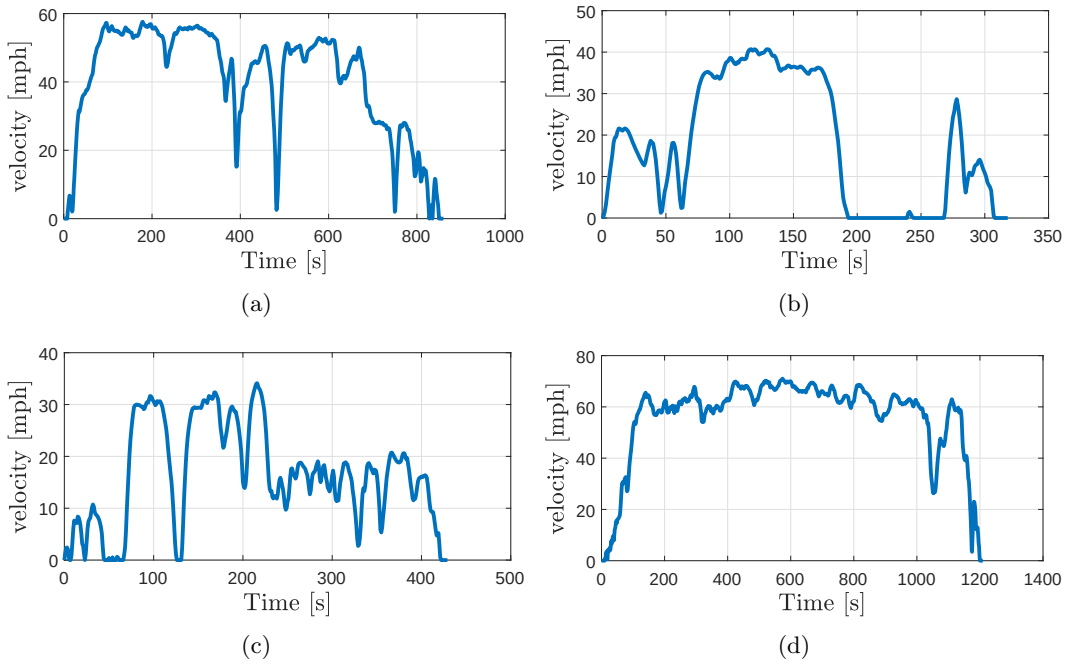

Figure 4.17: Example of the naturalistic drive cycles studied. The fuel economy improvement of the vehicle with the PSS compared to the turbocharged engine for each case is, (a) ΔFE = 9.5%, (b) ΔFE = 42.4%, (c) ΔFE = 27.7%, (d) ΔFE = 2.8%.

the US06, which is a more aggressive cycle, the mild hybrids can enhance the fuel economy only by 7-8%, which is 40-50% of the full hybrid fuel economy gain. The results revealed that the optimal controller for the PSS engine often adopts torque assist over supercharging

mode when the torque demand can be met with either mode, but the occasions of using the supercharger increases for smaller battery sizes. The fuel economy benefit of the PSS system for some real world cycles was studied following the same DP optimization framework. It was shown that the PSS FE gain is largest for cycles with lower average velocities, similar to the FTP75 cycle, because they include more braking and stopping instances.

The DP solution showed that the additional flexibility of eSC-SGM, from dual motors, is only useful on the US06, where it gives 1.3% more fuel economy benefit compared to the PSS. In addition, the optimal controller for the two motor eSC-SGM uses both the electric supercharger and torque assist simultaneously to meet high torque demands, and the supercharging share increases for a smaller battery or a more efficient supercharger. Furthermore, the results showed that it is not a fuel optimal policy to supercharge the engine and generate electric power from the crankshaft in the same time in this system and generation from the crankshaft is only fuel economic in non-boosted points.

Finally, two causally implementable rules, one that uses the supercharger only when necessary and the other that selects the PSS mode based on the equivalent minimum consumed fuel were proposed and integrated into the optimization problem. It was shown that these rules can produce results very close to optimal fuel economy for different battery sizes and drive cycles.

CHAPTER V

Online Energy Management for a Power Split Supercharger

This chapter focuses on designing an online energy management for a vehicle equipped with a PSS. Many different controllers are developed for energy management of HEVs, which fall into the two main categories of rule-based approaches and optimization-based approaches [30]. Rule-based methods are static controllers and can be implemented in real time. These rules are determined offline based on heuristics or approximations to optimization results. These techniques do not use the knowledge of the drive cycle or a traffic preview. Thermostatic control, which turns the engine on and off based on the battery state of charge, is an example of rule-based control for a series HEV. Load leveling, which uses only the motor at low load, the engine at medium load and both at high load, is an example of a rule-based approach for a parallel HEV. These controllers are based on simple concepts and easily implementable. However, they do not exploit the full potential of the system for fuel consumption reduction and are not reusable for a different objective or powertrain configuration.

Optimization-based methods on the other hand, use physics-based modeling and optimization techniques to minimize a cost function that can include different performance metrics such as fuel consumption or emissions. The objective cost can be minimized instantaneously, like the equivalent consumption minimization method [79], or over some receding horizon, such as with model predictive control [78], or over the full driving profile, as in dynamic programming [31, 74].

The global fuel consumption minimization for a hybrid electric vehicle equipped with a power split supercharger under a charge sustaining constraint was previously formulated and solved using DP in Chapter IV. This chapter presents an Equivalent Consumption Minimization Strategy (ECMS) that minimizes the instantaneous fuel consumption of the engine and the battery for a vehicle equipped with a PSS. The DP results from the previous study are revisited throughout this work to compare against the ECMS results and to infer the electric energy equivalence factor. The global fuel consumption minimization problem is shortly described and then the ECMS is formulated. The equivalence factor for the ECMS is computed from the DP results through inverse optimization. The implementation of

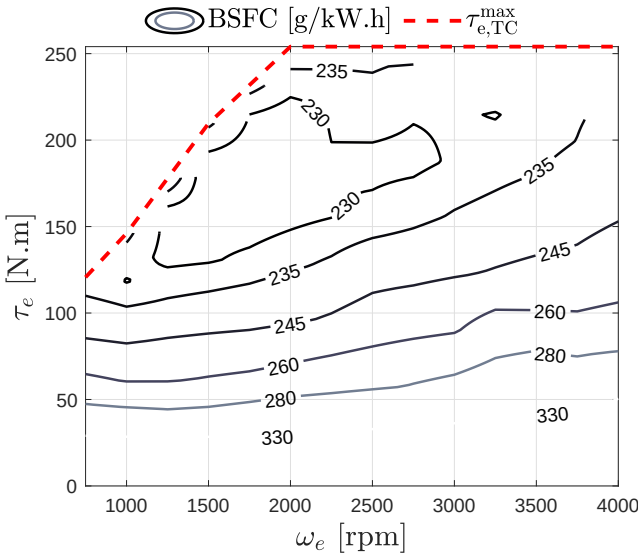

Figure 5.1: Brake specific fuel consumption for baseline turbocharged engine. The maximum engine produced torque, $\tau_{e,\mathrm{TC}}^{\max}$, is also shown.

the ECMS is explained and the drive cycle simulation results are presented and compared against the DP results. The trajectories from the simulations are supplied to the engine dynamometer setup to experimentally verify the fuel economy gains. Later, an adaptive ECMS strategy is introduced and its performance is compared against the ECMS controller.

5.1 Utilized Hardware

The baseline engine is a 1.6 liter, 4 cylinder four stroke gasoline fueled turbocharged SIDI engine, patterned off a Ford EcoBoost engine. The PSS is coupled with the engine after removing the turbocharger.

5.2 Vehicle and Powertrain Model

5.2.1 Engine Model

5.2.1.1 Fuel Consumption Map

The GT-Power engine model, introduce and validated in Section 2.6 was used to develop fuel consumption maps of both the turbocharged engine and the engine with PSS. Figure 5.1 shows the baseline turbocharged engine BSFC map, along with the engine maximum produced torque, $\tau_{e,\mathrm{TC}}^{\max}$. Figure 5.2 shows the BSFC map for the engine with PSS along with the engine torque limit in boosting mode, $\tau_{e,B}^{\max}$, the engine torque limit when the supercharger is bypassed, $\tau_{e,\mathrm{NA}}^{\max}$ and the powertrain maximum torque in torque assist mode, $(\tau_{e,\mathrm{NA}} + \tau_{\mathrm{TA}})^{\max}$.

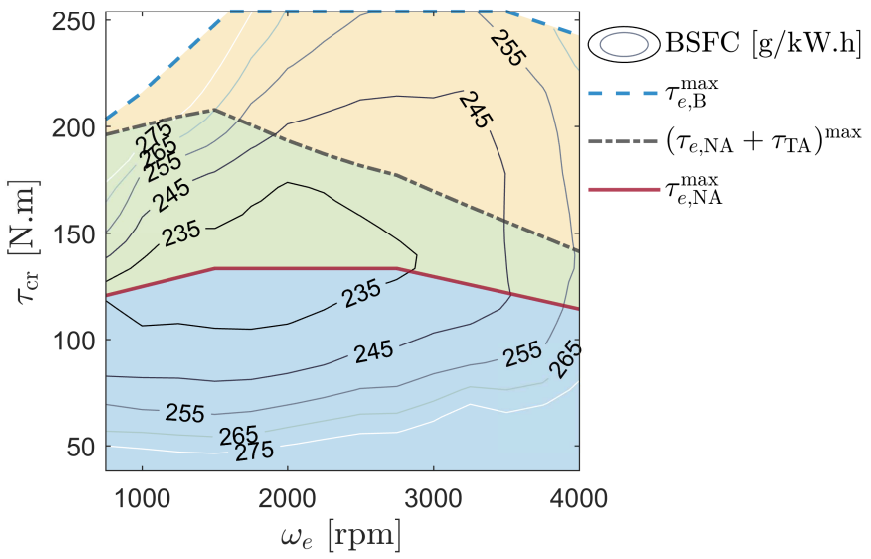

Figure 5.2: Brake specific fuel consumption for engine with the power split supercharger along with the maximum engine torque at boosting mode, $\tau_{e,\mathrm{B}}^{\max}$, the powertrain maximum torque at torque assist mode, $(\tau_{e,\mathrm{NA}} + \tau_{\mathrm{TA}})^{\max}$, and the naturally aspirated engine maximum torque, $\tau_{e,\mathrm{NA}}^{\max}$.

5.2.1.2 Torque Dynamics

The mean value engine model introduced and validated in Section 2.2 is used to capture the full engine air path dynamics. The modeled states were the pressure state inside different air path volumes, actuator dynamics, the turbocharger shaft dynamics (for the TC engine) and the PSS dynamics (for the engine with PSS). The 4-cylinders, compressor, turbine, charge air coolers, the supercharger, and motor were modeled as quasi steady components. A compressible turbulent flow equation was used to model the flow through the valves, including the throttle, wastegate, and the supercharger bypass valve. The induction to power and induction to exhaust delays were used to model the engine reciprocating behavior. An example of the model performance in a super-turbo configuration was presented in Chapter III.

5.2.2 Vehicle Model

The modeled vehicle is a MY2015 Ford Escape with 6 speed automatic transmission. The drivetrain model includes a transmission, a friction clutch in parallel with a torque converter and crankshaft dynamics. The individual models of each component along with the transmission and clutch control strategy were described in detail Section 2.7. The driver model is a Proportional+Integral (PI) controller that switches gains based on a 1 second preview of the vehicle acceleration and the tracking error.

5.3 Energy Management System

5.3.1 Global Fuel Consumption Minimization

The global fuel consumption minimization problem for a vehicle equipped with a PSS was formulated and solved using DP in Chapter IV. In this chapter the DP results are used to gain insight and compared to the instantaneous consumption minimization problem. A brief summary of the DP problem is presented in the following discussion. The cost function in the global fuel consumption minimization problem penalizes the fuel flow rate, the gear shifts, the engine cranking (for start/stop) and the PSS mode as follows:

$$\min\Bigg\{\sum_{k=1}^{N}\Bigg(\dot{m}_f(k)T_s+\alpha|n_g(k)-n_g(k-1)| \\ +\beta\big(\max(x_e(k)-x_e(k-1),0)\big)+\lambda\big(1-u_{\mathrm{br}}(k)\big)\Bigg)\Bigg\} \tag{5.1}$$

in which the problem horizon, N, is the full drive cycle and T_s is the problem sampling time equal to 1 second. The problem inputs are the commanded torque assist from the electric motor, gear shift command, the PSS mode, and the engine on/off command. The modeled system states include the battery state of charge, the gear number, and the engine on/off state. This problem was solved using a MATLAB based dynamic programming function. Full details are provided in Chapter IV.

5.3.2 Equivalent Consumption Minimization

The equivalent consumption minimization proposed by Paganelli [79, 85] minimizes the instantaneous sum of the engine and the motor fuel flow rate by using a factor to convert the electric energy consumption to an equivalent fuel flow rate. The motor torque in ECMS is computed as follows:

$$\tau_m=\underset{\tau_m}{\operatorname{argmin}}\big(\dot{m}_f(\tau_e,\omega_e)+\alpha_{\mathrm{eq}}P_m(\tau_m,\omega_m)\big) \tag{5.2}$$

where τ_m is the motor torque, ω_m is the motor speed, τ_e is the engine torque, ω_e is the engine speed and α_{eq} is the equivalence factor. The energy management system of an engine with a PSS is different from a conventional HEV because it has to decide on the PSS mode first and if the torque assist mode is selected then the EMS has to determine the optimum motor torque to minimize the powertrain fuel consumption. Note that the motor torque is an optimization parameter in torque assist mode but not in the boosting mode, during which the motor controls the boost pressure and hence the engine torque.

When the requested crankshaft torque, τ_{cr}^{d}, is less than the naturally aspirated torque limit of the engine, $\tau_{e,\mathrm{NA}}^{\max}$, the blue area in Figure 5.2, it is fuel optimal to brake and bypass

the supercharger, hence the PSS should be in torque assist mode. On the other hand, when the requested torque is larger than $\tau_{e,\mathrm{NA}}^{\max}$ plus the maximum torque assist from the motor on the crankshaft, $(\tau_{e,\mathrm{NA}} + \tau_{\mathrm{TA}})^{\max}$, the yellow area in Figure 5.2 the powertrain can only supply the requested torque through supercharging, hence the PSS must be in boosting mode. Finally, when the requested torque is larger than $\tau_{e,\mathrm{NA}}^{\max}$ and smaller than the powertrain torque limit in torque assist mode, green area in Figure 5.2, the requested torque can be realized through either mode. In this work a consumption minimization rule that selects the PSS mode for minimizing the sum of the engine and the motor fuel flow rate is introduced:

$$u_{\mathrm{br}}^{\mathrm{CMR}} = \begin{cases} 0 & \text{if} \quad \tau_{\mathrm{cr}}^{d} > (\tau_{\mathrm{TA}} + \tau_{e,\mathrm{NA}})^{\max} \\ 1 & \text{if} \quad \tau_{\mathrm{cr}}^{d} \leq \tau_{e,\mathrm{NA}}^{\max} \\ \underset{u_{\mathrm{br}}=0,1}{\operatorname{argmin}}(\dot{m}_{f,\mathrm{eq}}) & \text{otherwise} \end{cases} \tag{5.3}$$

where $u_{\mathrm{br}}^{\mathrm{CMR}}$ is the PSS mode for consumption minimization. This rule was introduced and incorporated into DP optimal control problem in Chapter IV, however it is repeated here because unlike Chapter IV, here the rule is used in forward simulation on a detailed vehicle and engine model and its generated results are later tested on the engine dynamometer experimental setup. The equivalent fuel flow rate of the engine and motor, $\dot{m}_{f,\mathrm{eq}}$, computed for each mode:

- Boosting mode ($u_{\mathrm{br}} = 0$):

$$\dot{m}_{f,\mathrm{eq}} = \dot{m}_f(\tau_e^d, \omega_e) + \alpha_{\mathrm{eq}} P_m(\tau_e^d, \omega_e) \tag{5.4a}$$

$$\tau_e^d = \tau_{\mathrm{cr}}^d \tag{5.4b}$$

- Torque assist mode ($u_{\mathrm{br}} = 1$):

$$\dot{m}_{f,\mathrm{eq}} = \min_{\tau_{\mathrm{m}}^d} \left(\dot{m}_f(\tau_e^d, \omega_e) + \alpha_{\mathrm{eq}} P_m(\tau_{\mathrm{m}}^d, \omega_m) \right) \tag{5.5a}$$

$$\tau_e^d = \tau_{\mathrm{cr}}^d - \tau_{\mathrm{TA}}^d \tag{5.5b}$$

$$\tau_m^d = \frac{g_R}{n_{\mathrm{im}} n_{\mathrm{ri}} (g_S + g_R)} \tau_{\mathrm{TA}}^d \tag{5.5c}$$

where τ_{TA} is the torque assist from the motor on the crankshaft related to the motor torque through (5.5c), g_S is the sun gear teeth number, g_R is the ring gear teeth number, n_{im} is the idler to motor gear ratio and n_{ri} is the ring to idler gear ratio. The superscript d refers to the demanded or commanded values.

When in boosting mode, the engine has to supply the entire requested torque, (5.4b). In this mode the planetary gear set and the motor decouple the supercharger produced boost pressure from the engine operating speed. The engine losses are minimized by utilizing

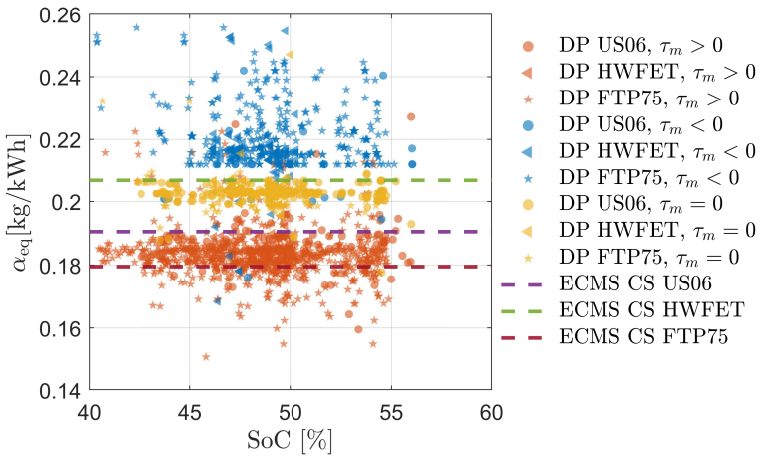

Figure 5.3: The ECMS equivalence factor produced by inverting DP optimization results along with the used equivalence factor for charger sustaining (CS) condition in full vehicle simulation.

Wide Open Throttle (WOT) in these operating points. Employing a WOT strategy, the motor power for supercharging is a function of the engine operating point during steady state, shown in Figure 4.4(c). This steady state map is used to compute the equivalent fuel consumption of the engine in boosting mode.

During torque assist mode, the motor supplies part of the torque demand, (5.5b), and for a given equivalence factor, the motor torque should be determined to minimize the equivalent fuel flow rate of the engine and the motor, similar to a regular ECMS problem. The only remaining parameter to be determined for the online energy management system is the equivalence factor.

5.3.3 ECMS Equivalence Factor from DP Results

The inverse optimization problem for inferring the ECMS equivalence factor from the DP results was introduced in Section 4.5.3 and solved over the operating points that the energy management system had to use torque assist or boosting to meet the driver torque demand (The green area in Figure 5.2). The equivalence factor in this method is computed as,

$$\alpha_{\text{eq}} = \frac{\eta_m^{\text{sgn}(\text{P}_\text{m})}}{\omega_e} \frac{\partial \dot{m}_f}{\partial \tau_e}. \tag{5.6}$$

Here the equivalence factor is computed for a larger set of operating points with positive torque demand of less than the powertrain maximum torque in torque assist mode, $(\tau_{e,\text{NA}} + \tau_{\text{TA}})^{\max}$. The resulting α_{eq} is plotted against the battery SoC at each operating point in Figure 5.3 for standard EPA drive cycles. The blue markers represent instances that the

PSS motor is generating, the red markers represent points where the motor supplies energy to the crankshaft, while the yellow markers are the points that the motor torque is zero. The data points on the US06, HWFET and the FTP75 cycles are indicated by circle, triangle and star markers. The value of the equivalence factor varies mainly between 0.17 to 0.22, with the value highest for generating (blue markers) and lowest for supplying torque to the crankshaft (red markers). There is no apparent relationship between the computed equivalence factor and the instantaneous battery state of charge. The reason for this is that DP considers the full problem horizon for minimizing the fuel consumption, thus it makes sense that the computed equivalence factor is not directly related to the instantaneous SoC.

It is shown that a single equivalence factor can produce near optimal fuel economy results over a drive cycle [80]. Hence, in the dynamic drive cycle simulations presented later the equivalence factor is fixed over the cycle. Meanwhile, the next section presents the ECMS solution for the optimal PSS mode and motor torque in torque assist mode for different values of the equivalence factor, which also produces charge sustaining solutions over the standard EPA drive cycles.

5.3.4 ECMS Solution under Charge Sustaining Conditions

The optimum PSS mode and motor torque in torque assist mode can be calculated offline for various crankshaft speeds, torques, and equivalence factors and stored in look up tables [81]. Figures 5.4(a), 5.4(b) and 5.4(c) show the PSS mode from (5.2) with three different values of the equivalence factor, $\alpha_{\text{eq}} = 0.179$, $\alpha_{\text{eq}} = 0.207$, $\alpha_{\text{eq}} = 0.191$, which generate charge sustaining results over the FTP75, HWFET and the US06 cycles, respectively. These values are also represented on Figure 5.3 for comparison to the equivalence factor inferred from the DP solution.

In Figures 5.4(a), 5.4(b) and 5.4(c) the blue color stands for boosting mode and the red color represents the torque assist mode. The operating points from the dynamic programming results during each cycle are also plotted on top of the ECMS produced mode for comparison. In the area that the requested torque can be supplied through both modes, torque assist mode is mostly the optimal choice, except for high engine speeds (>3000 rpm) or the points close to the maximum powertrain torque in torque assist mode, $(\tau_{e,\text{NA}} + \tau_{\text{TA}})^{\max}$. On the HWFET and US06 cycles, boosting is also fuel optimal for operating points close to the naturally aspirated torque limit of the engine. The ECMS solution for the PSS mode is in agreement with the DP results found in the prior work everywhere except for a small region on the US06 cycle around 2500 rpm engine speed and 150 N.m torque.

Figures 5.5(a), 5.5(b), and 5.5(c) show the ECMS computed motor torque (with equivalence factors mentioned above) for the FTP75, HWFET and the US06 cycles, along with the powertrain operating points from DP, shown with star markers and colored based on the motor torque sign, where blue signifies negative motor torque (generating) and red markers stand for a positive motor torque (supplying) while yellow means zero motor torque. The

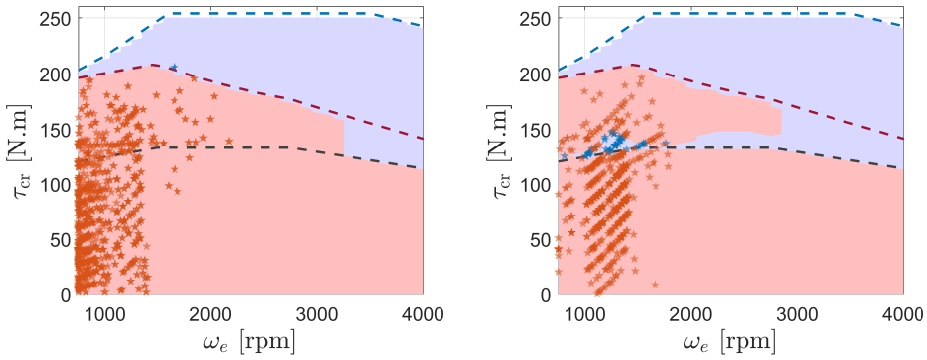

(a) PSS Mode for FTP75 (α_{eq}=0.179)

(b) PSS Mode for HWFET (α_{eq}=0.207)

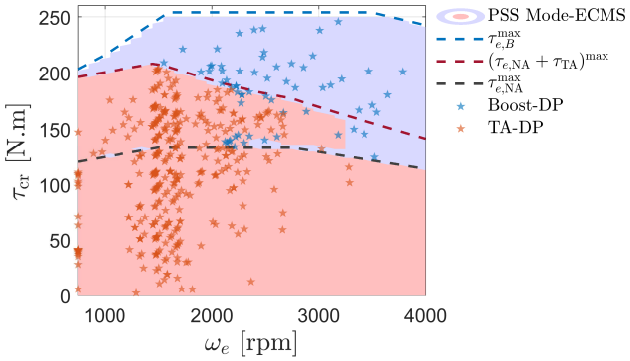

(c) PSS Mode for US06 (α_{eq}=0.191)

Figure 5.4: The optimal PSS model under the consumption minimization rule and comparison to DP results over, (a) the FTP75, (b) the HWFET, (c) the US06 cycle. The blue color stands for the boosting mode and the red color shows torque assist mode.

ECMS results show that over all cycles, the electric machine should generate at low loads to prevent the engine working at a low efficiency, consistent with the DP results. At medium torques, the motor should mostly supply torque to the crankshaft over the FTP75 and US06 but not over the HWFET. This result is in agreement with the DP solution over the FTP75 and the HWFET. However, on the US06 the ECMS shows that the motor should supply a small amount of torque to the crankshaft, while the motor torque is mostly zero at medium load points in the DP solution.

Note that the required equivalence factor for charge sustaining operation is smallest over the FTP75 cycle due to the higher availability of electric energy from regenerative braking on this cycle. Likewise, the equivalence factor is the highest on the HWFET cycle, which does not include many braking instances.

Analyzing the results shown in Figure 5.4, the PSS operating mode selection can be further simplified to use the boosting mode when the torque demand is larger than the

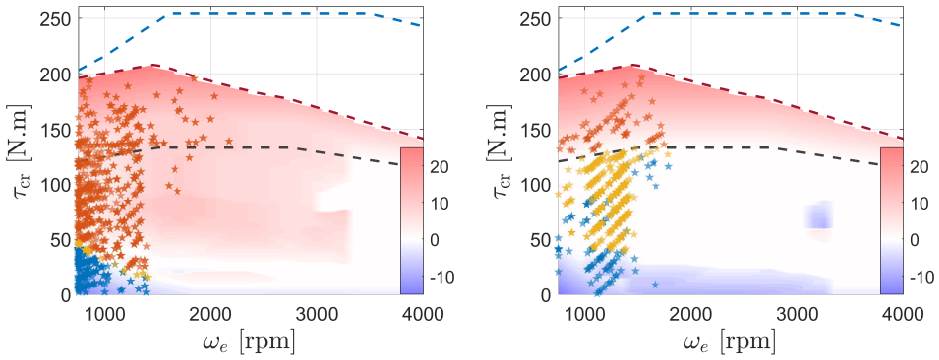

(a) Torque assist for FTP75 (α_{eq}=0.179) (b) Torque assist for HWFET (α_{eq}=0.207)

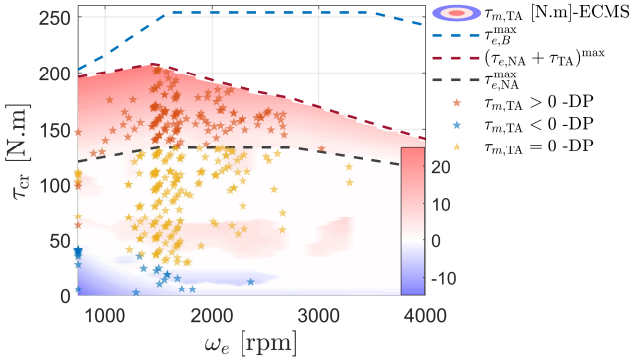

(c) Torque assist for US06 (α_{eq}=0.191)

Figure 5.5: The motor torque during torque assist mode from ECMS and comparison to DP results over (a) the FTP75, (b) the HWFET, (c) the US06 cycle.

maximum powertrain torque in torque assist mode (above the green area in Figure 5.2),

$$u_{br}^{TAR} = \begin{cases} 1 & \text{if} \quad \tau_{cr}^{d} > (\tau_{TA} + \tau_{e,NA})^{max} \\ 0 & \text{otherwise} \end{cases} \tag{5.7}$$

where u_{br}^{TAR} is the PSS mode from torque assist rule. Note that it was shown in Chapter IV that for smaller battery sizes with lower electric energy availability and higher battery loss, supercharging is the fuel optimal strategy for a larger range of operating points. In this work the PSS mode selection based on both the consumption minimization rule and the torque assist rule are studied while the effect of battery size on the vehicle fuel consumption and the effectiveness of these rules is left for future development.

5.4 ECMS Implementation for Full Drive Cycle Simulation

The implementation of hybrid capabilities of the PSS system on the vehicle model for full drive cycle simulation is described in this section. The PSS permits power split (between the

engine and motor), regenerative braking and start/stop. In order to implement regenerative braking and power split, the torque demand on the crankshaft, τ_{cr}^{d}, has to be computed first.

5.4.1 Torque Demand on Crankshaft

The requested tractive torque, τ_{trc}^{d}, when the accelerator pedal is active is linearly mapped to the pedal position:

$$\tau_{\mathrm{trc}}^{d} = u_{\mathrm{acc}}(\tau_{e,\mathrm{B}}^{\max} - \tau_{e}^{\min}) + \tau_{e}^{\min} \tag{5.8}$$

where u_{acc} is the accelerator pedal position, $\tau_{e}^{\min}$ is the minimum engine torque and $\tau_{e,\mathrm{B}}^{\max}$ is from Figure 5.2. The requested braking torque on the gearbox inlet shaft, τ_{brk}^{d}, is computed with:

$$\tau_{\mathrm{brk}}^{d} = \frac{u_{\mathrm{brk}}\tau_{\mathrm{brk}}^{\max}}{\gamma} \tag{5.9}$$

where u_{brk} is the brake pedal position, $\tau_{\mathrm{brk}}^{\max}$ is the maximum braking torque on the wheels and γ is the gear ratio in the gearbox. In a vehicle with automatic transmission when the vehicle is stopped and at low vehicle speed, the torque converter unlocks and the engine has to supply some torque to maintain the idling speed. This minimum torque can be computed from the torque converter K-factor, K, and Torque Ratio, TR, which are functions of turbine to pump speed ratio, SR,

$$\mathrm{SR} = \frac{\omega_{\mathrm{tct}}}{\omega_{\mathrm{tcp}}} \tag{5.10a}$$

$$\tau_{\mathrm{tcp}} = \Big(\frac{\omega_{\mathrm{tcp}}}{K}\Big)^{2} \tag{5.10b}$$

$$\tau_{\mathrm{tct}} = \tau_{\mathrm{tcp}} \times \mathrm{TR} \tag{5.10c}$$

where ω_{tct} is the torque converter turbine speed, τ_{tct} is the turbine torque, τ_{tcp} is the pump torque, and ω_{tcp} is the pump speed. Assuming that ω_{tcp} is equal to the engine idling speed when the torque converter unlocks, the minimum torque on the crankshaft when the turbine speed drops to less than engine idling speed can be computed as a function of turbine speed, $\tau_{\mathrm{tcp}}^{*}(\omega_{\mathrm{tct}})$. Accordingly, the minimum torque on the crankshaft, $\tau_{\mathrm{cr}}^{\min}$, is computed by:

$$\tau_{\mathrm{cr}}^{\min} = \begin{cases} \tau_{\mathrm{tcp}}^{*}(\omega_{\mathrm{tct}}) & \text{if} \quad \omega_{\mathrm{tct}} \le \omega_{e,\mathrm{idle}} \\ -\infty & \text{otherwise.} \end{cases} \tag{5.11}$$

The requested torque on the crankshaft is:

$$\tau_{\mathrm{cr}}^{d} = \begin{cases} \max(\tau_{\mathrm{trc}}^{d}, \tau_{\mathrm{cr}}^{\min}) & \text{if} \quad u_{\mathrm{acc}} \ge 0 \\ \max(\tau_{\mathrm{brk}}^{d}, \tau_{\mathrm{cr}}^{\min}) & \text{if} \quad u_{\mathrm{brk}} > 0. \end{cases} \tag{5.12}$$

This equation imposes some positive torque demand on the crankshaft at low vehicle speed to maintain the engine idling speed and it disables regenerative braking under these conditions.

5.4.2 Traction

The PSS optimal mode during traction ($\tau_{\mathrm{cr}}^d > 0$) and the optimum motor torque in torque assist mode are computed offline and stored in look up tables based on the requested crank torque and the engine speed:

$$u_{\mathrm{br}}^d = \Gamma(\tau_{\mathrm{cr}}^d, \omega_e) \tag{5.13}$$

$$\tau_m^d = \Lambda(\tau_{\mathrm{cr}}^d, \omega_e) \tag{5.14}$$

in which u_{br}^d is the commanded PSS mode and τ_m^d is the motor torque demand. The desired engine torque is:

$$\tau_e^d = \begin{cases} \tau_{\mathrm{cr}}^d & \text{if} \quad u_{\mathrm{br}}^d = 0 \\ \tau_{\mathrm{cr}}^d - \tau_m^d \frac{(g_R+g_S)n_{\mathrm{im}}n_{\mathrm{ri}}}{g_R} & \text{if} \quad u_{\mathrm{br}}^d = 1. \end{cases} \tag{5.15}$$

Finally the desired intake manifold pressure is computed from the engine speed and the desired engine torque

$$p_{\mathrm{im}}^d = \Xi(\tau_e^d, \omega_e). \tag{5.16}$$

When the desired manifold pressure is less than the ambient pressure the supercharger is bypassed and the intake throttle is used to control the intake manifold pressure, while when the desired intake manifold pressure is higher than the ambient pressure the throttle is wide open and the supercharger controls the intake manifold pressure.

5.4.3 Regenerative Braking

Regenerative braking is only feasible when the torque demand on the crankshaft is negative ($\tau_{cr}^d < 0$) and the torque converter is locked. Due to practical reasons the torque converter is unlocked at a slightly higher speed than the engine idling speed[1]. The motor torque during regenerative braking is computed by:

$$\tau_m^d = \max(\tau_{cr}^d \frac{g_R}{(g_R + g_S)n_{\mathrm{im}}n_{\mathrm{ri}}}, \tau_m^{\min}) \times u_c \tag{5.17}$$

where $u_c = 1$ stands for the locked torque converter and $u_c = 0$ means an unlocked torque converter, while $\tau_m^{\min}$ is the minimum motor torque. The PSS mode is set to torque assist mode during braking. Note that (5.17) is the solution to (5.2).

[1]The engine idling speed is 750 rpm and the torque converter unlocks at 900 rpm in the vehicle model.

Table 5.1: Drive cycle simulation results for Ford Escape. The numbers in parenthesis show the relative fuel economy improvement compared to the turbocharged engine for that model type.

Powertrain	Model Type	Energy Management	FTP75 Cycle FE [mpg]	HWFET Cycle FE [mpg]	US06 Cycle FE [mpg]	Combined Cycle FE [mpg]
Turbocharged	Simple	DP	34.79	48.57	30.29	39.88
Engine + PSS	Simple	DP	46.25 (32.9%)	50.67 (4.3%)	32.46 (7.2%)	48.14 (20.7%)
Turbocharged	Full	-	33.86	47.98	30.22	39.03
Engine + PSS	Full	CMR/ECMS	44.54 (31.5%)	49.90 (4.0%)	31.95 (5.7%)	46.80 (19.9%)
Engine + PSS	Full	TAR/ECMS	44.56 (31.6%)	49.87 (3.9%)	32.00 (5.9%)	46.80 (19.9%)

5.4.4 Engine Start/Stop

The engine is turned off when the vehicle speed, v, is less than some threshold, v_{th}, close to zero and the accelerator pedal is not depressed. Otherwise the engine is turned on,

$$u_e = \begin{cases} 0 & \text{if} \quad u_{\text{acc}} = 0, v \leq v_{\text{th}} \\ 1 & \text{otherwise} \end{cases} \tag{5.18}$$

in which u_e is the engine on/off command. The engine torque, motor torque, engine speed and the fuel flow rate are set equal to zero when the engine is turned off and it is assumed the engine turns on and reaches the idling condition 250 ms after the start command is issued. A fuel penalty of 0.28 grams is assumed for each engine cranking and a minimum fuel flow rate of 1 kg/h is assumed when the engine is turned on.

5.5 Drive Cycle Simulation Results

This section presents the drive cycle simulation results with ECMS for controlling the PSS mode and the motor torque, with the equivalence factor selected for charge sustaining operation. Table 5.1 presents the fuel economy predictions in miles per gallon (mpg) for the baseline turbocharged engine and the engine with the power split supercharger over standard EPA drive cycles. The first two rows show the dynamic programming fuel economy predictions from Chapter IV and the bottom three rows show the new full vehicle simulations. The numbers in parenthesis show the relative fuel economy improvement of each case compared to the baseline turbocharged engine for that model. The dynamic programming solution employes backward simulation to calculate the crankshaft torque from the drive cycle speed profiles and uses static maps to model the engine, while the full vehicle simulation includes the vehicle, driveline and engine torque dynamics with low-level controllers for each component and a driver model. The DP results for the TC engine include optimized gear numbers. The gear shift strategy for the TC engine and the engine with PSS is similar in the full vehicle simulations. There are two full vehicle simulation cases with ECMS in last two rows of Table 5.1, one of which uses the Consumption Minimization Rule (CMR), from (5.3), for PSS mode selection and the other uses the Torque Assist Rule

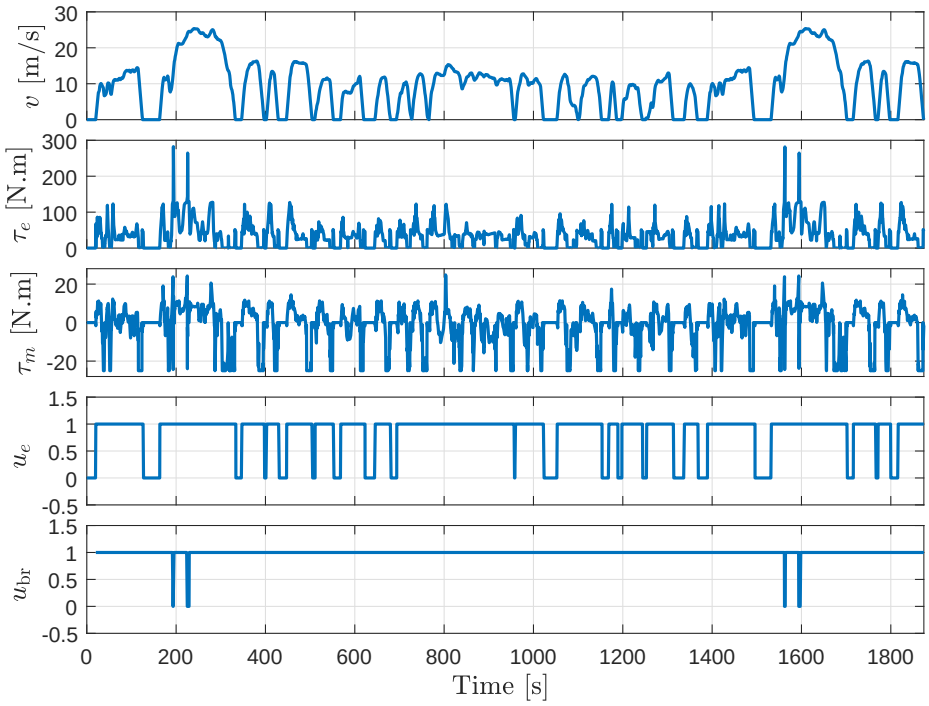

Figure 5.6: The optimal trajectories generated by ECMS over the FTP75 drive cycle. Respectively from top, vehicle velocity, engine torque, motor torque, engine on/off command and the PSS mode.

(TAR), from (5.7), while both cases use ECMS for commanding the motor torque in torque assist mode.

The DP solution showed that the engine with the PSS produces 32.9%, 4.3%, and 7.2% greater FE compared to the TC engine over the FTP75, HWFET and the US06 cycles, respectively, and 20.7% improvement over the combined cycle. The combined cycle FE is computed with allocating weights of 0.55 and 0.45 to FTP75 and HWFET cycles fuel consumption, respectively [83]. The full vehicle simulation with the ECMS and CMR generates 31.5%, 4.0% and 5.7% FE improvements over the FTP75, HWFET, and the US06 cycles and 19.9% over the combined cycle. In terms of the relative fuel economy improvement, ECMS gives more than 90% of the DP predicted FE improvement on the FTP75 and HWFET cycles and 80% of the DP predicted FE gain on the US06 cycle. The reason for this difference lies in the highly transient velocity profile of the US06 cycle, because ECMS uses only static maps in its computations. The ECMS with TAR for PSS mode selection produces similar fuel economy predictions, confirming the possibility of further control design simplification for the PSS mode selection.

Figure 5.6 shows the optimal trajectories generated by the ECMS with CMR over the FTP75 drive cycle. The top subplot shows the cycle velocity profile. The second subplot shows the engine torque, which is mostly less than the naturally aspirated torque limit of the engine (shown on Figure 5.2), except for four peaks, where a large torque is requested.

The third subplot shows the motor torque. The motor torque is negative when the vehicle is decelerating (decreasing speed on the first subplot), meaning that the motor is recouping part of the vehicle kinetic energy and it is supplying the recovered energy back to the crankshaft (positive torque segment) during accelerations. When the engine is turned off, both the motor torque and the engine torque are zero, shown in the fourth subplot, where $u_e = 1$ means that the engine is turned on and $u_e = 0$ stands for engine turned off. The bottom subplot shows the commanded PSS mode, u_{br}. During the large torque requests the PSS switches to boosting mode, $u_{\text{br}} = 0$, corresponding to the peaks in engine torque plot on the second subplot.

Finally, Figure 5.7 compares the battery state of charge variation during the FTP75, HWFET and the US06 cycles from CMR/ECMS to the SoC trajectory from the dynamic programming results. The charge sustainability condition is imposed for both the ECMS and DP solutions. The SoC variation shows the instances of electric energy harvesting and consumption. The trajectories are close for the DP and ECMS solutions, confirming that the suboptimal solution found via ECMS acts close to the global optimal solution.

5.6 Experimental Drive Cycle Fuel Economy Validation

The time trajectories of the powertrain produced from the full vehicle simulations, presented in the previous section, were tested on the engine dynamometer experimental setup to verify the predicted fuel economy improvements. For the baseline turbocharged engine, the crankshaft torque and speed are supplied to the dynamometer and for the PSS engine, the motor torque and the PSS mode are also provided. Figure 5.8 shows a schematic of this process along with the vehicle Simulink model (top left) and a picture of the engine dynamometer (bottom left).

Figure 5.9 presents the experimentally measured fuel economy for the baseline engine and for the PSS engine with cooled EGR on the FTP75 cycle. The baseline engine generates a FE of 38 mpg over the FTP75 cycle. This is higher than the simulation prediction (33.86 mpg), because in the experiment the fuel was cut off during vehicle braking to improve torque control and provide repeatability. The same fuel cut off strategy was also used for the engine with PSS. The middle bar in Figure 5.9 shows the fuel economy of the engine with PSS and EGR, excluding start/stop functionality. In a vehicle the engine is connected to a torque converter, which is unlocked when the starter is cranking the engine, while in the engine dynamometer setup the engine is directly connected to the dynamometer and it is not possible to reproduce the in-vehicle start/stop behavior with the PSS electric motor. The FE improvement of this case compared to the baseline turbocharged engine is written in parenthesis next to the FE result, showing a 16.8% FE increase relative to the baseline turbocharged engine.

The right bar in Figure 5.9 is produced by removing the idling segments of the results in the middle bar and adding 0.28 grams of fuel penalty for each engine cranking event.

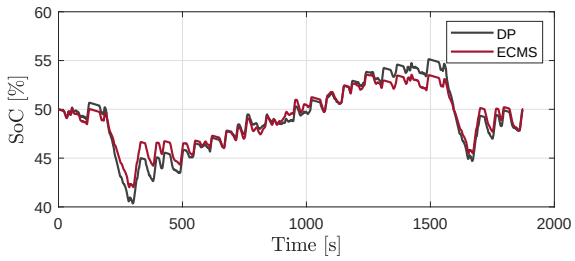

(a) FTP75

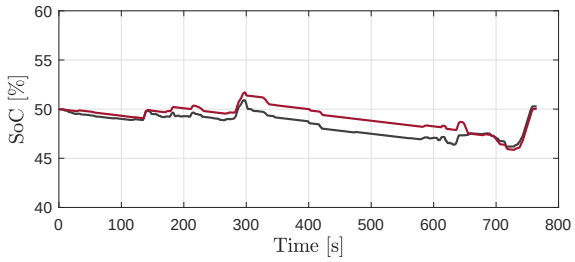

(b) HWFET

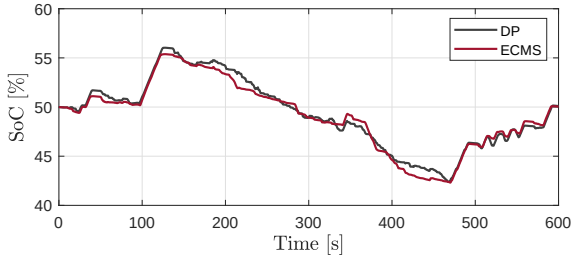

(c) US06

Figure 5.7: The battery state of charge variation with ECMS compared to DP over, (a) the FTP75 cycle, (b) the HWFET cycle, (c) the US06 cycle.

This adjustment yields a FE improvement of 35.5%. As shown previously in Figure 3.3(c) the engine fuel consumption reduces by 3%-4% when including 20% cEGR. Reducing this amount from the experimental FE, the FE improvement with only the PSS should be around 31%, which is in agreement with the simulation results reported in Table 5.1.

Figure 5.10(a) shows the velocity profile for a segment of the FTP75 cycle and Figures 5.10(b), 5.10(c), and 5.10(d) show the crankshaft torque, engine speed, and electric motor torque respectively, supplied into the engine dynamometer along with the measured feedback values. The engine speed and electric motor torque track the desired values almost perfectly. The crankshaft torque tracking, although not as good the other two variables, is still acceptable. Figures 5.11(a) and 5.11(b) show the commanded shaft power versus the feedback value for both the baseline engine and the PSS engine along with some other statistics. The power R^2 for both engines is more than 90%.

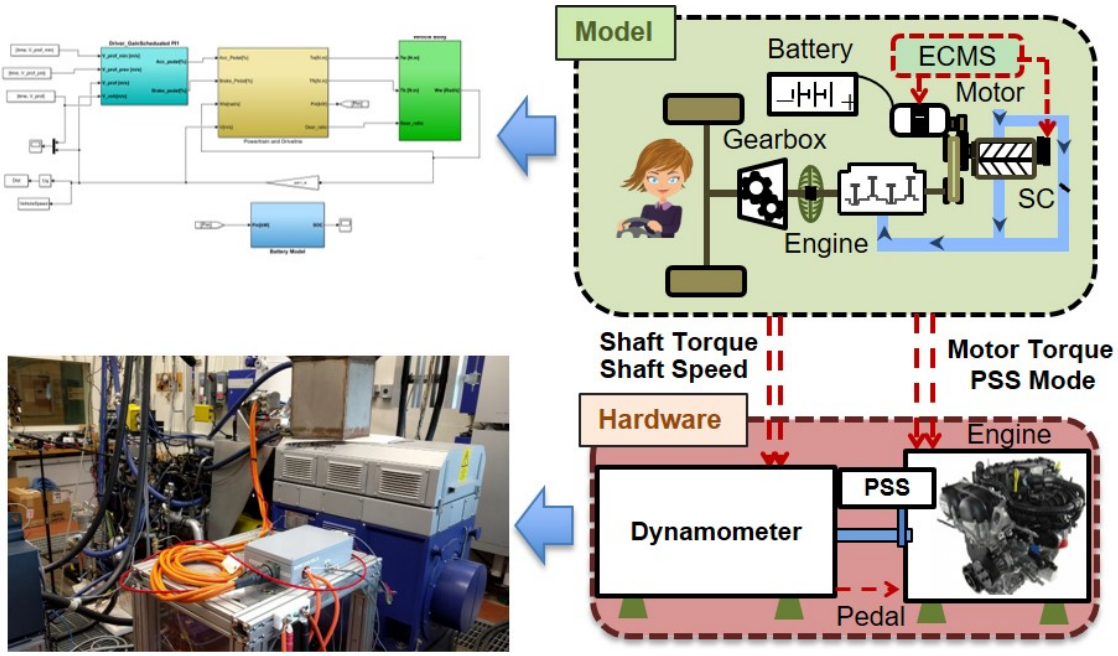

Figure 5.8: A schematic of the adopted fuel economy validation process, with a picture of the vehicle Simulink model on top left corner and a picture of engine dynamometer experimental set up on the bottom left corner.

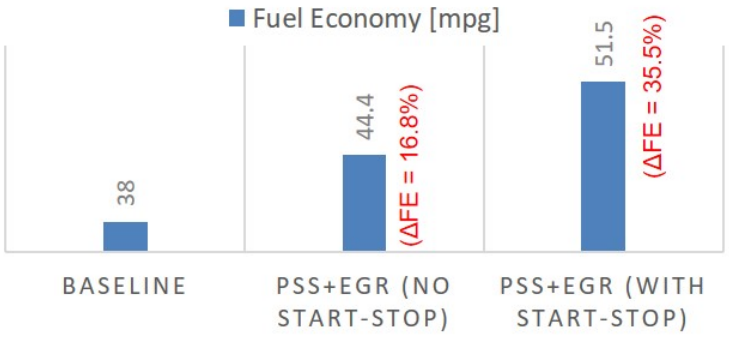

Figure 5.9: The experimental fuel economy for the FTP75 drive cycle, produced using engine dynamometer setup.

5.7 Adaptive ECMS

The ECMS equivalence factor used in the energy management of the PSS system in previous sections was tuned offline for a charge sustaining solution. However, in real world applications the future velocity profile is not known. Therefore, it is necessary to tune the ECMS factor in real time to ensure acceptable operation of the energy management system, especially when starting from an unfavorable initial condition. In this part an Adaptive

ECMS (A-ECMS) is used to adjust the equivalence factor,

$$\alpha_{\text{eq}}(k) = \begin{cases} 0.25 & \text{if} \quad \text{SoC} < 40\% \\ 0.15 & \text{if} \quad \text{SoC} > 60\% \\ \alpha_{\text{eq}}(k-1) + q\big(SoC(k) - SoC(k-1)\big) & \text{otherwise} \end{cases} \tag{5.19}$$

where q is a constant coefficient. The recursive equation for updating α_{eq} when $40\% \leq SoC \leq 60\%$ is derived from the literature [86]. The sampling time for equation (5.19) is chosen as 15 seconds. Figures 5.12 and 5.13 present the performance of equation (5.19) for an initial SoC of 10% and 90% on the FTP75 cycle. Figures 5.12(a) and 5.13(a) show the SoC and Figures 5.12(b) and 5.13(b) present the equivalence factor. This method successfully drives the final SoC to the desired window of [40% 60%].

Figures 5.14, 5.15, and 5.16 compare the SoC and the equivalence factor of the A-ECMS method with SoC(0)=50% to the ECMS results presented in Section 5.5 over the standard EPA drive cycles, and Table 5.2 compares the A-ECMS predicted FE to the ECMS FE. The A-ECMS generated SoC trajectory is different from the ECMS results, but the produced FEs are within 0.2 mpg. The US06 FE improvement is 0.5% larger with A-ECMS. The reason is that in these simulations some hysteresis is added to the PSS switching mode strategy. Such that it switches to the boosting mode only when boosting is requested for more than 0.5 second and it switches back to torque assist mode when it is requested for more than a second.

Table 5.2: Drive cycle simulation results for Ford Escape with Adaptive ECMS (A-ECMS) compared to ECMS. The numbers in parenthesis show the relative fuel economy improvement compared to the turbocharged engine.

Powertrain	Model Type	Energy Management	FTP75 Cycle FE [mpg]	HWFET Cycle FE [mpg]	US06 Cycle FE [mpg]	Combined Cycle FE [mpg]
Turbocharged	Full	-	33.86	47.98	30.22	39.03
Engine + PSS	Full	ECMS	44.54 (31.5%)	49.90 (4.0%)	31.95 (5.7%)	46.80 (19.9%)
Engine + PSS	Full	A-ECMS	44.39 (31.1%)	49.99 (4.1%)	32.14 (6.2%)	46.75 (19.8%)

5.8 Summary

This chapter presented an online energy management system for fuel consumption minimization of a vehicle equipped with a power split supercharger. This controller selects the device mode and the motor torque by minimizing an equivalent fuel flow rate of the engine and the electric motor at each time instant. The online controller, ECMS, generates results consistent with the DP global optimum solution for both the PSS mode and motor torque selection. The ECMS controller was implemented on a Ford Escape vehicle model with full engine air path dynamics. The results showed that the developed strategy is capable of replicating the DP produced FE gains by more than 90%, where the fuel economy gain of

the PSS engine was 31.5% over the FTP75 and 4.0% over the HWFET with ECMS.

The time trajectories from full vehicle simulations were supplied to the engine dynamometer experimental setup and it was shown that the PSS combined with cooled EGR can improve the vehicle fuel economy by 35.5% over the FTP75 cycle. Given that the engine fuel consumption reduces by 3%-4% when including 20% cEGR, the FE improvement with only the PSS is around 31%, which is in agreement with the simulation results. Finally, an adaptive ECMS strategy from the literature was adopted to tune the ECMS factor online based on the battery state of charge. It was shown that although the generated SoC trajectory of adaptive ECMS is different from the ECMS results, the produced FEs are within 0.2 mpg.

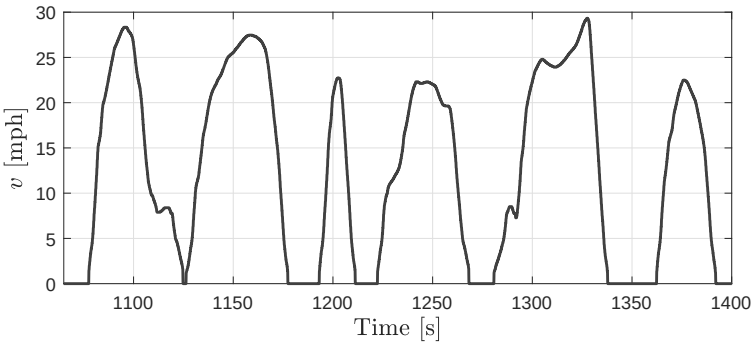

(a) Vehicle velocity

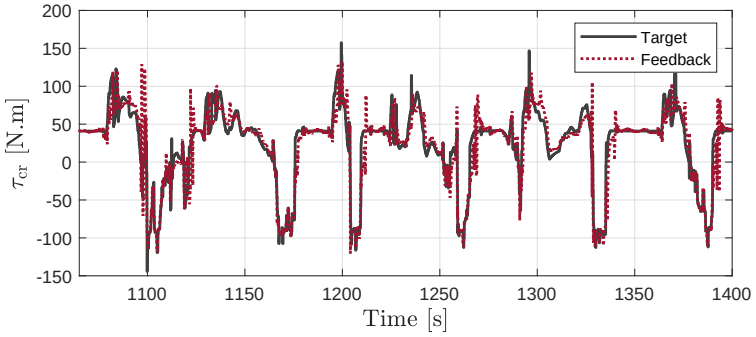

(b) Crankshaft torque

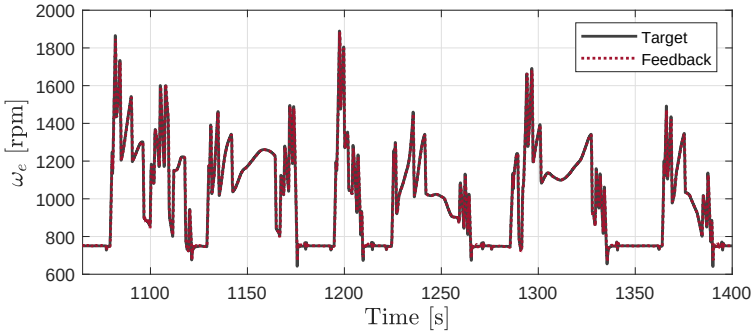

(c) Engine Speed

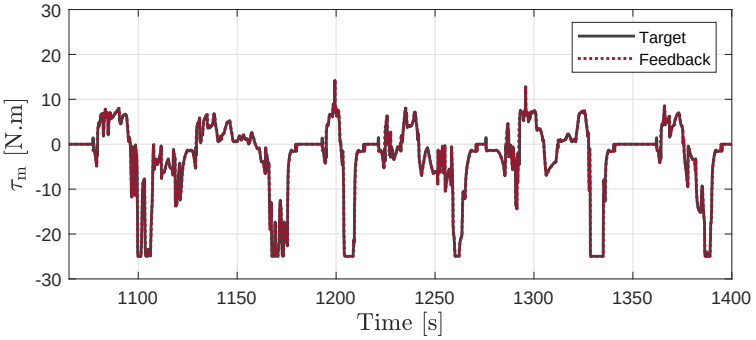

(d) Motor torque

Figure 5.10: The simulation time trajectories supplied to the engine dynamometer (Target) and the measured feedback values (Feedback) for a segment of the FTP75 cycle, (a) velocity profile of the presented segment, (b) crankshaft torque, (c) engine speed, (d) electric motor torque.

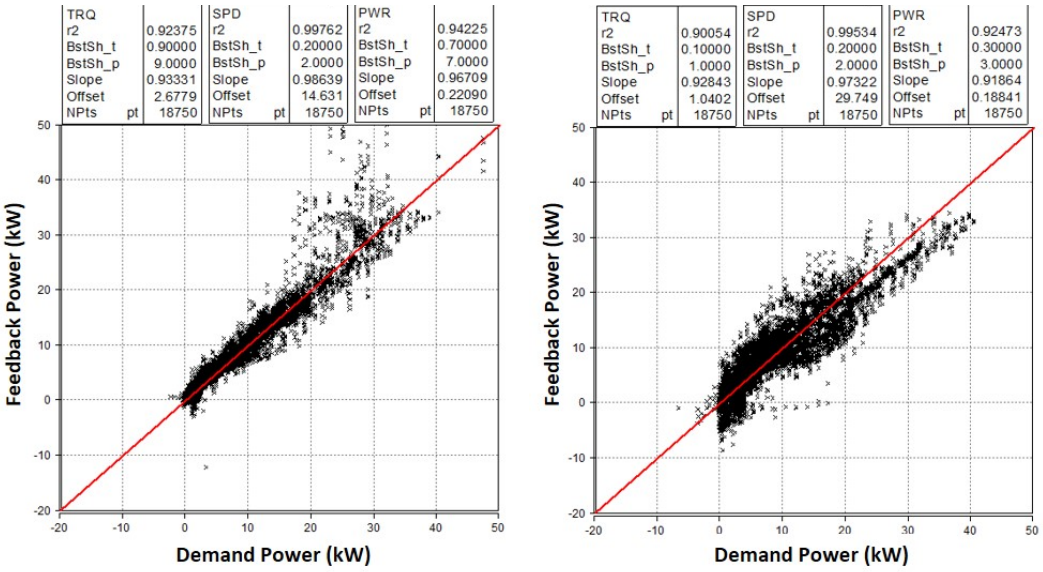

(a) Turbocharged engine (b) Engine with PSS

Figure 5.11: The commanded crankshaft power versus the feedback value from the engine dynamometer experiment for the FTP75 cycle and for, (a) the baseline turbocharged engine, (b) the engine with PSS and EGR.

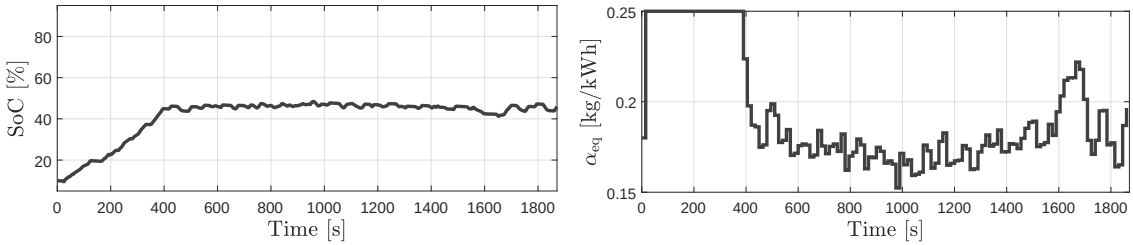

(a) SoC (b) Equivalence factor

Figure 5.12: The A-ECMS performance with initial battery state of charge of 10% over FTP75 cycle, (a) battery state of charge, (b) equivalence factor.

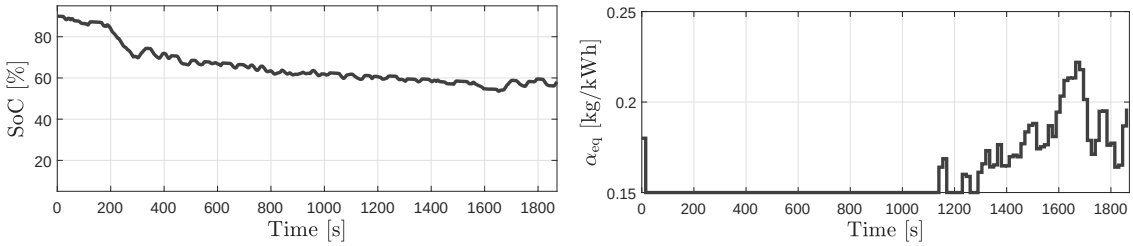

(a) SoC (b) Equivalence factor

Figure 5.13: The A-ECMS performance with initial battery state of charge of 90% over FTP75 cycle, (a) battery state of charge, (b) equivalence factor.

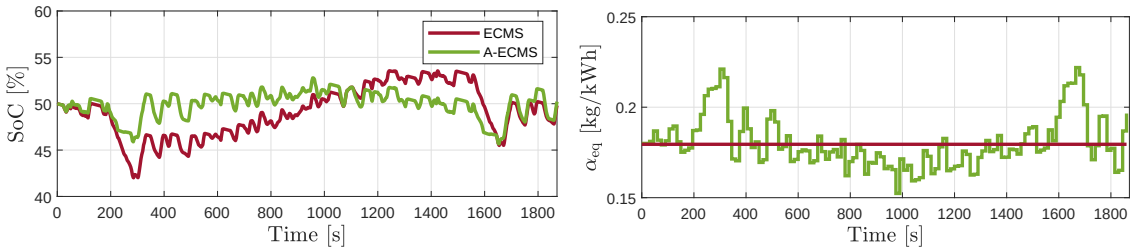

(a) SoC (b) Equivalence factor

Figure 5.14: The A-ECMS performance compared to ECMS for the FTP75 cycle, (a) battery state of charge, (b) equivalence factor.

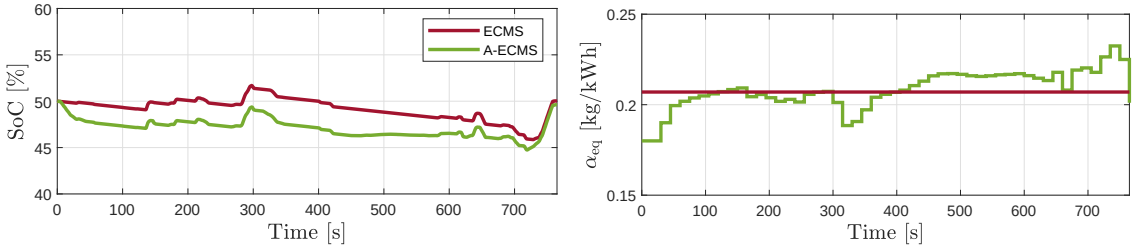

(a) SoC (b) Equivalence factor

Figure 5.15: The A-ECMS performance compared to ECMS for the HWFET cycle, (a) battery state of charge, (b) equivalence factor.

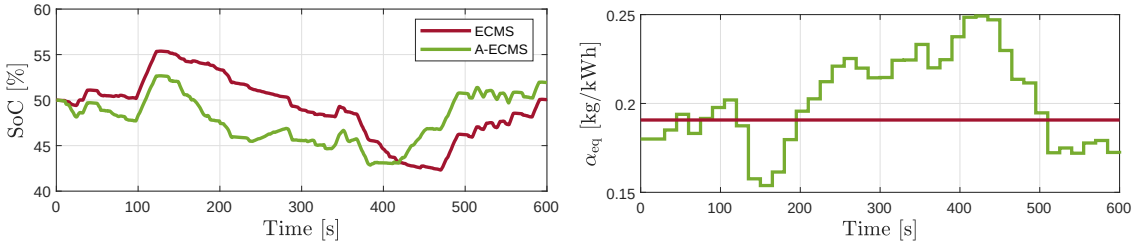

(a) SoC (b) Equivalence factor

Figure 5.16: The A-ECMS performance compared to ECMS for the US06 cycle, (a) battery state of charge, (b) equivalence factor.

CHAPTER VI

Eco-Driving Paired with Hybridization

Many assisting systems are developed to advise drivers on fuel efficient habits and maneuvers, called eco-driving, [87, 88]. Eco-driving is attracting extra attention these days due to the growing vehicle autonomy. Efficient driving styles can be programmed into the automated vehicles and advanced driving assistance systems, such as adaptive cruise control [89, 90], to increase their fuel economy impact compared to non-automated vehicles that depend on a driver.

This chapter studies the synergy between hybridization and eco-driving. Specifically, it investigates the necessary degree of hybridization when velocity profile smoothing is employed, as well as the benefit of eco-driving for an existing hybrid powertrain. Hybridization diversifies the energy source of a vehicle and permits resource allocation optimization. Hybrid electric vehicles enable recovering the vehicle kinetic energy during braking and using it later for propulsion. Likewise, eco-driving saves fuel by avoiding braking and retaining the kinetic energy. This analogy in concept influences the hybridization demand for eco-driving.

Eco-driving is shown to be effective for both conventional internal combustion engines and HEVs [91, 92]. However, full HEVs depend on large electric machines and battery packs, and high voltage electronics, which increase their price. Micro and mild hybrids on the other hand, realized with low voltage (<60V) electrical systems and low power machinery, are cheaper and can partially provide HEV functionalities such as start/stop, regenerative braking and torque assist/generation [25, 26].

This chapter formulates the fuel consumption minimization problem for a vehicle equipped with the PSS in a car following scenario. To defeat the curse of dimensionality, the velocity optimization and the energy management problem for the hybrid vehicle are formulated and solved independently, which is sub-optimal but still effective. The velocity optimization problem is presented after introducing the studied vehicle and engine. The energy management problem is solved on the optimized (smoothed) cycle using dynamic programming and the drive cycle fuel economy results for the engine with PSS and different motor sizes over the standard and optimized cycles are demonstrated. The fuel economy numbers are compared to a turbocharged engine and a full parallel HEV. The hybridization

requirements for the optimized cycles and the eco-driving benefit for different motor sizes are discussed in the final part of the chapter.

6.1 Studied Vehicle and Engine

The modeled vehicle is a Ford Escape MY2015 with 6 speed automatic transmission. The baseline engine is a 1.6 L EcoBoost gasoline 4 cylinder 4 stroke spark ignition turbocharged engine. All studied hybrids use the same engine block after the turbocharger is removed. Figure 6.1 shows a schematic view of the vehicle and the engine with the PSS.

The EcoBoost engine with a PSS can provide good acceleration even with a small electric motor, hence instead of a conventional hybrid system, the PSS is used in this study. This feature enables studying the fuel economy of a vehicle with the same engine and transmission but with different electric motor sizes, while having comparable drive-ability.

6.2 Fuel Consumption Minimization in a Car Following Scenario

The fuel consumption of a vehicle depends on both the high-level vehicle velocity profile and the low-level powertrain energy management. In an automated car following scenario, the vehicle position has to comply with the traffic condition, hence it has to be included in the optimal control problem in addition to the vehicle velocity. On the other hand, the energy management of a hybrid electric system, like the PSS, has more inputs due to its switching mode. Consequently, the fuel consumption minimization of an automated vehicle equipped with the PSS has a large dimensionality and cannot be address efficiently with the methods that find the global optimum solution such as DP. Therefore, this work solves the velocity profile optimization and the energy management of the hybrid system separately,

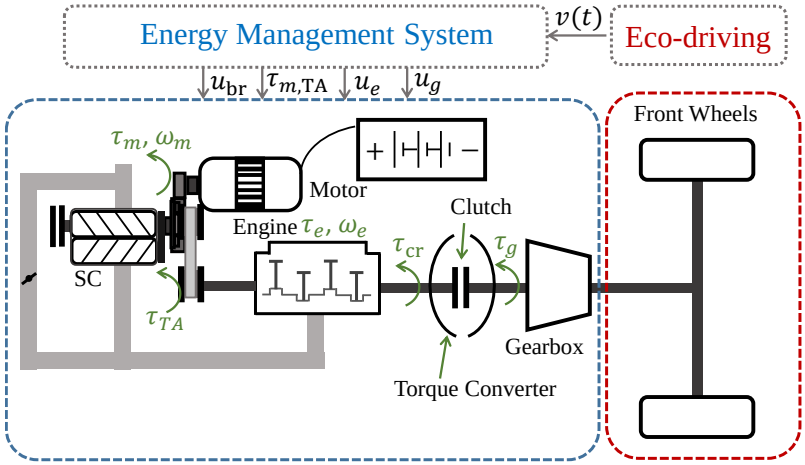

Figure 6.1: Schematic view of the vehicle and drivetrain with the power split supercharger.

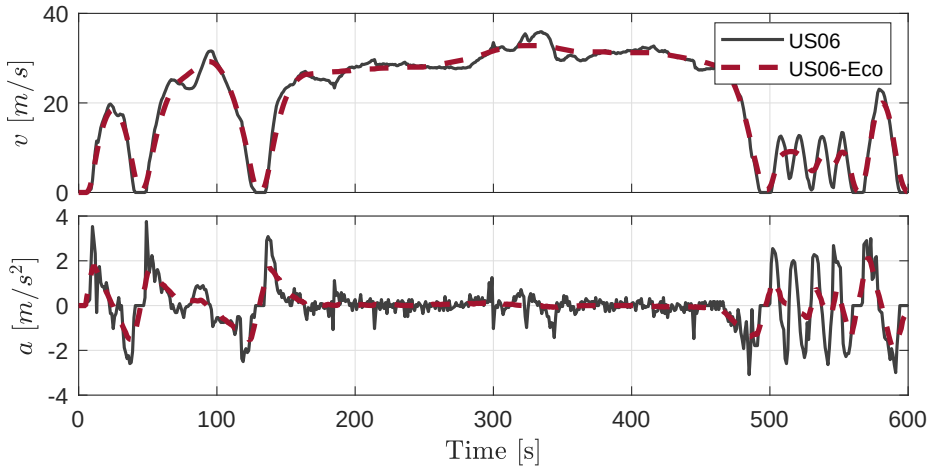

(a) US06

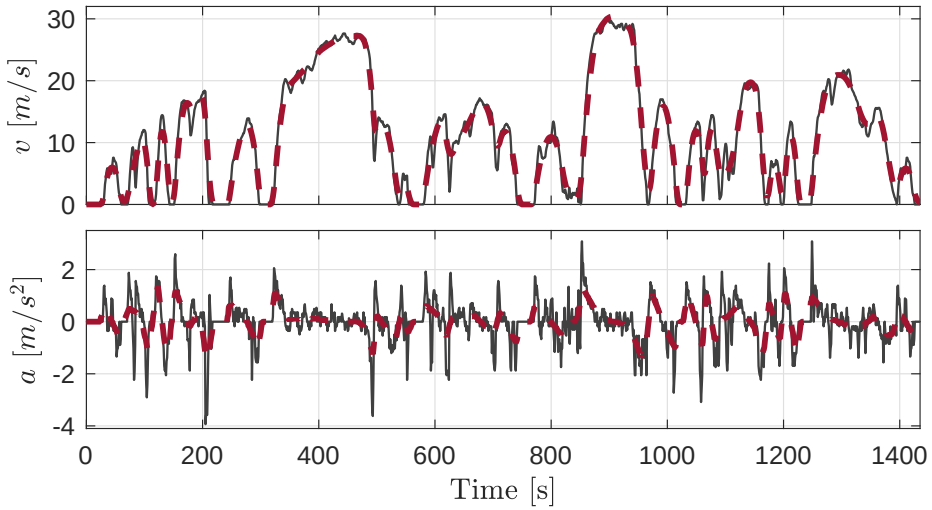

(b) LA92

Figure 6.2: Standard and optimized velocity profile and acceleration profile, (a) US06 cycle, (b) LA92 cycle.

as shown in Figure 6.1. This sequential strategy is sub-optimal, but still effective in fuel consumption reduction per this work. In the following sections each optimization problem is discussed briefly.

6.2.1 Velocity Profile Optimization

To achieve a smooth velocity profile and hence eco-driving, the second norm of the vehicle acceleration, a, is minimized,

$$\min \sum_{1}^{N} ||a(k)||_2^2 \tag{6.1}$$

subject to vehicle equations of motion and input and state constraints,

$$x(k+1) = x(k) + v(k)T_s + \frac{1}{2}a(k)T_s^2 \tag{6.2a}$$

$$v(k+1) = v(k) + a(k)T_s \tag{6.2b}$$

$$a^{\min} \leq a(k) \leq a^{\max} \tag{6.2c}$$

$$v^{\min} \leq v(k) \leq v^{\max} \tag{6.2d}$$

$$x(k)^{\min} \leq x(k) \leq x(k)^{\max} \tag{6.2e}$$

Equations (6.2a) and (6.2b) describe the vehicle longitudinal model, which is a second order Linear Time-Invariant (LTI) model with position, x, and velocity, v, as system states and acceleration as system input. T_s is the sampling time equal to 1 second. Equation (6.2c) limits the acceleration and (6.2d) constrains the velocity. The position constraints, (6.2e), are based on the distance from the hypothetical lead vehicle.

The concept of a hypothetical lead vehicle, introduced in [93], is found for any standard drive cycle by inverting the Intelligent Driver Model (IDM) [94]. This method would allow simulating the actual traffic conditions associated with the Federal drive cycles and also provides a consistent comparison between how humans follow traffic and how optimal controllers would follow the same traffic conditions while avoiding accidents. For more information about the hypothetical lead vehicle and the optimization problem (6.1) please see [93]. Figure 6.2(a) represent the velocity profile of the US06 and the optimized velocity profile from (6.1) and (6.2), with "Eco" suffix in this work. As seen the US06-Eco cycle has a smoother velocity profile with less acceleration and decelerations. Note that the traveled distance for both cycles is fixed. Figure 6.2(b) shows the standard LA92 and optimized LA92 cycles.

6.2.2 Energy Management System

The details of the optimal control problem for energy management of a vehicle with an automatic transmission and PSS is described in details in Chapter IV, here only a summary is presented. The optimal control problem inputs are the commanded torque assist, $\tau_{m,\mathrm{TA}}$, gear shift command, u_g, the PSS mode, u_{br}, and the engine on/off command, u_e. The modeled states are the battery state of charge, ζ, gear number, n_g, and the engine on/off state x_e. The optimal control problem cost function compensates the fuel flow rate, $\dot{m}_f$, the gear shift, the engine cranking for starting the engine and the PSS mode, as follows,

$$\min \left\{ \sum_{k=1}^{N} \left(\dot{m}_f(k)T_s + \alpha \left| n_g(k) - n_g(k-1) \right| \right.\right.$$
$$\left.\left. + \beta \Big(\max\big(x_e(k) - x_e(k-1), 0\big) \Big) + \lambda \Big(1 - u_{\mathrm{br}}(k) \Big) \right) \right\} \tag{6.3}$$

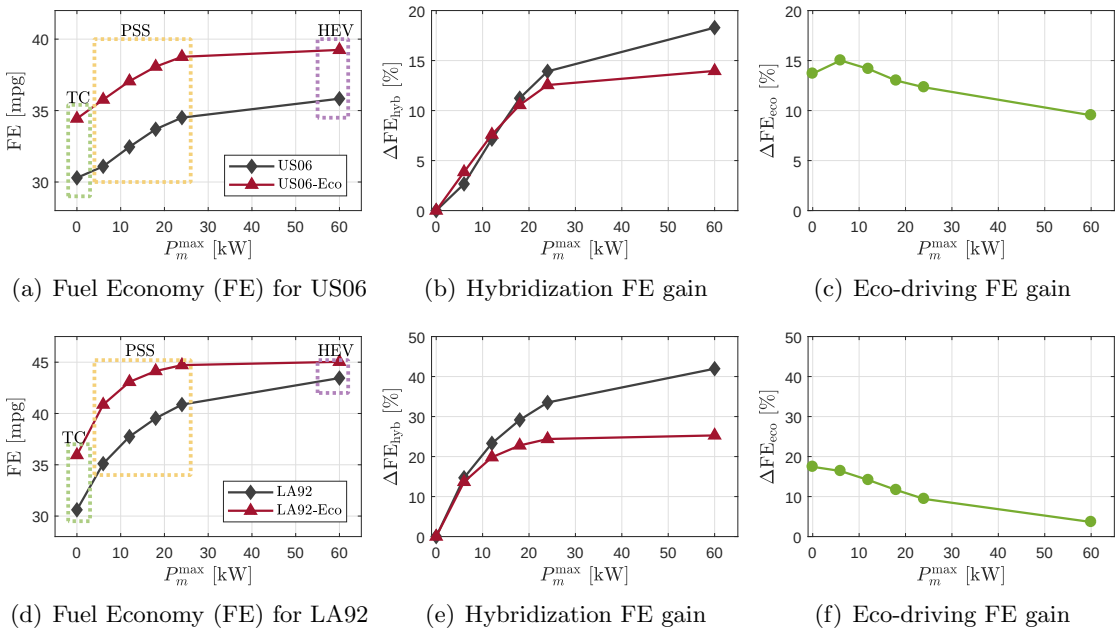

(a) Fuel Economy (FE) for US06 (b) Hybridization FE gain (c) Eco-driving FE gain

(d) Fuel Economy (FE) for LA92 (e) Hybridization FE gain (f) Eco-driving FE gain

Figure 6.3: Drive cycle FE results, (a) FE of turbocharged and hybridized engines over the US06, (b) relative FE change compared to the turbocharged engine over the US06, (c) eco-driving FE improvement over the US06, (d) FE of turbocharged and hybridized engines over the LA92, (e) relative FE change compared to the turbocharged engine over the LA92, (f) eco-driving FE improvement over the LA92.

The problem constraints are described in (4.20a) to (4.20n).

Note that to find the global optimum solution, the problem horizon for both the energy management and velocity optimization has to be the entire drive cycle. This means that determining the optimal control strategy in current time step requires the knowledge of future driving demands, which produces an acausal solution that cannot be implemented in an online controller. Nevertheless, this method is still very useful because it provides a benchmark for evaluating the effectiveness of different powertrains and driving concepts. In this work, a MATLAB-based dpm function [82] that applies DP is used for finding the global optimum solution of (6.1) and (6.3).

6.3 Drive Cycle Simulation Results

The optimal control problem is solved over two standard cycles and the corresponding optimized cycles. The US06 and LA92 cycles were selected to study in this work because they include aggressive transients, necessitating full hybridization for high fuel economy impact. Figure 6.3(a) compares drive cycle FE for the standard US06 cycle (black) and the US06-Eco cycle (red). The horizontal axis is the motor peak power ($P_m^{\max}$), where zero power stands for the turbocharged engine that has no hybridization. The 60 kW case corresponds

to a full parallel HEV and the other cases represent the engine with PSS, but with different motor sizes. The optimal energy management for the turbocharged engine and the full HEV is also formulated and solved using DP.

Figure 6.3(b) shows the hybridization FE gain, (ΔFE_{hyb}), computed as follows:

$$\Delta FE_{hyb} = \frac{FE - FE_{TC}}{FE_{TC}} \times 100 \tag{6.4}$$

where for each cycle FE_{TC} is the fuel economy of turbocharged vehicle on the same cycle. Figure 6.3(c) represents eco-driving FE gain, ΔFE_{eco},

$$\Delta FE_{eco} = \frac{FE_{Eco} - FE_{std}}{FE_{std}} \times 100 \tag{6.5}$$

in which FE_{std} is the fuel economy of each case over the standard drive cycle and FE_{Eco} is its fuel economy over the Eco cycle. Figure 6.3(d), 6.3(e), and 6.3(f) show corresponding results for the LA92 cycle.

Both eco-driving and hybridization improve the vehicle fuel economy. For example the fuel economy of the turbocharged engine over the US06 increases from 30.3 mpg to 34.4 mpg with eco-driving and to 39.0 mpg with full hybridization. Inspecting the results, the following less intuitive features are observed.

- Over the Eco cycles, the PSS with a smaller motor can give the FE gain of a full HEV.
- The FE benefit of eco-driving is smaller for a larger motor size, i.e. a higher hybridization degree.
- For full HEV, while eco-driving provides around 10% FE gain on the US06, it yields a much smaller benefit of 3% over the LA92.

In the following sections each item is discussed in more details.

6.3.1 Hybridization Degree for Eco-driving

Increasing the motor size provides a higher FE on both standard and Eco cycles. However, this relationship is not strictly increasing. For each vehicle and driving profile, there is a minimum motor size that maximizes the FE. This trend is seen in Figures 6.3(b) and 6.3(e). More importantly, the Eco cycles hybridization FE benefit saturate with a smaller motor size, meaning that on the Eco cycles a smaller motor can provide the FE of a full HEV. On the standard US06 cycle, a 24 kW motor can produce 75% of a full HEV benefit but over the Eco cycle it can produce 90% of a full HEV FE gain. Likewise, on the LA92, an 18 kW motor generates only 68% of a full HEV benefit, while with Eco-driving it can achieve 90% of the FE gain.

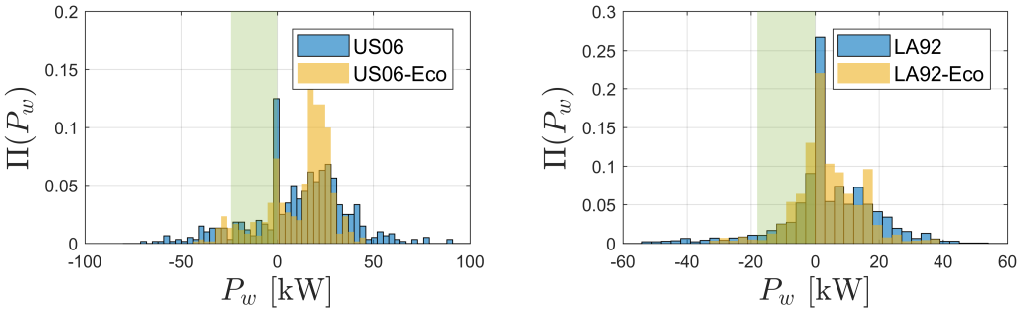

(a) US06 (b) LA92

Figure 6.4: Distribution of power at wheels, (a) US06 cycle, (b) LA92 cycle.

Eco-driving smooths the vehicle accelerations and decelerations. This fact is shown in Figures 6.4(a) and 6.4(b), which show the probability distribution, Π, of power demand at wheels, P_w, for the considered drive cycles. A positive number shows traction and a negative number shows braking. As seen for both cycles eco-driving pushes the power demand distribution towards center. The highlighted green area are the region that a 24 kW motor, for US06, and an 18 kW motor, for LA92, can fully recover the vehicle kinetic energy during braking. For braking power outside the highlighted area the motor can still partially recover the vehicle kinetic energy. As seen, for the Eco cycles, the largest part of the braking power lies within the highlighted area.

Figure 6.5 shows the percentage of the recovered vehicle kinetic energy during braking, $\frac{\mathrm{E_{regen}}}{\mathrm{E_{brake}}}$, verses FE gain of the each system compared to the full HEV FE gain, $\frac{\Delta \mathrm{FE_{hyb}}}{\Delta \mathrm{FE_{hyb}^{HEV}}}$,

$$\mathrm{E_{regen}} = \int_{P_w<0} P_m(t)dt \tag{6.6a}$$

$$\mathrm{E_{brake}} = \int_{P_w<0} P_w(t)dt \tag{6.6b}$$

where P_m is the motor power, E_{regen} is the regenerated energy during vehicle braking and E_{brake} is the total wheels energy that is either regenerated or dissipated in friction brakes.The motor size is written within the markers. Figure 6.5 indicates that the FE gain of the studied hybrids compared to the full HEV FE benefit is equivalent to the percentage of the recovered braking power. In other words, for each cycle it is only sufficient to determine the fraction of the wasted energy during braking to determine the fuel economy benefit of the system compared to full HEV case. For example a 12kW motor recovers 40% of the braking energy on the standard US06 and accordingly gives around 40% of a full HEV FE benefit. Eco-driving smooths the velocity profile and permits recovering a larger portion of vehicle kinetic energy during braking with a small motor, hence a lower hybridization degree is sufficient with eco-driving to maximize the FE benefits of the vehicle.

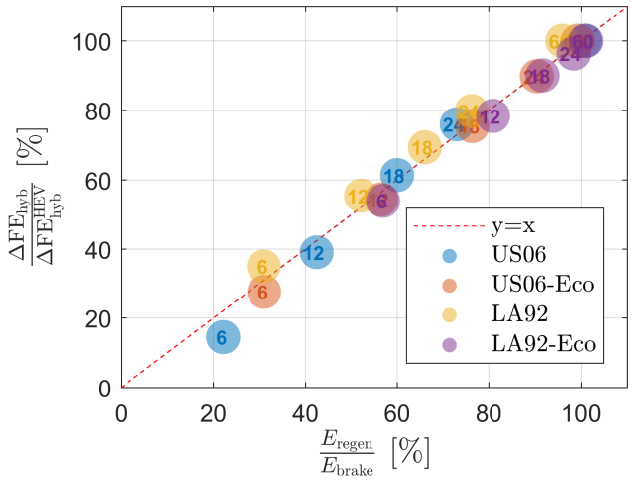

Figure 6.5: The relation between the ratio of recovered energy during braking and FE gain over the FE gain of full HEV.

6.3.2 Eco-driving Benefit for Hybrid Electric Vehicles

The drive cycle simulation results indicate that eco-driving benefit is largest for the turbocharged vehicle and as the motor size in a hybrid vehicle increases the FE benefits of eco-driving drops, as shown in Figures 6.3(c) and 6.3(f). For example, the eco-driving FE gain is 17% for a turbocharged vehicle over LA92 and only 3% for the full HEV. Similar trend is observed for the US06 cycle.

The ultimate source of vehicle propulsion in a hybrid electric vehicle is fuel. Both eco-driving and hybridization guide the engine operating points into more efficient areas and save fuel. This fact is shown in Figures 6.6(a) and 6.6(b), which compare the engine torque probability distribution for the turbocharged engine over the standard US06 to its distribution over US06-Eco and to the probability distribution of the engine torque with PSS and 18 kW motor. Note that these two cases have around the same FE in Figure 6.3(a). As seen, both hybridization and eco-driving decrease the instances of high torque demands and instead, they push the operating points towards the engine efficiency sweet spot that is around 130 N.m torque. Considering this similarity on how hybridization and eco-driving work, it makes sense that eco-driving will be less rewarding for hybrid vehicles with larger motors.

Despite all similarities for the two studied cycles, for a full HEV, eco-driving produces only 3% FE benefit on the LA92, but it generates 3 times more FE gain on the US06, 10%. The reason for this significant difference lies within the US06 drive cycle profile, shown in Figure 6.2(a). As seen, the US06 is a highly non-smooth profile, which necessitates frequent downshifts even for a full HEV, as shown in Figure 6.7. These inevitable downshifts push the engine to work at higher speeds and higher fuel consumption rates, shown in Figure 6.8(a) along with the fuel flow rate contours. Eco-driving on the other hand, smooths the

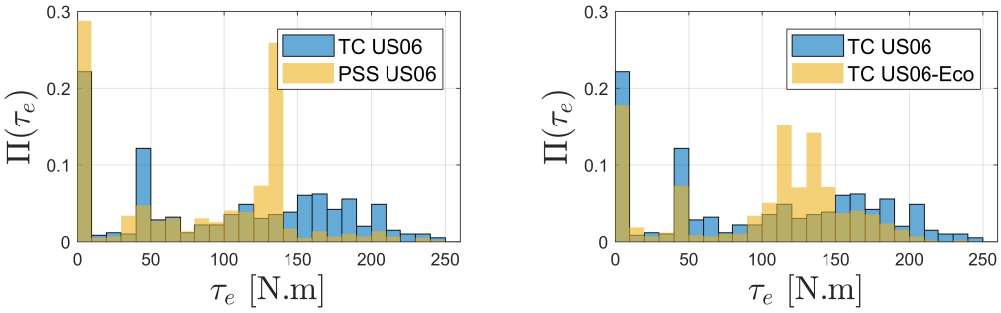

(a) Hybridization (b) Eco-driving

Figure 6.6: The change in turbocharged engine torque distribution with, (a) hybridization, (b) eco-driving.

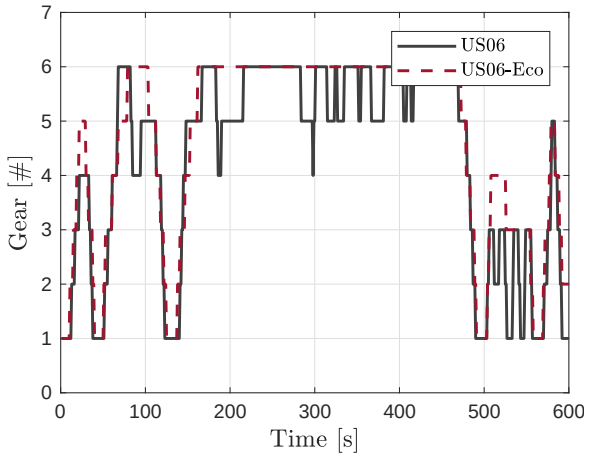

Figure 6.7: Gear change during the US06 and US06-Eco cycles for full HEV

velocity profile and avoids frequent downshifts, resulting in engine operating at lower speeds and lower fuel flow rates, demonstrates on Figure 6.8(b). This difference is not observed for the engine operating points over the LA92 cycle, displayed in Figure 6.8(c) and 6.8(d).

6.4 Summary

This chapter formulated the fuel consumption minimization for a power split supercharger in a car following scenario. The velocity profile optimization and the energy management problem were solved sequentially to overcome the curse of dimensionality. Both the fuel economy gain of hybrid vehicles from eco-driving and the vehicle hybridization gain with eco-driving were studied. The results indicated that the fuel economy benefit of eco-driving reduces as the motor size in the hybrid system increases, such that it produces the largest gain for a non-hybrid vehicle and the smallest gain for a full hybrid. It was also shown that over an optimized velocity profile the power split supercharger with a small motor can

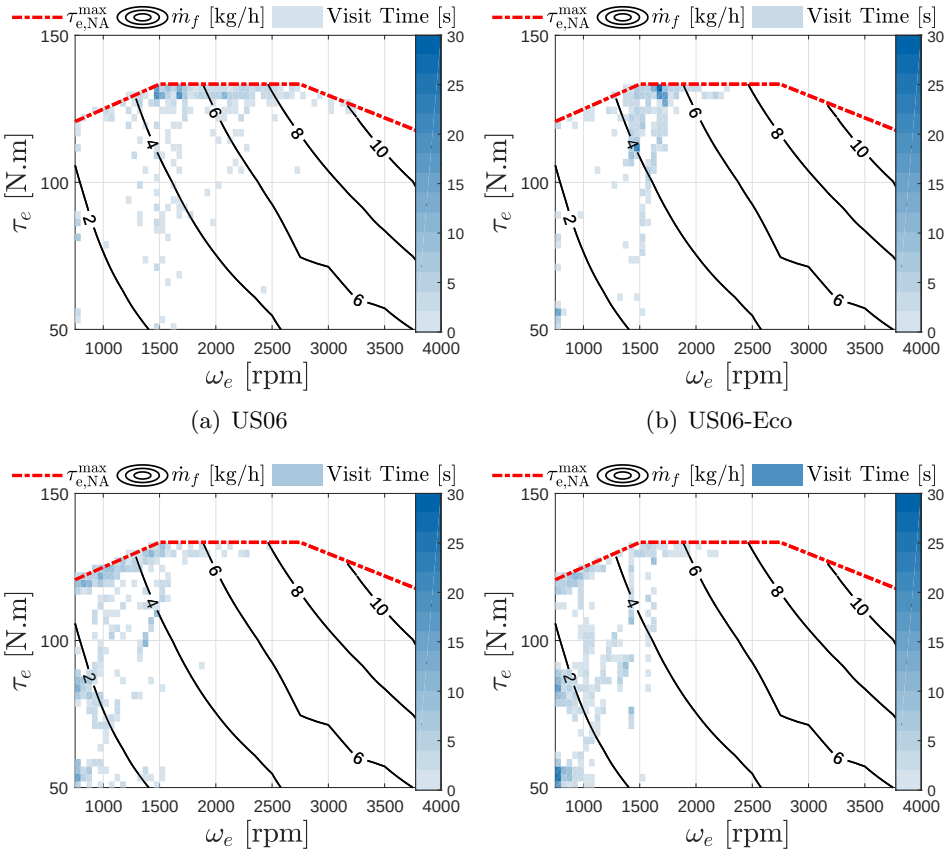

(a) US06 (b) US06-Eco

(c) LA92 (d) LA92-Eco

Figure 6.8: Engine visitation points for full HEV based on spent time at each operating point over, (a) US06 cycle, (b) US06-Eco cycle, (c) LA92 cycle, (d) LA92-Eco cycle.

provide most of a full HEV fuel economy improvement. For example over the US06-Eco, a 24 kW motor and for the LA92-Eco an 18 kW motor can give 90% of a full HEV FE gain. These results indicate that the future automated vehicles that can precisely optimize their velocity profile can benefit from hybridization with small electrical components at a lower cost.

CHAPTER VII

Conclusions and Future Work

7.1 Results and Conclusions

Hybridization is one of the key technologies pursued by vehicle manufacturers to improve the fuel economy of vehicles. Hybrid electric vehicles use an electric motor in addition to an internal combustion engine for driving a vehicle. This practice diversifies the propulsion source of a vehicle and allows utilizing each source efficiently. The majority of prior studies focus on full HEVs, realized by large electric machines and high voltage systems, both of which are expensive. This work focused on a novel low-voltage HEV configured with a 48V electrical system and a small motor, called a Power Split Supercharger (PSS). The PSS can switch between providing power to the crankshaft (for start/stop, regenerative braking or torque assist) to variable speed supercharging.

This work presented a decentralized controller for air path control problem of a twin-charged engine with both a turbocharger and a PSS. The proposed boost controller has a master-slave structure, in which the high stroke supercharger, is slaved to the turbocharger so that it is only used during transients. The decentralized controller is configured such that while having a fast response the supercharger usage is minimized for fuel consumption. The designed controller was validated against a high fidelity GT-Power engine model and the performance of the controller during both constant and varying engine speed transients was validated. It was shown that the power split supercharger with the designed controller is capable of reducing the engine response time from 2.3 seconds to less than 0.5 second. Furthermore, the motor only partially powers the supercharger, reducing the electric energy consumption over a drive cycle relative to a completely electrically driven supercharger.

This work also formulated an optimization problem for energy management of two mild hybrid systems both capable of boosting and parallel hybrid operation, one with a single motor (PSS), and the other with two separate motors (eSC-SGM). The optimization inputs for the engine with power split supercharger include the gear shift command, the engine start/stop, the PSS mode and the motor torque when the PSS is in torque assist mode. For this system, input dependent constraints were used to model the switching system structure in different modes. The optimal control problem was discretized and solved using dynamic

programming. The most important findings of this study were:

- Both mild hybrid systems are capable of improving the vehicle fuel economy on combined cycle by 20.7%, which is around 75% of a full HEV benefit. However, on the aggressive US06 cycle the mild hybrids can enhance the fuel economy only by 7-8%, which is 40-50% of the full hybrid fuel economy gain.

- The additional flexibility from a dual motor system is only useful on the US06, where it gives 1.3% more fuel economy gain compared to the single motor system.

- The optimal controller for the engine with PSS often adopts torque assist over supercharging when the torque demand can be met with either mode, yet as the battery size reduces the instances of using the supercharger increases.

- The optimal controller for the two motor eSC-SGM uses both the electric supercharger and torque assist simultaneously to meet high torque demands and the supercharging share increases for a smaller battery or a more efficient supercharger.

- It is not a fuel optimal policy to supercharge the engine and generate electric power from the crankshaft simultaneously in the dual motor system.

- Two causally implementable rules, one that uses the supercharger only when necessary and the other that selects the PSS mode based on the equivalent minimum consumed fuel were proposed and integrated into the optimization problem. It was shown that these rules can produce results very close to optimal fuel economy for different battery sizes and drive cycles.

- Under high load operating conditions such as during a sustained hill climb, the PSS will be in boosting mode and the electric motor will generate some power to charge the battery. This behavior allows continuous use of the PSS at high load conditions without depleting the battery charge.

An online energy management system for fuel economy optimization of a vehicle equipped with a power split supercharger was developed. The energy management system has to select the PSS operating mode in addition to the power split ratio between the engine and the motor if the parallel hybrid mode is selected. An equivalent consumption minimization strategy that selects both the PSS mode and the motor torque for minimizing the sum of the instantaneous engine and motor fuel consumption was introduced. The ECMS results for the PSS mode and motor torque selection were in agreement with the DP solution for global fuel consumption minimization. The ECMS was implemented on a Ford Escape vehicle model with full engine air path dynamics. The results showed that the developed online energy management system is capable of improving the vehicle fuel economy by 31.5% and 4.0% over the FTP75 and HWFET cycles, respectively compared to a baseline turbocharged engine.

These improvements are more than 90% of the DP predicted fuel economy gain. Finally, the time trajectories from full vehicle simulations were supplied to the engine dynamometer experimental setup and it was shown that the PSS combined with cooled EGR can improve a vehicle fuel economy by 35.5% over the FTP75 cycle.

The PSS fuel economy was also compared to a full HEV in an automated car following scenario. To overcome the curse of dimensionality the velocity profile optimization and the hybrid system energy management problem were solved independently. The results indicated that the eco-driving fuel economy benefit drops as the motor size in the hybrid system increases, such that it provides the smallest gain for a full hybrid. It was also shown that over an optimized velocity profile the power split supercharger with a small motor can provide most of a full HEV fuel economy benefit. For example over the optimized US06, a 24 kW motor and for the optimized LA92 an 18 kW motor can give 90% of a full HEV FE gain. This result can contribute to cost reduction in future automated vehicles that are capable of accurate velocity profile optimization with vehicle to vehicle and vehicle to infrastructure communication.

7.2 Future Work and Open Challenges

In this work the fuel economy of the power split supercharger when replacing a turbocharger in a downsized turbocharged engine was studied and validated through engine dynamometer experiments. The next step would be validation of the results on a vehicle. The control algorithms and energy management system developed here are easily implementable on a vehicle ECU. However, the packaging problem has to be addressed for installing the PSS on a vehicle drivetrain, given that the PSS has a larger size compared to a turbocharger and extra space is necessary for the drive belt.

Another direction for future research would be studying the fuel economy of the PSS system in an automated vehicle when limited preview is available. The problem horizon for vehicle velocity optimization in this work was the full drive cycle and the problem was solved using dynamic programming. This choice was made to demonstrate the higher effectiveness of the PSS system in an automated vehicle. It is proposed that in the next step the PSS system fuel economy gain be studied when a limited preview of the traffic ahead is available. Moreover, the simultaneous optimization of the velocity profile and energy management and comparison to the sequential optimization pursued here would be interesting.

BIBLIOGRAPHY

BIBLIOGRAPHY

[1] Z. Yang and A. Bandivadekar, "Light-duty vehicle greenhouse gas and fuel economy standards," 2017.

[2] "1.6 l ecoboost engine geometry," http://dsportmag.com/the-tech/ford-ecoboost-1-6l-analysis-turbocharged-direct-injection-ccvtc/, Accessed: 2017-10-27.

[3] "Total u.s. greenhouse gas emissions by economic sector in 2015," https://www.epa.gov/ghgemissions/sources-greenhouse-gas-emissions, Accessed: 2017-12-28.

[4] "U.S. Transportation Emissions," https://www.c2es.org/content/regulating-transportation-sector-carbon-emissions/, Accessed: 2017-12-28.

[5] L. Eriksson, S. Frei, C. Onder, and L. Guzzella, "Control and optimization of turbocharged spark ignited engines," *IFAC Proceedings Volumes*, vol. 35, no. 1, pp. 283–288, 2002.

[6] S. Nazari, A. Stefanopoulou, and J. Martz, "Minimum backpressure wastegate control for a boosted gasoline engine with low pressure external EGR," in *ASME 2016 Dynamic Systems and Control Conference*. American Society of Mechanical Engineers, 2016, pp. V002T20A002–V002T20A002.

[7] A. Jain, T. Nueesch, C. Naegele, P. M. Lassus, and C. H. Onder, "Modeling and control of a hybrid electric vehicle with an electrically assisted turbocharger," *IEEE Transactions on Vehicular Technology*, vol. 65, no. 6, pp. 4344–4358, 2016.

[8] I. Kolmanovsky, A. Stefanopoulous, and B. Powell, "Improving turbocharged diesel engine operation with turbo power assist system," in *Control Applications, 1999. Proceedings of the 1999 IEEE International Conference on*, vol. 1. IEEE, 1999, pp. 454–459.

[9] G. He and H. Xie, "Fuel saving potential of different turbo-compounding systems under steady and driving cycles," SAE Technical Paper, Tech. Rep., 2015.

[10] S. McBroom, R. A. Smithson, R. Urista, and C. Chadwell, "Effects of variable speed supercharging using a continuously variable planetary on fuel economy and low speed torque," *SAE International Journal of Engines*, vol. 5, no. 2012-01-1737, pp. 1717–1728, 2012.

[11] J. King, M. Heaney, J. Saward, A. Fraser, M. Criddle, T. Cheng, G. Morris, and P. Bloore, "Hyboost: An intelligently electrified optimised downsized gasoline engine concept," in *Proceedings of the FISITA 2012 World Automotive Congress*. Springer, 2013, pp. 483–496.

[12] P. Pallotti, E. Torella, J. New, M. Criddle, and J. Brown, "Application of an electric boosting system to a small, four-cylinder si engine," SAE Technical paper, Tech. Rep., 2003.

[13] S. Nazari, R. Middleton, K. Sugimori, J. Siegel, and A. Stefanopoulou, "Assessing a hybrid supercharged engine for highly diluted combustion using a dynamic drive cycle simulation," SAE Technical Paper, Tech. Rep., 2018-01-0969.

[14] S. Nazari, R. Middleton, K. Sugimori, J. Siegel, and A. Stefanopoulou, "Assessing a hybrid supercharged engine for diluted combustion using a dynamic drive cycle simulation," *SAE Journal of Alternative Powertrains*, 2019.

[15] S. George, G. Morris, J. Dixon, D. Pearce, and G. Heslop, "Optimal boost control for an electrical supercharging application," SAE Technical Paper, Tech. Rep., 2004.

[16] M. Amann and D. Ouwenga, "Engine parameter optimization for improved engine and drive cycle efficiency for boosted, GDI engines with different boosting system architecture," SAE Technical Paper, Tech. Rep., 2014.

[17] C. Stan and S. Taeubert, "Analysis of engine performances improvement by down sizing in relationship with super-and turbocharging, adapted scavenging and direct injection," SAE Technical Paper, Tech. Rep., 2009.

[18] S. Nazari, A. Stefanopoulou, R. Kiwan, and V. Tsourapas, "A coordinated boost control in a twincharged spark ignition engine with high external dilution," in *ASME 2016 Dynamic Systems and Control Conference*. American Society of Mechanical Engineers, 2016, pp. V002T20A003–V002T20A003.

[19] T. Alger, J. Gingrich, C. Roberts, and B. Mangold, "Cooled exhaust-gas recirculation for fuel economy and emissions improvement in gasoline engines," *International Journal of Engine Research*, vol. 12, no. 3, pp. 252–264, 2011.

[20] K. Siokos, R. Koli, R. Prucka, J. Schwanke, and J. Miersch, "Assessment of cooled low pressure EGR in a turbocharged direct injection gasoline engine," *SAE International Journal of Engines*, vol. 8, no. 2015-01-1253, pp. 1535–1543, 2015.

[21] M. Kaiser, U. Krueger, R. Harris, and L. Cruff, "Doing more with less-the fuel economy benefits of cooled egr on a direct injected spark ignited boosted engine," SAE Technical Paper, Tech. Rep., 2010.

[22] J. M. Luján, H. Climent, R. Novella, and M. E. Rivas-Perea, "Influence of a low pressure egr loop on a gasoline turbocharged direct injection engine," *Applied Thermal Engineering*, vol. 89, pp. 432–443, 2015.

[23] L. Teodosio, V. De Bellis, and F. Bozza, "Fuel economy improvement and knock tendency reduction of a downsized turbocharged engine at full load operations through a low-pressure egr system," *SAE International Journal of Engines*, vol. 8, no. 2015-01-1244, pp. 1508–1519, 2015.

[24] D. Takaki, H. Tsuchida, T. Kobara, M. Akagi, T. Tsuyuki, and M. Nagamine, "Study of an egr system for downsizing turbocharged gasoline engine to improve fuel economy," SAE Technical Paper, Tech. Rep., 2014.

[25] C. Silva, M. Ross, and T. Farias, "Analysis and simulation of low-cost strategies to reduce fuel consumption and emissions in conventional gasoline light-duty vehicles," *Energy Conversion and Management*, vol. 50, no. 2, pp. 215–222, 2009.

[26] A. Rick and B. Sisk, "A simulation based analysis of 12v and 48v microhybrid systems across vehicle segments and drive cycles," SAE Technical Paper, Tech. Rep., 2015.

[27] D. Hountalas, C. Katsanos, and V. Lamaris, "Recovering energy from the diesel engine exhaust using mechanical and electrical turbocompounding," SAE Technical Paper, Tech. Rep., 2007.

[28] S. Nazari, R. Kiwan, J. Siegel, and A. Stefanopoulou, "Waste energy recovery through turbo generation:"unexpected fuel efficiency sweet spot for transient control."," in *2018 Annual American Control Conference (ACC)*. IEEE, 2018, pp. 13–18.

[29] U. Hopmann and M. C. Algrain, "Diesel engine electric turbo compound technology," SAE Technical Paper, Tech. Rep., 2003.

[30] A. Panday and H. O. Bansal, "A review of optimal energy management strategies for hybrid electric vehicle," *International Journal of Vehicular Technology*, vol. 2014, 2014.

[31] C.-C. Lin, H. Peng, J. W. Grizzle, and J.-M. Kang, "Power management strategy for a parallel hybrid electric truck," *IEEE transactions on control systems technology*, vol. 11, no. 6, pp. 839–849, 2003.

[32] S. Nazari, J. Siegel, and A. Stefanopoulou, "Control of hybrid boosting in highly diluted internal combustion engines," *accepted to IEEE Transactions on Control Systems Technology*, 2019.

[33] S. Nazari, J. B. Siegel, and A. Stefanopoulou, "Optimal energy management for a mild hybrid vehicle with electric and hybrid engine boosting systems," *IEEE Transactions on Vehicular Technology*, 2019.

[34] S. Nazari, J. Siegel, and A. Stefanopoulou, "Optimal energy management for a hybrid electric vehicle with a power split supercharger," in *2018 IEEE Vehicle Power and Propulsion Conference (VPPC)*. IEEE, 2018, pp. 1–6.

[35] S. Nazari, R. Middleton, J. Siegel, and A. Stefanopoulou, "Equivalent consumption minimization strategy for a power split supercharger," SAE Technical Paper, Tech. Rep., 2019-01-1207.

[36] S. Nazari, N. Prakash, J. Siegel, and A. Stefanopoulou, "On the effectiveness of hybridization paired with eco-driving," in *2019 Annual American Control Conference (ACC)*. IEEE, 2019.

[37] G.-P. U. GT-Suite Mannual, "Gt-suite version 7.5," *Gamma Technologies Inc, https://www.gtisoft.com*, 2016.

[38] L. Eriksson and L. Nielsen, *Modeling and control of engines and drivelines*. John Wiley & Sons, 2014.

[39] E. Hendricks, "A compact, comprehensive model of large turbocharged, two-stroke diesel engines," SAE Technical Paper, Tech. Rep., 1986.

[40] L. Guzzella and C. Onder, *Introduction to modeling and control of internal combustion engine systems*. Springer Science & Business Media, 2009.

[41] J.-P. Jensen, A. Kristensen, S. C. Sorenson, N. Houbak, and E. Hendricks, "Mean value modeling of a small turbocharged diesel engine," SAE Technical Paper, Tech. Rep., 1991.

[42] P. Moraal and I. Kolmanovsky, "Turbocharger modeling for automotive control applications," SAE Technical Paper, Tech. Rep., 1999.

[43] N. Watson and M. S. Janota, *Turbocharging: The internal combustion engine*. Macmillan, 1982.

[44] L. Jiang, J. Vanier, H. Yilmaz, and A. Stefanopoulou, "Parameterization and simulation for a turbocharged spark ignition direct injection engine with variable valve timing," SAE Technical Paper, Tech. Rep., 2009.

[45] P. H. Gorzelic, "Modeling and model-based control of multi-mode combustion engines for closed-loop si/hcci mode transitions with cam switching strategies," Ph.D. dissertation, The University of Michigan, 2015.

[46] U. Nowak, J. Frauhammer, and U. Nieken, "A fully adaptive algorithm for parabolic partial differential equations in one space dimension," *Computers and chemical engineering*, vol. 20, no. 5, pp. 547–561, 1996.

[47] R. Salehi, G. Vossoughi, and A. Alasty, "Modeling and estimation of unmeasured variables in a wastegate operated turbocharger," *Journal of Engineering for Gas Turbines and Power*, vol. 136, no. 5, p. 052601, 2014.

[48] "Tvs v400 specifications," https://www.eaton.com/us/en-us/catalog/engine-solutions/tvs-v400.specifications.html, Accessed: 01-16-2019.

[49] R. J. Middleton, O. G. H. Gupta, H.-Y. Chang, G. Lavoie, and J. Martz, "Fuel efficiency estimates for future light duty vehicles, part a: Engine technology and efficiency," SAE Technical Paper, Tech. Rep., 2016.

[50] F. Bonatesta, B. Waters, and P. Shayler, "Burn angles and form factors for wiebe function fits to mass fraction burned curves of a spark ignition engine with variable valve timing," *International Journal of Engine Research*, vol. 11, no. 2, pp. 177–186, 2010.

[51] B. Hoepke, S. Jannsen, E. Kasseris, and W. K. Cheng, "EGR effects on boosted si engine operation and knock integral correlation," *SAE International Journal of Engines*, vol. 5, no. 2012-01-0707, pp. 547–559, 2012.

[52] S. Bai, J. Maguire, and H. Peng, *Dynamic analysis and control system design of automatic transmissions*. SAE International Warrendale, Pennsylvania, 2013, vol. 21.

[53] S. P. Nuesch, "Analysis and control of multimode combustion switching sequence." 2015.

[54] National Highway Traffic Safety Administration U.S. Department of Transportation, *Midterm Evaluation of Light-Duty Vehicle Greenhouse Gas Emission Standards and Corporate Average Fuel Economy Standards for Model Years 2022-2025*, 2016.

[55] N. Ravi, H.-H. Liao, A. F. Jungkunz, and J. C. Gerdes, "Mid-ranging control of a multi-cylinder hcci engine using split fuel injection and valve timings," *IFAC Proceedings Volumes*, vol. 43, no. 7, pp. 797–802, 2010.

[56] M. Larsen and P. Kokotovic, "Passivation design for a turbocharged diesel engine model," in *Decision and Control, 1998. Proceedings of the 37th IEEE Conference on*, vol. 2. IEEE, 1998, pp. 1535–1540.

[57] S. J. Schroeck and W. C. Messner, "On controller design for linear time-invariant dual-input single-output systems," in *American Control Conference, 1999. Proceedings of the 1999*, vol. 6. IEEE, 1999, pp. 4122–4126.

[58] I. Kolmanovsky and A. G. Stefanopoulou, "Evaluation of turbocharger power assist system using optimal control techniques," SAE Technical Paper, Tech. Rep., 2000.

[59] R. J. Middleton, J. Martz, A. G. Stefanopoulou, and M. S. Wooldridge Voronoi, "Partitions for assessing fuel consumption of advanced technology engines: An approximation of full vehicle simulation on a drive cycle," *In Preparation*, 2017.

[60] S. Nazari, R. J. Middleton, J. Martz, and A. G. Stefanopoulou, "The elusive consequences of slow engine response on drive cycle fuel efficiency," in *American Control Conference (ACC), 2017*. IEEE, 2017, pp. 5379–5385.

[61] M. J. Van Nieuwstadt, I. V. Kolmanovsky, and P. E. Moraal, "Coordinated egr-vgt control for diesel engines: an experimental comparison," SAE Technical paper, Tech. Rep., 2000.

[62] R. Kiwan, A. G. Stefanopoulou, J. Martz, G. Surnilla, I. Ali, and D. J. Styles, "Effects of differential pressure measurement characteristics on low pressure-egr estimation error in si-engines," *IFAC-PapersOnLine*, vol. 49, no. 11, pp. 722–729, 2016.

[63] A. Y. Karnik, J. H. Buckland, and J. S. Freudenberg, "Electronic throttle and wastegate control for turbocharged gasoline engines," in *American Control Conference, 2005. Proceedings of the 2005*. IEEE, 2005, pp. 4434–4439.

[64] P. Moulin and J. Chauvin, "Modeling and control of the air system of a turbocharged gasoline engine," *Control Engineering Practice*, vol. 19, no. 3, pp. 287–297, 2011.

[65] A. Thomasson, L. Eriksson, O. Leufven, and P. Andersson, "Wastegate actuator modeling and model-based boost pressure control," *IFAC Proceedings Volumes*, vol. 42, no. 26, pp. 87–94, 2009.

[66] J. Livengood and P. Wu, "Correlation of autoignition phenomena in internal combustion engines and rapid compression machines," in *Symposium (international) on combustion*, vol. 5, no. 1. Elsevier, 1955, pp. 347–356.

[67] M. Stuhldreher, C. Schenk, J. Brakora, D. Hawkins, A. Moskalik, and P. DeKraker, "Downsized boosted engine benchmarking and results," SAE Technical Paper, Tech. Rep., 2015.

[68] M. Salazar, P. Elbert, S. Ebbesen, C. Bussi, and C. H. Onder, "Time-optimal control policy for a hybrid electric race car," *IEEE Transactions on Control Systems Technology*, 2017.

[69] J. Wang, B. Taylor, Z. Sun, and D. Howe, "Experimental characterization of a supercapacitor-based electrical torque-boost system for downsized ice vehicles," *IEEE Transactions on Vehicular Technology*, vol. 56, no. 6, p. 3674, 2007.

[70] N. Murgovski, S. Marinkov, D. Hilgersom, B. de Jager, M. Steinbuch, and J. Sjöberg, "Powertrain sizing of electrically supercharged internal combustion engine vehicles," *IFAC-PapersOnLine*, vol. 48, no. 15, pp. 101–108, 2015.

[71] R. Aymanns, T. Uhlmann, C. Nebbia, and T. Plum, "Electric supercharging new opportunities with higher system voltage," *MTZ worldwide*, vol. 75, no. 7-8, pp. 4–11, 2014.

[72] F. Millo, F. Mallamo, E. Pautasso, and G. G. Mego, "The potential of electric exhaust gas turbocharging for hd diesel engines," SAE Technical paper, Tech. Rep., 2006.

[73] D. Zhao, R. Stobart, G. Dong, and E. Winward, "Real-time energy management for diesel heavy duty hybrid electric vehicles," *IEEE Transactions on Control Systems Technology*, vol. 23, no. 3, pp. 829–841, 2015.

[74] C.-C. Lin, H. Peng, and J. Grizzle, "A stochastic control strategy for hybrid electric vehicles," in *American Control Conference, 2004. Proceedings of the 2004*, vol. 5. IEEE, 2004, pp. 4710–4715.

[75] N. Kim, S. Cha, and H. Peng, "Optimal control of hybrid electric vehicles based on pontryagin's minimum principle," *IEEE Transactions on Control Systems Technology*, vol. 19, no. 5, pp. 1279–1287, 2011.

[76] S. Delprat, J. Lauber, T.-M. Guerra, and J. Rimaux, "Control of a parallel hybrid powertrain: optimal control," *IEEE transactions on Vehicular Technology*, vol. 53, no. 3, pp. 872–881, 2004.

[77] T. Nüesch, P. Elbert, M. Flankl, C. Onder, and L. Guzzella, "Convex optimization for the energy management of hybrid electric vehicles considering engine start and gearshift costs," *Energies*, vol. 7, no. 2, pp. 834–856, 2014.

[78] H. Borhan, A. Vahidi, A. M. Phillips, M. L. Kuang, I. V. Kolmanovsky, and S. Di Cairano, "Mpc-based energy management of a power-split hybrid electric vehicle," *IEEE Transactions on Control Systems Technology*, vol. 20, no. 3, pp. 593–603, 2012.

[79] G. Paganelli, S. Delprat, T.-M. Guerra, J. Rimaux, and J.-J. Santin, "Equivalent consumption minimization strategy for parallel hybrid powertrains," in *Vehicular Technology Conference, 2002. VTC Spring 2002. IEEE 55th*, vol. 4. IEEE, 2002, pp. 2076–2081.

[80] C. Musardo, G. Rizzoni, Y. Guezennec, and B. Staccia, "A-ecms: An adaptive algorithm for hybrid electric vehicle energy management," *European Journal of Control*, vol. 11, no. 4-5, pp. 509–524, 2005.

[81] M. Sivertsson and L. Eriksson, "Design and evaluation of energy management using map-based ecms for the phev benchmark," *Oil & Gas Science and Technology–Revue dIFP Energies nouvelles*, vol. 70, no. 1, pp. 195–211, 2015.

[82] O. Sundstrom and L. Guzzella, "A generic dynamic programming matlab function," in *Control Applications,(CCA) & Intelligent Control,(ISIC), 2009 IEEE*. IEEE, 2009, pp. 1625–1630.

[83] "Final rule for fuel economy labeling of motor vehicles: Revisions to improve calculation of fuel economy estimates," https://www.epa.gov/regulations-emissions-vehicles-and-engines/final-rule-fuel-economy-labeling-motor-vehicles-revisions, Accessed: 2018-03-26.

[84] R. K. Ahuja and J. B. Orlin, "Inverse optimization," *Operations Research*, vol. 49, no. 5, pp. 771–783, 2001.

[85] G. Paganelli, M. Tateno, A. Brahma, G. Rizzoni, and Y. Guezennec, "Control development for a hybrid-electric sport-utility vehicle: strategy, implementation and field test results," in *American Control Conference, 2001. Proceedings of the 2001*, vol. 6. IEEE, 2001, pp. 5064–5069.

[86] C. Sun, F. Sun, and H. He, "Investigating adaptive-ecms with velocity forecast ability for hybrid electric vehicles," *Applied energy*, vol. 185, pp. 1644–1653, 2017.

[87] M. Barth and K. Boriboonsomsin, "Energy and emissions impacts of a freeway-based dynamic eco-driving system," *Transportation Research Part D: Transport and Environment*, vol. 14, no. 6, pp. 400–410, 2009.

[88] C. Vagg, C. J. Brace, D. Hari, S. Akehurst, J. Poxon, and L. Ash, "Development and field trial of a driver assistance system to encourage eco-driving in light commercial vehicle fleets." *IEEE Trans. Intelligent Transportation Systems*, vol. 14, no. 2, pp. 796–805, 2013.

[89] G. Klunder, K. Malone, J. Mak, I. Wilmink, A. Schirokoff, N. Sihvola, C. Holmén, A. Berger, R. d. Lange, W. Roeterdink *et al.*, "Impact of information and communication technologies on energy efficiency in road transport-final report," 2009.

[90] S. Li, K. Li, J. Wang, L. Zhang, X. Lian, H. Ukawa, and D. Bai, "Mpc based vehicular following control considering both fuel economy and tracking capability," in *Vehicle Power and Propulsion Conference, 2008. VPPC'08. IEEE*. IEEE, 2008, pp. 1–6.

[91] C. Manzie, H. Watson, and S. Halgamuge, "Fuel economy improvements for urban driving: Hybrid vs. intelligent vehicles," *Transportation Research Part C: Emerging Technologies*, vol. 15, no. 1, pp. 1–16, 2007.

[92] H. Kato, R. Ando, Y. Kondo, T. Suzuki, K. Matsuhashi, and S. Kobayashi, "Comparative measurements of the eco-driving effect between electric and internal combustion engine vehicles," in *Electric Vehicle Symposium and Exhibition (EVS27), 2013 World*. IEEE, 2013, pp. 1–5.

[93] N. Prakash, A. G. Stefanopoulou, A. J. Moskalik, and M. J. Brusstar, "Use of the hypothetical lead (hl) vehicle trace: A new method for evaluating fuel consumption in automated driving," in *American Control Conference (ACC), 2016*. IEEE, 2016, pp. 3486–3491.

[94] M. Treiber, A. Hennecke, and D. Helbing, "Congested traffic states in empirical observations and microscopic simulations," *Physical review E*, vol. 62, no. 2, p. 1805, 2000.